E.O. Paton Electric Welding Institute of the National Academy of Science of Ukraine
International Association “Welding”

The Paton Welding Journal

05
2025

International Scientific-Technical and Production Journal ♦ Founded in January 2000 (12 Issues Per Year)

Address of Editorial Office:
E.O. Paton Electric Welding Institute, 11 Kazymyr Malevych Str., 03150, Kyiv, Ukraine
E-mail: office@paton.kiev.ua; https://paton.org.ua/en/

Address of Publisher:
International Association “Welding”, 11 Kazymyr Malevych Str., 03150, Kyiv, Ukraine
Tel.: (38044) 205 23 90, E-mail: patonpublishinghouse@gmail.com; journal@paton.kiev.ua
https://patonpublishinghouse.com/eng/journals/tpwj

The Journal was registered by the National Council of Ukraine on Television and Radio Broadcasting on 09.05.2024, carrier identifier R30-04569
ISSN 0957-798X (Print), ISSN 3041-2293 (Online)
DOI: https://doi.org/10.37434/tpwj, from #01, 2020 to now; DOI: https: //doi.org/10.15407/tpwj from #01, 2014 to #12, 2019.

Subscriptions, 12 issues per year:
348 Euro — annual subscription for the printed (hard copy) version, air postage and packaging included;
288 Euro — annual subscription for the electronic version (sending issues in pdf format or providing access to IP addresses).

Representative Offices of “The Paton Welding Journal”:

BRAZIL, Arc Dynamics
Address: Nova Iguacu, Rio de Janeiro, Brazil
Daniel Adolpho, Tel.: +55 21 9 6419 5703,
E-mail: dadolpho@arcdynamics.com.br

CHINA, China-Ukraine Institute of Welding, Guangdong Academy of Sciences
Address: Room 210, No. 363 Changxing Road, Tianhe, Guangzhou, 510650, China
Zhang Yupeng, Tel.: +86-20-61086791,
E-mail: patonjournal@gwi.gd.cn

BULGARIA, Bulgarian Welding Society
Address: Blvd. Asen Yordanov No.10, Sofia 1592, Bulgaria
Pavel Popgeorgiev, Tel.: +359 899 96 22 20,
E-mail: office@bws-bg.org

POLAND, PATON EUROPE Sp. z o. o.
Address: ul. Kapitałowa 4, 35-213, Rzeszów, Poland
Anton Stepakhno, Tel.: +38067 509 95 67,
E-mail: Anton.Stepakhno@paton.ua

The content of the Journal includes articles received from authors from around the world in the field of welding, cutting, cladding, soldering, brazing, coating, 3D additive technologies, electrometallurgy, material science, NDT and selectively includes translations into English of articles from the following journals, published in Ukrainian:

- «Avtomatychne Zvaryuvannya» (Automatic Welding), https://patonpublishinghouse.com/eng/journals/as;
- «Suchasna Elektrometalurhiya» (Electrometallurgy Today), https://patonpublishinghouse.com/eng/journals/sem;
- «Tekhnichna Diahnostyka ta Neruinivnyi Kontrol» (Technical Diagnostics & Nondestructive Testing), https://patonpublishinghouse.com/eng/journals/tdnk.

CONTENTS

ORIGINAL ARTICLES

*Translated Article(s) from “Avtomatychne Zvaryuvannya” (Automatic Welding), No. 2, 2025.

**Translated Article(s) from “Suchasna Elektrometalurhiya” (Electrometallurgy Today), No. 4, 2024.

***Translated Article(s) from “Tekhnichna Diahnostyka ta Neruinivnyi Kontrol” (Technical Diagnostics & Nondestructive Testing), No. 1, 2025.

Indexing: The electronic edition of the Journal is stored in the V.I. Vernadsky National Library of Ukraine (eVerLib), included in the OPEN UKRAINIAN CITATION INDEX database and international databases: CROSSREF, EBSCO, Google Scholar, INDEX COPERNICUS, ULRICHSWEB.

DOI: https://doi.org/10.37434/tpwj2025.05.01

SPHERICAL TITANIUM POWDER PRODUCTION FOR 3D PRINTING BY PLASMA-ARC ATOMIZATION OF WIRE MATERIALS

V.M. Korzhyk[1], D.V. Strohonov[1], O.S. Tereshchenko[1], O.V. Ganushchak[1], A.Yu. Tunik[1], V.A. Kostin[1], S.L. Chygileichyk[2], V.K. Yuliuhin[1]

[1]E.O. Paton Electric Welding Institute of the NASU
11 Kazymyr Malevych Str., 03150, Kyiv, Ukraine
[2]JSC "Ivchenko-Progress"
2 Ivanova Str., 69068, Zaporizhzhia, Ukraine

ABSTRACT

The possibility of spherical titanium powder production by plasma-arc atomization of solid Cp-Ti Grade 2 wire with a diameter of 1.0 and 1.6 mm has been experimentally confirmed. Analysis of the particle size distribution of the powder showed that in the case of atomization of titanium wire with a diameter of 1.0 mm, the main fraction is –140 μm, which is 96 % of the total mass of the powder, where the amount of the finely dispersed fraction of –63 μm is up to 60 wt. %, and in the case of wire with a diameter of 1.6 mm, the main fraction is –200 μm, which is 95 wt.%, while the amount of the finely dispersed fraction of –63 μm does not exceed 38 wt.%. A study of shape parameters of the titanium powder was performed, which showed that most particles have a regular spherical shape with an average sphericity coefficient close to 0.9, the number of particles with satellites and particles of irregular shape does not exceed 1 wt.%, which determines the high technological properties of the produced powder, which are on a par with other industrial technologies of spherical powder production by plasma and gas atomization methods. The chemical and phase composition of the atomized powder was investigated, and it was found that the phase composition consists of α-Ti, and the chemical composition corresponds to the ASTM B 348-05 standard. It was shown that application of the technology of plasma-arc atomization of titanium wire allows obtaining spherical powders that can be used as consumables for 3D printing of products for the aviation, rocket and space, medical, energy and chemical industries by the methods of electron beam melting (EBM), laser direct energy deposition (LDED) and plasma metal deposition (PMD).

KEYWORDS: plasma-arc atomization, wire, compact section, titanium, sphericity, powders, 3D printing

INTRODUCTION

Recently, due to the intensive development of aviation, rocket and space, medical, energy and chemical industries there has been a significant need in manufacturing volumetric complex-shaped parts from titanium and its alloys, predominantly using additive technologies of 3D printing [1, 2].

The main additive technologies of growing products from titanium and its alloys include: Selective Laser Melting (SLM), Selective Laser Sintering (SLS), Electron Beam Melting (EBM), methods of Laser Direct Energy Deposition (LDED) and Plasma Metal Deposition (PMD), etc. All these methods use specialized spherical powders (predominantly finely-dispersed) as consumable materials to form the additive layers, with strict requirements being made of the powder particle size distribution, shape, and physical-chemical and technological properties. So, for instance, powders of a narrow fraction of 15–45 μm are used for SLM process, powders of 45–106 μm are applied for EBM, those of 45–150 μm are used for LDED, and powders of 63–160 μm fraction are designed for PMD technology [3–5]. Moreover, the above powders should have a spherical shape with minimal number of external (satellites) and internal (pores) defects, good technological properties (high flowability, bulk density, coefficient of sphericity, etc.) and low content of gas mixtures, providing a high packing density of the additive layers, reduction of porosity and improvement of mechanical properties of the final product [6–8].

LITERATURE DATA ANALYSIS AND PROBLEM DEFINITION

At present, Vacuum Inert Gas Atomization (VIGA) is the most widespread technology for producing titanium powders for additive manufacturing. Alongside a number of advantages, described in works [9, 10], the above-mentioned technology has a number of essential drawbacks, namely [10-13]: presence of a large number of satellites and irregularly-shaped particles, lower coefficient of sphericity for the methods of gas atomization, of the melt resulting in low values of flowability (particularly for the fine fraction of <63 μm), and leading to defect formation in the deposited layers; presence of intragranular argon porosity for powders produced by gas atomization technology, which in some cases cannot be removed by further cold or hot pressure treatment; high cost of powder manufacture by gas at-

omization, as the gas-to-metal ratio (flow rate (m^3) of atomizing gas — argon, required to produce 1 kg of powder) can be equal to 26-110.

Plasma Rotating Electrode Process technology (PREP) has also become widespread, where the plasma jet melts the surface layer of the billet end face, and melt atomization is carried out due to off-center forces. However, this method also has several essential drawbacks, as PREP equipment operation involves considerable difficulties of producing –106 μm fraction: to achieve more than 40 vol.% yield of the above-mentioned fraction there is the need for a significant increase in the speed of billet rotation (more than 30 000 rpm) that complicates the already not at all simple kinematic diagram of the unit (lowering of the level of vibrations, designing complex bearing systems are required, etc.). We can also include here the difficulties associated with producing a cylindrical billet of precise dimensions, which should be ground with a high accuracy [12].

In this respect, prospects for manufacturing spherical powders open up, due to application of technologies, where wires or rods (ingots) are used as feedstock materials, and the processes of melt heating, melting and dispersion are performed by plasma jets, without using off-center forces, or high-speed equipment with a complex kinematic diagram. Among such technologies is the process of plasma-arc atomization, which is flexible, and can be used to produce powders from a wide class of materials (billets), which are either manufactured by industry (wires, rods), or can be produced by casting methods in the form of ingots [13, 14].

At present, in connection with the transition of additive manufacturing to a new level in Ukraine, its expansion and provision with consumables in full, particularly due to intensive progress of aviation and rocket and space industries, requires development of domestic technology and equipment to produce finely-dispersed spherical powders, particularly with the fractional composition of 63 μm, which is a relevant science and technology task.

RESEARCH OBJECTIVE AND TASKS

The objective of the work is analysis of the possibility and assessment of the prospects for application of the process of plasma-arc atomization of Cp-Ti Grade 2 titanium wire 1.0 and 1.6 mm in diameter for further development of the domestic technology and equipment to produce spherical powders for 3D printing. To achieve this goal, it is necessary to study the particle size distribution, morphology, microstructure, technological properties and chemical and phase composition of the powder manufactured using the technology of plasma-arc atomization of Cp-Ti Grade 2 titanium wire; provide conclusions regarding the possibility of application of the produced spherical powders for 3D printing by the methods of Selective Laser Melting (SLM) and Electron Beam Melting (EBM), Selective Laser Sintering (SLS), Laser Direct Energy Deposition (LDED) and Plasma Metal Deposition (PMD).

INVESTIGATION MATERIALS AND PROCEDURE

PROCEDURE OF WIRE ATOMIZATION AND DETERMINATION OF FRACTIONAL COMPOSITION OF THE POWDER

Experiments were performed using "PLAZER 50-PL-W" process equipment for plasma-arc atomization of wire materials (manufacturer is "SPC "PLAZER" Ltd, Ukraine) [15], with application of an experimental plasmatron with a copper hollow electrode operating by the scheme of "indirect action arc" (Figure 1, *a*, *b*) [16]. Technology of plasma-arc atomization of wire materials (Plasma Atomization (PA)) is well described in works [17–19], and in the general case it consists in melting the wire, fed into the zone of

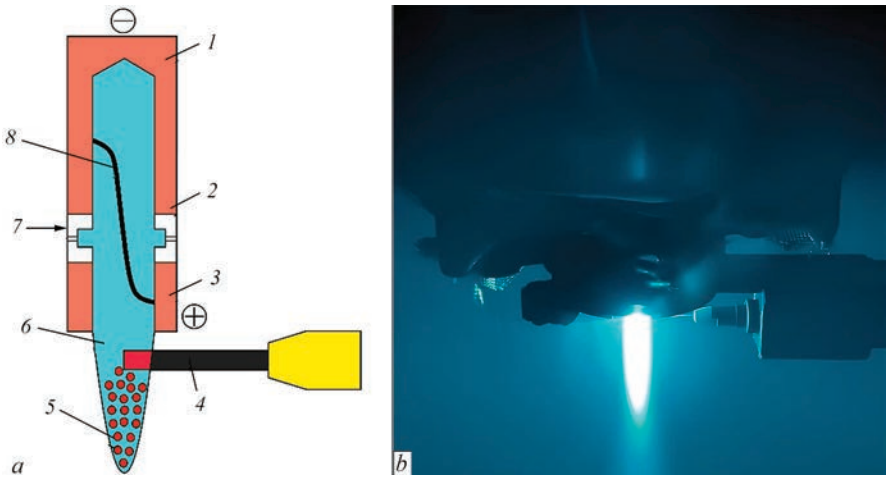

Figure 1. Scheme (*a*) and visualization (*b*) of the process of plasma-arc atomization of Cp-Ti Grade 2 titanium wire in the atomization chamber

plasma jet outflow under the plasmatron nozzle edge and further fragmentation of the melt layer, formed at the atomized wire tip. This method provides formation of a high-speed (in some cases, supersonic) plasma jet, which greatly increases the dynamic pressure on the dispersed melt, and leads to its intensive fragmentation, that, in its turn, creates the conditions for producing an optimal particles size distribution of the dispersed phase.

Plasma-arc atomization of the wire was conducted in a laboratory atomization chamber in an argon atmosphere, according to the procedure of [20], where pumping down of the chamber inner volume to residual pressure of $5–7\times10^{-3}$ Torr was performed before filling it with gas. Residual pressure values were monitored, using thermocouple manometric transducer PMT-2 (Ukraine) and ionization-thermocouple vacuum gauge VIT-2 (Ukraine).

Parameters of the mode of plasma-arc atomization of the neutral wire were as follows: current of 300 A; arc working voltage of 140 V; plasma-forming gas flow rate of 15 m^3/h, wire feed rate of 3–7 m/min, distance from the plasmatron nozzle edge to the atomized wire of 4 mm. Plasma-forming gas was argon of the highest grade I1 to ISO 14175-2008 in both the cases.

Acceptable atomization modes were determined after achieving of the minimal angle of opening of the plasma jet had and the process stability during melting of the atomized wire in the axial zone of the plasma jet.

Particle size distribution of laboratory batches of the powders was determined by sieve analysis in keeping with the procedure of ISO 2591-1:1988 in shock sieve analyzer "AS 200U (ROTAP)" (Ukraine) with a set of sieves with hole dimensions of 25–400 μm, sample weight being not less than 200 g of powder.

ATOMIZATION MATERIALS

Solid wire from commercial Cp-Ti Grade 2 titanium 1.0 and 1.6 mm in diameter was used as atomization material. Its composition is given in Table 1.

DETERMINATION OF POWDER MORPHOLOGY AND MICROSTRUCTURE

The appearance of powder particles was studied in scanning electron microscope JEOL JSM-840 (Japan) at the following parameters: $U = 20$ kV, $I = 10^{-10}–10^{-7}$ A. Images were obtained in secondary electron mode of ZAF/PB computer program, designed for studying rough surfaces. Further analysis of the images for powder sphericity investigation was performed in MIPAR software product (USA) by the procedure of [21].

Table 1. Chemical composition of atomized Cp–Ti grade 2 wires according to the certificate of origin, wt.%

Ti	Fe	O	C	N	H
Base	0.2	0.18	0.05	≤0.03	0.012

DETERMINATION OF THE POWDER PHASE COMPOSITION

Phase composition of the powder and lattice parameters of the individual phases were studied by the method of X-ray diffraction phase analysis (XDPA). X-ray studies were conducted in DRON-M1 diffractometer (Ukraine) in monochromatic CuK_α-radiation. Used as a monochromator was a graphite single crystal mounted on a diffracted beam. Diffractograms were recorded by step-by-step scanning in the range of angles $2\theta = 10–120°$. Scanning step was equal to 0.05°, exposure time was 3–9 s. Diffractometric measurement data was processed using programs for full-profile analysis of X-ray spectra from a mixture of polycrystalline components PowderCell 2.4 (Germany).

DETERMINATION OF ELEMENTAL CHEMICAL COMPOSITION OF THE POWDER

The method of X-ray spectral microanalysis (XMA) with application of Link 860/500 detector (Great Britain) was used to determine the elemental chemical composition of the titanium powder.

DETERMINATION OF THE CONTENT OF OXYGEN AND NITROGEN IN THE POWDER

Investigations of the content of oxygen and nitrogen in the atomized powders were performed in gas analyzer LECO TC-436 Nitrogen Oxygen Analyzer (USA).

DETERMINATION OF THE TECHNOLOGICAL PROPERTIES OF THE POWDER

Powder flowability was determined in Hall instrument according to ASTM B213 standard. Measurements of bulk density were conducted according to ASTM B212 standard.

INVESTIGATION RESULTS AND DISCUSSION

Studies of particle size distribution of the produced powder (Figure 2) showed that the largest quantity of the powder finely-dispersed fraction is observed at atomization of 1.0 mm titanium wire, where the main powder fraction is 140 μm, making up 96 wt.%, and the proportion of the finely-dispersed fraction of 63 μm is 59 wt.%. In the case of atomization of 1.6 mm titanium wire, the main powder fraction is 200 μm, which is 95 wt.%, and the quantity of fine-

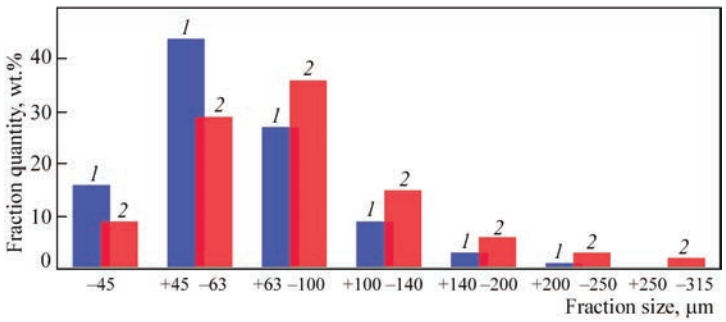

Figure 2. Distribution of the particle size distribution of powder produced in plasma-arc atomization of Cp–Ti Grade 2 titanium wire with a diameter of 1.0 (*1*) and 1.6 mm (*2*)

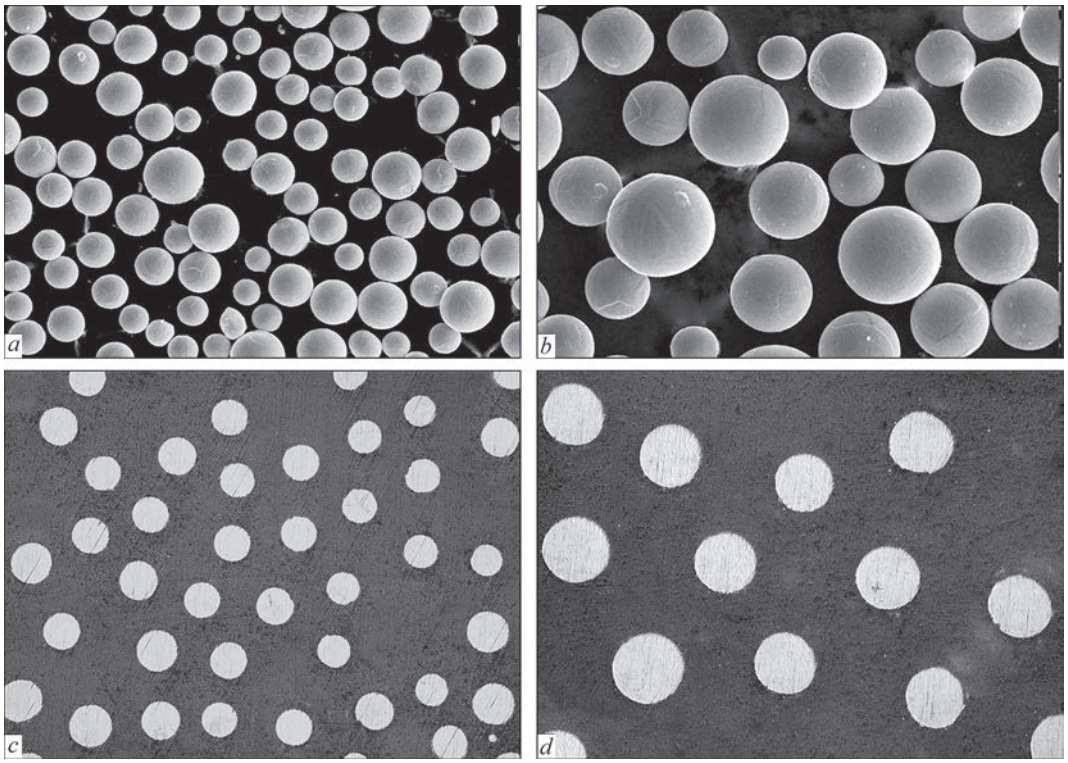

Figure 3. SEM images of the morphology (*a, b*) and microstructure (*c*, *d*) of Cp-Ti Grade 2 titanium powder of 106 μm fraction; *a*, *c* — ×100; *b*, *d* — ×200

ly-dispersed powder fraction of 63 μm does not exceed 38 wt.%.

Formation of finer powders during atomization of 1.0 mm titanium wire with other unchanged process

Table 2. Comparison of the technological properties of Cp-Ti Grade 2 titanium powder produced by SS-PREP, GA and PA technologies

Method	Fraction size, μm	Flowability, s/50 g	Bulk density, g/cm^3
SS-PREP (Sino-euro Ltd, China) [23]	15–45	≤30	≥2.5
	45–106	≤27	≥2.5
	45–150	≤27	≥2.5
GA (Hoganas, Sweden) [24]	15–45	40	2.34
	45–106	35	2.37
	45–150	33	2.37
PA (AP&C, USA) [25]	15–45	29	2.55
	45–106	25	2.61
	45–150	23	2.65
PA (PWI, Ukraine)	15–45	32	2.46
	45–106	28	2.53
	45–150	25	2.57

Table 3. Chemical composition of the feedstock wire and titanium powder Cp-Ti Grade 2, wt.%

Studied zone	Ti	Fe	O	N
ASTM Standard B 348-05	Base	≤0.30	≤0.25	≤0.03
Initial wire		0.18	0.23	0.02
Powder of 106 μm fraction		0.19	0.20	0.01
Powder of +106, –106 μm fraction		0.21	0.22	0.02

Table 4. Results of XDA of Cp-Ti Grade 2 titanium powder of –106, +106; –160 μm

Sample	Phases	Phase content, vol.%	Lattice parameters, Å
Powder fraction of –106 μm	α-Ti	100	a = 2.9487; c = 4.6850; c/a = 1.5888
Powder fraction of +106; –160 μm			a = 2.9501; c = 4.6871; c/a = 1.5887

parameters is attributable to smaller dimensions of the liquid interlayer, compared to those of the interlayer forming at the tip of atomized 1.6 mm wire. This, in its turn, promotes reduction in the dimensions of the fragments forming at atomization [16].

Analysis of titanium powder morphology in MIPAR software (Figure 3) in the case of 106 μm fraction showed that the powder is of a spherical shape, with average coefficient of sphericity S = 0.87–0.91. External defects in the form of satellites and irregularly-shaped particles are practically absent, their proportion not exceeding 1 wt.%, and dendrites and grain boundaries coming to the powder surface are observed. Investigations of powder microstructure showed absence of internal defects in the form of cavities, cracks, etc.

High indices of sphericity of the studied powders determine their high technological properties (Table 2), which can be compared to the properties of powders produced by the SS-PREP technology ([22]) at the speed of more than 30 000 rpm.

XMA and gas analysis methods were used to establish the chemical composition of powders (Table 3), produced during plasma-arc atomization of Cp-Ti Grade 2 titanium wire, and to determine that it corresponds to the chemical composition of the feedstock material — the wire (ASTM B 348-05 standard).

Proceeding from the results of X-ray studies (Figure 4, Table 4), it was established that the powder phase composition consists of α-Ti with the following FCC lattice parameters: a = 2.95 Å; c = 4.69 Å.

Analysis of the results of studying the chemical and phase composition, technological properties and particle size distribution of spherical titanium powder Cp-Ti Grade 2, produced during plasma-arc atomization, showed that the above-mentioned powders can be used for 3D printing by different methods. Plasma-arc atomization of current-conducting 1.0 mm wire allows producing sound titanium wires, where the proportion of the fraction of 45–106 μm is up to

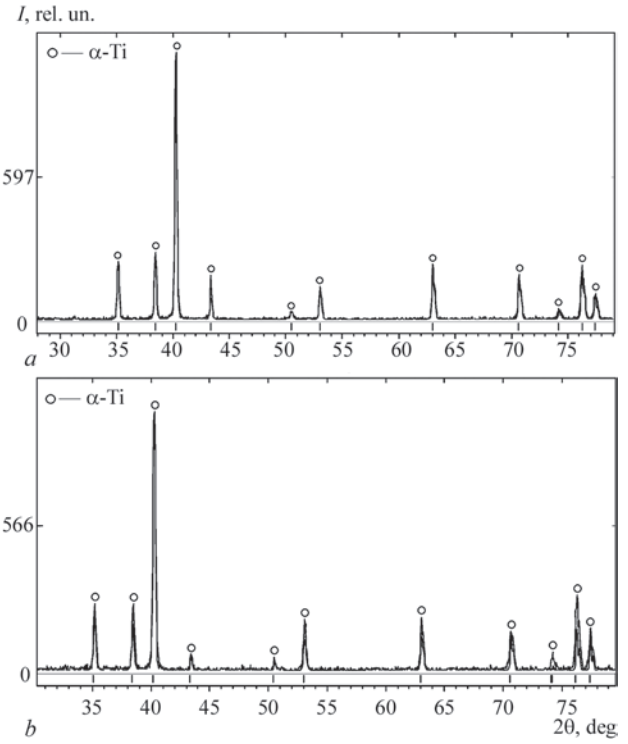

Figure 4. Diffractograms of Cp-Ti Grade 2 titanium powders of the fractions: –106 μm (*a*), +106; –160 μm (*b*)

70 wt.%, which it is rational to use predominantly in the electron beam melting (EBM) process; plasma-arc atomization of current-conducting 1.6 mm wire allows producing sound titanium powders, where the proportion of the fraction of 45–140 μm makes up to 80 wt.%, which it is more rational to use for direct laser deposition (LDED) and plasma metal deposition (PMD) processes.

CONCLUSIONS

1. It was determined that during plasma-arc atomization of 1.0 mm Cp-Ti Grade 2 titanium wire the main powder fraction is 140 μm, making up 96 wt.%, of the total powder weight, where the proportion of the finely-dispersed fraction of 63 μm is 59 wt.%. In the case of atomization of 1.6 mm titanium wire, the main

fraction is 200 μm, which is 95 wt.%, and the quantity of finely-dispersed powder fraction of 63 μm does not exceed 38 wt.%. On the whole, the powders are of a regular spherical shape with the coefficient of sphericity close to 0.9, with a small quantity of satellites and irregularly-shape particles (<1 wt.%). Investigations of the chemical and phase composition of the titanium powder showed that the phase composition of the atomized powder, irrespective of the fraction size, consists of α-Ti, and its chemical composition corresponds to ASTM B 348-05 standard for rods and billets from titanium and its alloys.

2. Derived results allow considering the process of plasma-arc atomization of wire materials as an effective technology, which allows producing sound domestic spherical powders, the technological properties of which are at the same level with another industrial method of producing spherical powders for 3D printing: SS-PREP (with more than 30000 rpm speed), and have higher characteristics, compared to gas atomization processes (VIGA, etc.). The particle size distribution of the produced powders determines the good prospects for their application exactly in the processes of electron beam melting (EBM), direct laser deposition (LDED) and plasma metal deposition (PMD). In the SLM process a relatively low yield of the required 45 μm fraction at the level of 15 wt.% is achieved, so further research is required to increase the yield of the above powder fraction during plasma-arc atomization of wire materials.

REFERENCES

1. Nguyen, H., Pramanik, A., Basak, A. et al. (2022) A critical review on additive manufacturing of Ti6Al4V alloy: Microstructure and mechanical properties. *J. of Materials Research and Technology*, **18**, 4641–4661. DOI: https://doi.org/10.1016/j.jmrt.2022.04.055
2. Matviichuk, V.A., Nesterenkov, V.M., Berdnikova, O.M. (2022) Additive electron beam technology for manufacture of metal products from powder materials. *The Paton Welding J*., **2**, 16–26. DOI: https://doi.org/10.37434/as2022.02.03
3. Ahn, D. (2021) Directed energy deposition (DED) process: State of the art. *Inter. J. of Precis. Eng. and Manuf.-Green Tech*., **8**, 703–742. https://doi.org/10.1007/s40684-020-00302-7
4. Svetlizky, D., Das, M., Zheng, B. et al. (2021) Directed energy deposition (DED) additive manufacturing: Physical characteristics, defects, challenges and applications. *Materials Today*, **49**, 271–295. DOI: https://doi.org/10.1016/j.mattod.2021.03.020
5. King, W., Anderson, A., Ferencz, R. et al. (2015) Laser powder bed fusion additive manufacturing of metals: Physics, computational, and materials challenges. *Applied Physics Reviews*, **2**, 041–304. DOI: https://doi.org/10.1063/1.4937809
6. Fatemeh, A, Haydari, Z., Salehi, H. et al. (2024) Spreadability of powders for additive manufacturing: A critical review of metrics and characterization methods. *Particuology*, **93**, 211–234. DOI: https://doi.org/10.1016/j.partic.2024.06.013
7. Olakanmi, E. (2013) Selective laser sintering/melting (SLS/SLM) of pure Al, Al–Mg, and Al–Si powders: Effect of processing conditions and powder properties. *J. of Materials Processing Technol.*, **213**, 1387–1405. DOI: https://doi.org/10.1016/j.jmatprotec.2013.03.009
8. Attar, H., Prashanth, K., Zhang, L. et al. (2015) Effect of powder particle shape on the properties of in situ Ti–TiB composite materials produced by selective laser melting. *J. of Mater. Sci. & Technol.*, **31**, 1001–1005. DOI: https://doi.org/10.1016/j.jmst.2015.08.007
9. Drawin, S., Deborde, A., Thomas, M. et al. (2020) Atomization of Ti–64 alloy using the EIGA process: Comparison of the characteristics of powders produced in lab scale and industrial-scale facilities. In: *MATEC Web of Conferences*, **321**, 07013. DOI: https://doi.org/10.1051/matecconf/202032107013
10. Xiao, H., Gao, B., Yu, S. et al. (2024) Life cycle assessment of metal powder production: A Bayesian stochastic Kriging model-based autonomous estimation. *Auton. Intell. Syst*., **4**, 20. DOI: https://doi.org/10.1007/s43684-024-00079-5
11. Chen, G., Zhao, S., Tan, P. et al. (2018) A comparative study of Ti6Al4V powders for additive manufacturing by gas atomization, plasma rotating electrode process and plasma atomization. *Powder Technology*, **333**, 38–46. DOI: https://doi.org/10.1016/j.powtec.2018.04.013
12. Sun, P., Fang, Z., Zhang, Y. et al. (2017) Review of the methods for the production of spherical Ti and Ti alloy powder. *JOM*, **69**, 1853–1860. DOI: https://doi.org/10.1007/s11837-017-2513-5
13. Korzhyk, V., Strohonov, D., Burlachenko, O. (2023) Development of plasma-arc technologies of spherical granule production for additive manufacturing and granule metallurgy. *The Paton Welding J*., **12**, 3–18. DOI: https://doi.org/10.37434/tpwj2023.12.01
14. Yurtukan, E., Unal, R. (2022) Theoretical and experimental investigation of Ti alloy powder production using low-power plasma torches. *Transact. of Nonferrous Metals Society of China*, **32**, 175–191. DOI: https://doi.org/10.1016/S1003-6326(21)65786-2
15. Korzhyk, V., Strohonov, D., Burlachenko, O. (2023) New generation unit for plasma-arc deposition of coatings and atomization of current-carrying wire materials. *The Paton Welding J*., **10**, 35–42. DOI: https://doi.org/10.37434/tpwj2023.10.06
16. Yin, Z., Yu, D., Zhang, Q. et al. (2021) Experimental and numerical analysis of a reverse-polarity plasma torch for plasma atomization. *Plasma Chem. Plasma Process*, **41**, 1471–1495. DOI: https://doi.org/10.1007/s11090-021-10181-8
17. Kharlamov, M., Krivtsun, I., Korzhyk, V. (2014) Dynamic model of the wire dispersion process in plasma-arc spraying. *J. of Thermal Spray Technol.*, **23**, 420–430. DOI: https://doi.org/10.1007/s11666-013-0027-4
18. Kharlamov, M., Krivtsun, I., Korzhyk, V. et al. (2015) Simulation of motion, heating, and breakup of molten metal droplets in the plasma jet at plasma-arc spraying. *J. of Thermal Spray Technol.*, **24**, 659–670. DOI: https://doi.org/10.1007/s11666-015-0216-4
19. Gulyaev, I., Dolmatov, A., Kharlamov, M. et al. (2015) Arc-plasma wire spraying: An optical study of process phenomenology. *J. of Thermal Spray Technol.*, **24**, 1566–1573. DOI: https://doi.org/10.1007/s11666-015-0356-6
20. Adeeva, L., Tunik, A., Korzhyk, V. et al. (2024) Properties of powders produced by plasma-arc spheroidization of current-carrying Fe–Al flux-cored wire. *Powder Metall. Met. Ceram*., **63**, 12–23. DOI: https://doi.org/10.1007/s11106-024-00434-4

21. Li, X., Cui, L., Shonkwiler, S. et al. (2023) Automatic characterization of spherical metal powders by microscope image analysis: A parallel computing approach. *J. Iron Steel Res*., **30**, 2293–2300. DOI: https://doi.org/10.1007/s42243-022-00907-z
22. Liu, Y., Zhao, X., Lai, Y. et al. (2020) A brief introduction to the selective laser melting of Ti6Al4V powders by supreme-speed plasma rotating electrode process. *Progress in Natural Sci.: Materials Intern.*, 1(**30**), 94–99. DOI: https://doi.org/10.1016/j.pnsc.2019.12.004

ORCID
V.M. Korzhyk: 0000-0001-9106-8593,
D.V. Strohonov: 0000-0001-9106-8593,
O.S. Tereshchenko: 0009-0003-4021-0758,
O.V. Ganushchak: 0000-0003-4392-6682,
A.Yu. Tunik: 0000-0001-6801-6461,
V.A. Kostin: 0000-0002-2677-4667,
S.L. Chygileichyk: 0000-0002-2372-9078,
V.K. Yuliuhin: 0009-0000-8377-6725

CONFLICT OF INTEREST
The Authors declare no conflict of interest

CORRESPONDING AUTHOR
V.M. Korzhyk
E.O. Paton Electric Welding Institute of the NASU
11 Kazymyr Malevych Str., 03150, Kyiv, Ukraine.
E-mail: vnkorzhyk@gmail.com

SUGGESTED CITATION
IV.M. Korzhyk, D.V. Strohonov, O.S. Tereshchenko, O.V. Ganushchak, A.Yu. Tunik, V.A. Kostin, S.L. Chygileichyk, V.K. Yuliuhin (2025) Spherical titanium powder production for 3D printing by plasma-arc atomization of wire materials. *The Paton Welding J*., **5**, 3–9.
DOI: https://doi.org/10.37434/tpwj2025.05.01

JOURNAL HOME PAGE
https://patonpublishinghouse.com/eng/journals/tpwj
Received: 06.01.2025
Received in revised form: 06.02.2025
Accepted: 17.05.2025

DOI: https://doi.org/10.37434/tpwj2025.05.02

IMPLEMENTATION AND SUSTAINABILITY OF BIOMASS GASIFICATION USING PLASMA TECHNOLOGIES

S.V. Petrov[1], O.I. Som[2], S.G. Bondarenko[3], O.V. Sanginova[3], M. Ganczarski[4], E. Rój[4]

[1]The Gas Institute of the NASU
39 Degtyarivska Str., 03113, Kyiv, Ukraine
[2]Plasma-Master Co., Ltd.
3 Omelian Pritsak Str., 03142, Kyiv, Ukraine
[3]National Technical University of Ukraine "Igor Sikorsky Kyiv Polytechnic Institute"
37 Prosp. Beresteiskyi, 03056, Kyiv, Ukraine
[4]Hydrogenium P.S.A. (Simple Joint Stock Company)
3/27 Marii Curie-Skłodowskiej Str., Lublin, Poland, 20-029

ABSTRACT

Waste biomass gasification technologies, especially with a focus on hydrogen production, have the potential for large-scale commercialization. The prerequisites for their development and promotion are innovative approaches to modeling, the use of traditional and new gasification mechanisms consistent with fundamental principles, and the development of new technical solutions on this basis. Ultimately, the goal is to significantly improve the gasification process's technical, economic, and environmental performance. In this context, plasma gasification is a promising renewable energy source from various wastes, including biomass. It contributes to achieving sustainable development goals: affordable and clean energy, climate change mitigation, waste diversion and resource reuse, reinforcing the concept of a circular economy. This paper presents an analysis and assessment of the conditions for increasing gasification processes' reliability, productivity, and quality while reducing costs, including potential barriers to applying plasma technologies. The paper presents new technological solutions to the problems facing gasification, aimed at optimizing energy flows in the gasification reactor, rational use of plasma as a concentrated energy flow, reducing electricity consumption by plasma torches, reducing the power and cost of plasma installations, as well as a radical solution to the problem of reliability of gasification equipment. The economic prospects for the transition to large-scale production, where a reduction in capital and operating costs can be expected, are considered.

KEYWORDS: biomass gasification, plasma gasification, plasmatron, synthesis gas, gasifier, energy efficiency of the gasification process

INTRODUCTION

The technical solution of converting biomass into fuel gas, gasification, is a key technology for producing products with higher value and application potential than the feedstock. The prerequisites for developing this technology are advanced, innovative, cost-effective and highly efficient methods. The strategy for improving the feasibility and sustainability of the biomass gasification process lies in technological advancement and minimizing the socio-environmental impacts [1]. Biomass has an advantage over other renewable energy sources because it depends less on location and climate. Biomass is easily stored and transported and is also available in abundance. This makes it a viable and promising feedstock as an energy source. Currently, biomass provides more than 10 % of the world's energy supply and is among the four largest energy sources in global final energy consumption [2].

Biomass waste gasification has an advantage over other existing methods, such as burial, incineration, etc., because it can convert a wide range of feedstocks into various useful products. Biomass gasification is a complex process that includes feedstock preparation, then a combination of pyrolysis, partial combustion of intermediate products, with final gasification, removal of inorganic residue, purification, and separation of synthesis gas. The gasification medium is important in converting intermediate products — solid carbon and heavy hydrocarbons into low-molecular gases such as carbon monoxide (CO) and hydrogen (H_2). The quality and properties of synthesis gas depend on the composition of the feedstock, size, gasifying agent, temperature, blast distribution in the reactor, and its design. Biomass gasification produces many useful components at the output, including synthesis gas, heat, electricity, green hydrogen, and fertilizers. Syngas can be further processed into methanol, dimethyl ether and other chemical products.

Biomass gasification for hydrogen production offers outstanding advantages regarding renewable energy resources, carbon neutrality, high efficiency and environmental benefits. However, the factors affecting H_2 production from biomass gasification are

complex, making it difficult to determine the optimal operating conditions [3].

THE REVIEW AIMS

to evaluate and classify plasma biomass gasification technologies based on the conditions for increasing productivity and quality while reducing costs, including potential barriers.

RESEARCH RESULTS

A common drawback of conventional gasifiers, whether with formation, downward emergence, or combined draft, is that the alternating gas contains tar to a greater or lesser extent, which is too problematic for many modern applications. Resin is considered the most inconvenient problem, which requires power outages, mainly when operating in large-scale conditions. Traditionally, steam reforming at elevated temperatures has been used as a solution. Water vapor gasification is an effective and well-proven method [4, 5]. In this case, the production of coke and resins is small, since steam converts them into CO and H_2 through water shear and reforming. Resins are never desired products and therefore reduce the efficiency of the process. Resin yield can be reduced by thermal cracking, steam reforming, dry reforming, carbonization and partial oxidation, which manifests itself in the following reactions:

$$pC_nH_x \leftrightarrow qC_mH_y + rH_2;$$

$$C_nH_x + mH_2O \leftrightarrow nCO + \left(m + \frac{x}{2}\right)H_2;$$

$$C_nH_x + nCO_2 \leftrightarrow 2nCO + \frac{x}{2}H_2;$$

$$C_nH_x \leftrightarrow nC + \frac{x}{2}H_2;$$

$$C_nH_x + \frac{n}{2}O_2 \leftrightarrow nCO + \frac{x}{2}H_2.$$

The authors of [6–9] found that the yield of H_2 during water vapor gasification is several times higher than that during air gasification. They also reported increased economic efficiency with higher H_2 production using water vapor as a gasification medium. It should be noted that a technological attempt to overcome this problem, which is helpful for further developments, is the concept of multi-stage gasification, which is applied at the Danish Technical University (Denmark) and Karlsruhe Institute of Technology (Germany) [10, 11]. This atypical gasification strategy separates the pyrolysis and gasification of biomass into separate stages with individual control, which are then integrated. Pyrolysis and gasification are carried out in separate zones inside the gasifier. This allows the biomass to be processed into usable products. The main motive for this concept is to obtain high-quality, clean synthesis gas with a low resin content. The permissible resin levels depend on the subsequent application. They are about 50 mg·Nm^{-3}, 5 mg·Nm^{-3} and 1 mg·Nm^{-3} for gas engines, gas turbines and fuel cells, respectively [12]. The exhaust gas contains significant amounts of ash and dust in all cases. A vital step between gas production in the gasifier and its utilization is gas treatment. The gas leaving the biomass gasification system is contaminated with resin, alkali metals, particulate matter, nitrogen (N_2), sulfur (S), and chlorine (Cl). According to the studies, gas cleaning was the most challenging issue in biomass gasification until recently [13]. To address this problem, various types of updraft and downdraft gasifiers have been developed, and many physical and catalytic methods for resin separation have been investigated. However, the most efficient and popular method for commercial purposes has yet to be developed. Efficient gasification and gas treatment methods allow the production of high-quality gas, ideally resin-free [14], which reduces the overall biomass consumption and ultimately reduces problems with biomass logistics and pre-treatment.

Plasma is also used in gasification processes in two ways: 1) as a heat source; 2) for cracking resins after standard gasification. Plasma gasification is primarily used for processing toxic organic waste, municipal solid waste, and rubber and plastics. Plasma technology has also attracted interest in syngas production and power generation and has entered the commercially competitive range. The main advantages of plasma gasification are syngas yield with high H_2 and CO content, increased heat content, low CO_2 yield, and low resin content [15–19]. The main limitations are the high capital and operating costs due to the high electricity consumption for plasma generation, resulting in low overall efficiency. For example, a base case scenario for a 680 tons per day waste treatment plant, suitable for a small town or regional business, would cost £97 mln, almost three times the cost of other waste treatment plants (such as incinerators).

The study [20] is indicative. Four biomass types — sawdust, plastic waste and oil obtained from the pyrolysis of waste tires — were investigated in a DC electric arc reactor with a torch power of 100 kW. A small amount of argon with H_2O vapor was used as plasma gas and H_2O as an oxidizing medium. High-quality synthesis gas containing 90 vol.% H_2 and CO for all four types of feedstock was obtained, and the resin content was below the sensitivity of the analysis method (1 mg/nm^3). A higher energy requirement compensates for these circumstances. Despite the high heat content in the output gases recorded for all data sets, the process efficiency was low due to

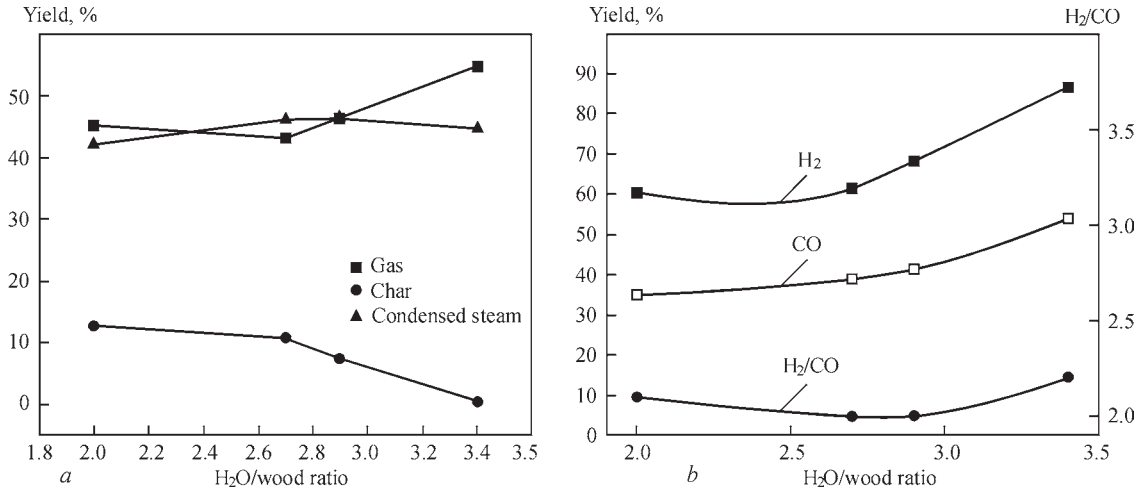

Figure 1. Effect of the H_2O and wood ratio on the product yield: *a* — total mass yield; *b* — yield of H_2 and CO gases, and the H_2/CO ratio

the high energy costs, which is a significant limiting factor for this technology.

Chemical processes modeling and experimental studies [21, 22] have shown that synthesis gas with high H_2 and CO content can be efficiently obtained from biomass waste using water-steam plasma. Timber conversion in a water-steam plasma environment was carried out under the following experimental conditions: wood consumption of 1.2 g/s, steam consumption of 2.63–4.48 g/s, plasma torch power of 49–56 kW. In the range of H_2O/wood ratios of 2.0–3.4, the average mass temperature was maintained at T = 2800 K. Timber was converted entirely into gas, liquid (water vapor), as shown in Figure 1, *a*, *b*. With a plasma torch power of 56 kW and an H_2O/wood ratio of 3/4, the residence time was sufficient to convert wood into gas, liquid, and charcoal. The yield of charcoal in the total mass of reaction products decreased to 0.5 %, and the gas yield increased to 55 %, which ensures a carbon conversion efficiency of up to 97.5 %.

It follows from Figure 1, *a* that the component of the mass balance is condensed incompletely reacted water, which was used as a plasma-forming gas. Thus, optimal organization of the conversion process is required. The amount of charcoal in the mass balance of the reaction products is reduced to 0.5 %, which indicates a great potential of thermoplasma technology for the efficient processing of organic materials. On the other hand, the low yield of carbon monoxide requires making the conversion process more selective. Therefore, special catalysts can be used to reduce the amount of carbon monoxide. Considering the inclusion of hydrogen energy in the energy balance and the comparison of biomass conversion methods into hydrogen from the point of view of the cost of energy consumption in kW·h/kg, technical and economic limitations, and environmental impact, it is crucial to increase efficiency, advance technology, and develop catalysts [23].

Plasma can be formed from air, O_2, water vapor, N_2, Ar, CO_2, or a mixture of these gases. Thus, plasma gasification is a promising source of obtaining renewable energy from solid waste and contributes to achieving sustainable development goals: affordable and clean energy, combating climate change, preventing waste from entering landfills and reusing resources, strengthening the concept of a circular economy. Plasma gasification of waste, unlike traditional incineration, reliably destroys highly toxic dioxins, benzopyrene and furans. High temperature destroys all resins, charcoal and dioxins, producing cleaner synthesis gas than conventional gasification. It should be noted that plasma gasification is the latest technology among modern waste disposal methods. Much work has been done to develop traditional gasification. According to the Council on Gasification and Syngas Technology, there are currently 272 gasification plants with 686 gasifiers in operation worldwide, and another 74 plants with 238 gasifiers are under construction. Most of them use coal as feedstock. Only five commercial plasma gasification plants are used worldwide for waste processing [24]. Recent efforts by developers in the field of plasma gasification are aimed at increasing the efficiency of the process, improving environmental and economic indicators through the development of advanced converter systems, gas cleaning, catalysts, monitoring and control systems, modular plant designs, improved materials and alternative energy sources. Plasma gasification is becoming an up-and-coming technology for waste disposal and energy production.

The Gasification Technologies Council website currently notes that there are operational plasma gas-

ifiers in Japan, Canada, and India. A new 2,000 tons per day MSW plant is being commissioned in Tees Valley, UK, which will be the largest plasma gasifier in the world when completed [25]. The Tees Valley One (TV1) plant, near Billingham, will process pre-treated municipal, commercial, and industrial waste supplied by Impetus Waste Management, diverting it from a nearby landfill. Billed as the "largest gasification plant in the world", it will use plasma gasification technology provided by Canadian company Alter NRG to convert waste into energy for the National Grid. It is expected to generate enough electricity to power 50,000 homes. The plant, which was granted planning permission by Stockton-on-Tees Council in 2011, is estimated to cost $500 mln (£320 mln) and is being funded almost entirely by US company Air Products, with One North East also providing a £260,000 grant in 2010 [25]. However, there have been challenges associated with design and operation. For example, several attempts have been made in South Korea to commercialise plasma waste recycling technology, but none have yet reached the commercialisation stage. However, this has not stopped development. The Korea Fusion Energy Institute, Hyundai Heavy Industries Power System Co., Ltd., and GS Engineering & Construction Co., Ltd. have agreed to develop a commercial plasma gasification furnace [26]. Under the agreement, the three organizations plan to collaborate closely in technology development, research and design of plasma gasification systems, development and manufacture of commercial equipment, and business development and implementation to commercialize plasma gasification technology. The development and construction of a commercial reactor capable of handling 100 tons of waste per day with a 500 kW plasma torch is planned, based on its experience in producing industrial circulating fluidized bed boilers.

It should be noted that there is currently no commercial H_2 production plant using plasma gasification technology from biomass. Significant research is needed to reduce energy consumption and thereby improve efficiency.

In general, hydrogen production technology from biomass gasification has not yet reached a high level of technological maturity. The main novelty of this work is to assess the current state of the art of H_2 production technologies from solid biomass, considering the technological, economic, and environmental indicators and the technical potential of hydrogen production through plasma gasification of biomass. According to the literature review, the normalized cost of hydrogen production can reach an average of 3.15 USD/kg H_2, and the average yield is 0.1 kg H_2/kg biomass biomass [27]. Meanwhile, the economic feasibility of hydrogen production from biomass may be hindered by the high cost, which ranges from 1.21 to 2.42 USD/kg for gasification and from 1.21 to 2.19 USD/kg for pyrolysis. Increasing the hydrogen yield and exploring methods to reduce the temperature are crucial to enhancing biomass gasification's economic viability and sustainability for hydrogen production, with special attention to energy saving [23].

According to the global hydrogen production outlook up to 2050 [28], electricity-based green hydrogen, produced by splitting hydrogen from water using electrolyzers, is expected to be the dominant form of production by mid-century, accounting for 72 % of production. This scenario would require excess renewable energy to power 3,100 gigawatts of electrolyzers. This is more than twice the total installed solar and wind capacity today. Blue hydrogen, produced from natural gas with emissions capture, plays a significant role in the short term (around 30 % of total production in 2030). Still, its competitiveness will decline as renewable capacity increases and prices fall. Making hydrogen projects competitive and economically viable based on excess renewable solar and wind energy to power electrolyzers remains challenging.

Natural gas reforming, coal gasification and water electrolysis are proven technologies for hydrogen production today and are used on an industrial scale worldwide. Steam reforming of natural gas is the most used process in the chemical and petrochemical industries. It is currently the cheapest production method and has the lowest CO_2 emissions of all fossil fuel extraction methods. Water electrolysis is expensive and is only used if high-purity hydrogen is required. With the expected increase in natural gas and coal prices, the gasification process is expected to be the most economical option starting around 2030. Biomass gasification for hydrogen production is still in its early stages today but will likely become the cheapest option for supplying renewable hydrogen in the coming decades. Biomass gasification is currently used in small, decentralized plants at an early stage of infrastructure deployment. In general, the hydrogen production mix is very country-specific. It depends heavily on expected feedstock prices, resource availability, and political support, which also play an essential role, especially for hydrogen from renewables and nuclear energy. Renewable hydrogen is primarily a cost-effective option in countries with a significant renewable resource base and/or a lack of fossil resources, for remote and sparsely populated areas (e.g., islands), or for storing excess electricity from intermittent renewable energy sources. Otherwise, renewable hydrogen should be incentivized or mandatory.

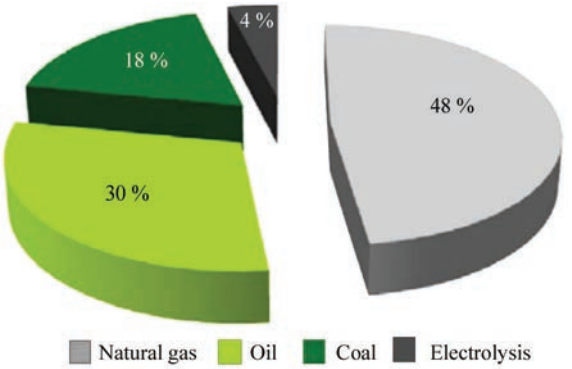

Figure 2. Current raw materials used for H_2 production [30]

In the long term, hydrogen must be produced using processes that avoid or minimize CO_2 emissions. Renewable hydrogen, whether produced by electrolysis from wind, solar energy, or biomass, is undoubtedly an endpoint (especially in climate change mitigation), but is not a prerequisite for introducing hydrogen as an energy vector. Until this goal is achieved, hydrogen produced from fossil fuels will predominate. Still, capturing and storing the resulting CO_2 becomes a prerequisite for hydrogen to contribute to the overall reduction of CO_2 emissions in the transport sector. The predominance of fossil hydrogen is expected from about 2030, as reflected in the various hydrogen roadmaps, as is the subsequent role of renewables. The specific costs of producing hydrogen from renewables are not considered competitive with most other options in this period, except for biomass. The cost of hydrogen production depends mainly on the assumed prices of the feedstock. The typical price range up to 2030 is between 0.08 and 0.12 USD/kW·h (2.6–4 $/kg). In the long term, up to 2050, with the expected increase in raw material (fossil fuel) prices and CO_2 prices, hydrogen production costs will also increase [29].

Based on the above, biomass provides renewable and sustainable energy in other forms such as syngas, biogas and hydrogen. Hydrogen energy has great potential for decarbonizing various sectors due to its versatility. At the same time, hydrogen energy production is considered environmentally friendly. However, even though the main precursors to produce hydrogen gas are readily available in various countries, these resources are not yet used and, as a result, hydrogen gas is not included in the energy balance of states [23].

Thus, today, hydrogen is mainly produced from fossil fuels (Figure 2) [30]. Hydrogen production from biomass through gasification can become a favorable alternative for future decarbonization applications based on renewable and carbon dioxide-neutral hydrogen.

However, it should be noted that biomass accounts for about 14 % of global energy consumption, which is higher than coal (12 %) and comparable to gas (15 %) and electricity (14 %). Biomass is a significant energy source for many developing countries, but much of it is non-commercial [31, 32].

Figure 3 shows the future trend of hydrogen supplies for three developed countries/regions — the US, EU, and Japan. As can be seen, hydrogen supplies will largely depend on fossil sources – natural gas and coal. Carbon capture and sequestration technologies are planned to be important in achieving climate goals. However, the amount of hydrogen produced from renewable sources should also increase significantly. It becomes clear that hydrogen supplies depend on regional differences in resource endowments. While Japan includes renewable electricity only as a source of renewable hydrogen, the EU and the US plan to increase hydrogen production through biomass gasification [33].

Numerous papers review current possible principles of industrial hydrogen production based on biomass gasification. Generally, hydrogen from renewable sources can be produced electrochemically, biochemically, or thermochemically. All three methods allow hydrogen production without CO_2 emissions (Figure 4). H_2@Scale is a US Department of Energy (DOE) initiative that brings together stakeholders to advance affordable hydrogen and reve-

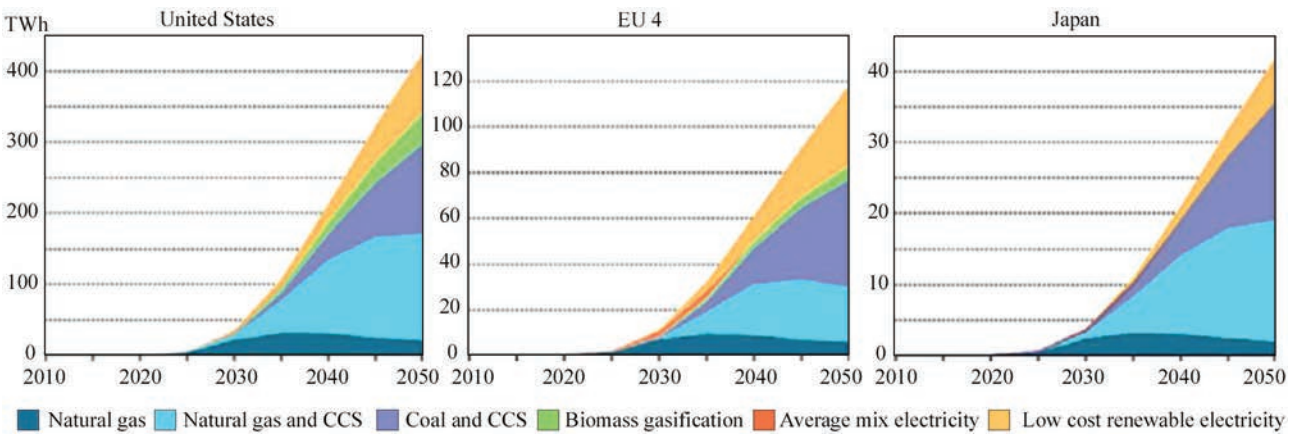

Figure 3. Hydrogen supply trends [33]

nue-generating opportunities in various energy sectors. It includes DOE-funded projects and activities jointly funded by national laboratories and industry to accelerate early-stage research and demonstration of hydrogen technologies.

This study focuses on the thermochemical approach through biomass gasification (wood chips, agricultural waste). Specifically, the potential industrial production of hydrogen is considered with an emphasis on plasma gasification technologies. Figure 5 shows the general scheme of the hydrogen production process by plasma gasification.

The scheme includes gas cleaning and enrichment, which are necessary to remove CO and CO_2, as well as trace components such as H_2S, HCl, and fly ash.

There are many differences in the characteristics of biomass. Solid biomass fuels commonly used in large-scale power plants include agricultural residues, short-rotation energy crops, and others. Their compositions vary significantly in the proportions of volatile matter and fixed carbon. Most lignocellulosic biomass (e.g., woody and herbaceous materials) has about 75–85 % volatile matter and about 15–17 % fixed carbon. Biomass varies significantly in physical characteristics, density, and thermal properties. Density ranges from 200–300 kg/m^3. Thermal conductivity for biomass particles is from 0.05 W/(m·K) for some herbaceous materials and from 0.1 to 0.15 W/(m·K) for woody materials [34]. A future industrial gasification system will likely use various available biomass resources. Therefore, the design will need to consider the variability of fuel combustion characteristics. To ensure optimum efficiency, it is necessary to control particle size, predict the behavior of inorganic components in the reactor, particularly the role of potassium, and control fouling and ash deposition effectively.

Plasma gasification involves a sequence of solid mass loss phases, including drying, pyrolysis — volatiles yield, and charcoal formation and gasification. This is followed by homogeneous partial oxidation of the volatiles approaching thermodynamic equilibrium and completion of the water shift reaction. Oxidation of both volatiles and charcoal occurs in the absence of O_2 at a rate proportional to the available O_2 and temperature.

The plasma torch is an independent source of concentrated heat, which allows the reactor temperature to

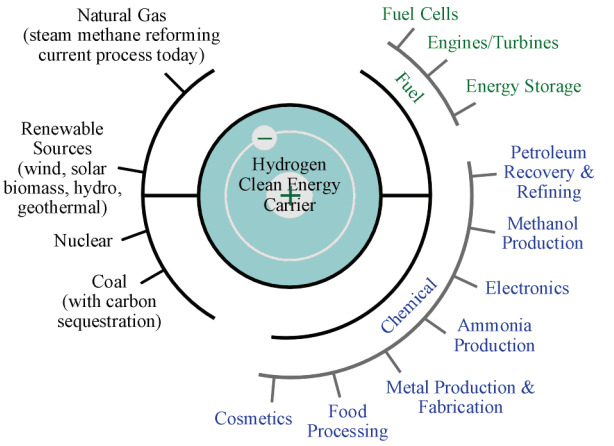

Figure 4. H_2@Scale vision for hydrogen production, including from renewable sources, and its use

be controlled independently of variations in feedstock quality and air/oxygen/steam supply required for its gasification. Optimum parameters can be established and easily maintained and are not affected by the state of the material being processed. This provides significant advantages in process variability compared to gasification without an external heat source. Plasma can be effectively used in each phase of the process, providing a considerable increase in efficiency within the framework of the strategy for converting feedstock into specified gasification products. However, its preferred place of use follows the process's logic.

A thermal analysis of weight loss was performed for five types of biomass pellet fuel. The heating rate of 20 °C/min is indicative for the assessments. TG and DTG curves were obtained (Figure 6, *a*, *b*) [35].

It can be seen from Figure 6 that the pyrolysis of five kinds of biomass pellet fuel mainly includes three stages: *1*, water evaporation stage; *2*, volatile matter release stage; *3*, fixed carbon oxidation stage. In the first drying stage, from room temperature to about 170 °C, the peak weight loss temperature is at 100 °C, and the weight loss at this stage is about 10 %. During heating, pellets absorb heat to evaporate water (free water, crystal water, absorbed water, etc.). This is the drying stage of the five kinds of biomass pellet fuel, and its composition has not changed significantly. The second stage is volatile matter release at about 190–450 °C. This is the stage of the main weight loss of the five kinds of biomass pellet fuel and the formation of the initial carbon layer. The main chemical components in the five types of biomass pellet fuel

Figure 5. General technological scheme of hydrogen production by plasma gasification

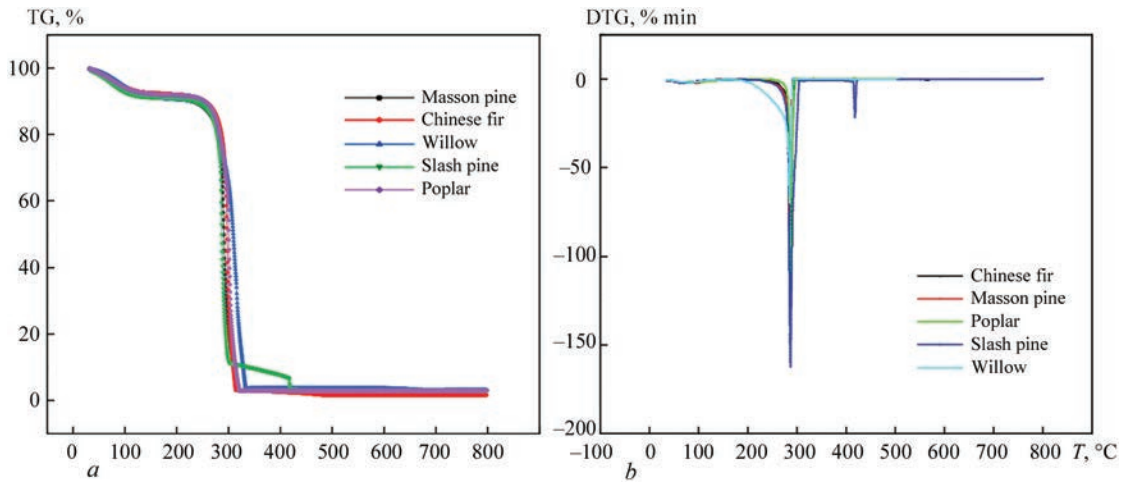

Figure 6. Thermal analysis of weight loss of biomass fuel (conducted for five types of biomass pellet fuel): *a* — TG curves; *b* — DTG curves [35]

are cellulose, hemicellulose, lignin, etc. The weight loss at this stage is about 75 %. The third stage is after 450 °C, where slow oxidation and decomposition of the carbon layer occur. The weight loss at this stage is about 10 %. The pyrolysis of organic matter in the five types of biomass pellet fuel is complete. Residual ash and other non-decomposable substances remain. The gasification results of the five types of biomass pellet fuel are approximately the same.

It is essential to characterize the fuel in measured durations of the various gasification stages to optimize the process for productivity and reaction completeness. Such valuable data for predicting the mass loss behavior of different particle sizes will inform operators about the need to adjust milling and temperature requirements [36] presents an experimental method for investigating the durations of the various combustion stages of individual particles for three types of wood biomass fuels. The volume of data obtained allows the evaluation of empirical expressions for the relationship between particle mass and the duration of volatile release and combustion of charcoal.

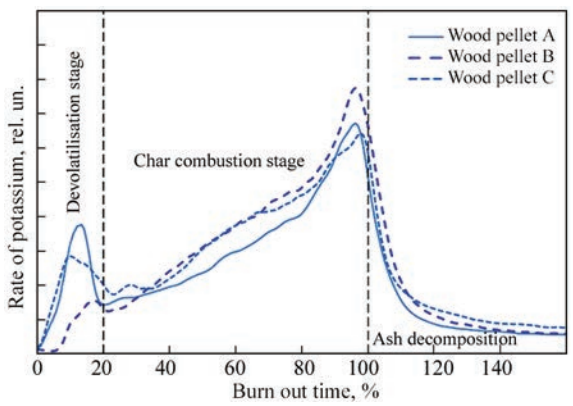

Figure 7. Time dependences of combustion of three types of wood pellets with the release of potassium and indication of the gasification stages [38]

The combustion temperature of biomass in large power plants reaches up to 1600 K. Such temperatures influence the separation of inorganic components through phase changes. In biomass fuels, particularly potassium, can be present in various forms and pass into the gas phase during combustion at elevated temperatures. Subsequently, the combustion products cool and condense on the surface of the furnace and heat exchangers. Potassium chloride and hydroxide lead to an increase in corrosion deposits and ash adhesion. Potassium in the gas phase can also lead to the formation of sulfate aerosols and recombine with other solid-phase components of ash, affecting the behavior of ash during melting and, consequently, affecting the formation of carbon and slag in the furnace [37]. The pattern of potassium release obtained in experiments on the combustion of various types of wood pellet fuels is shown in Figure 7 [38]. These data allow us to trace the physical mechanisms of the process and contribute to the development of models for the gasification of biomass particles.

As Figures 6 and 7 shows, the limiting stage of biomass gasification is the gasification of the carbon layer. Since the authors developed the theme of generating a plasma mixture of water vapor and atmospheric pressure oxygen using an electrodeless discharge to process biomass to obtain hydrogen [39], the main attention should be paid to the gasification of the carbon layer.

Oxygen and steam are the preferred gasifying agents for producing hydrogen-rich synthesis gas [40]. One of the key factors affecting the process performance is the steam-to-oxygen ratio at the reactor inlet. Both laboratory and industrial test data show that a higher steam-to-oxygen ratio also increases the water gas shift reaction rate. As a result of the influence of the steam-to-oxygen ratio on the thermodynamic and kinetic properties of the process, higher

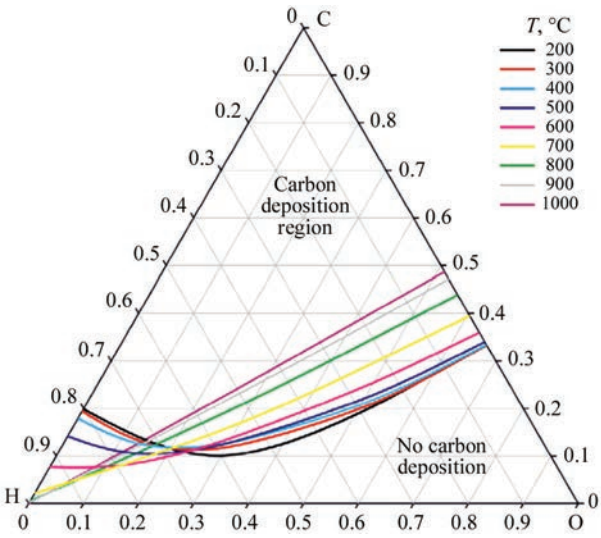

Figure 8. Ternary C–H–O diagram for the solid phase of all carbon allotropes at a pressure of 1 bar [41]

values result in higher CO conversion and lower CO content in the outlet gas. In addition to CO conversion, the steam-to-oxygen ratio can also affect the production of hydrocarbons (primarily methane) from the reaction:

$$2CO + 2H_2 \leftrightarrow CH_4 + CO_2 \ (\Delta H = -244 \text{ kJ/kmol}).$$

A minimum steam-to-oxygen ratio of ~0.4 at the reactor inlet should be ensured to minimize such undesirable reactions. In addition, a certain amount of steam prevents the risk of coking and carbon deposition on the surface. Depending on the feedstock fed to the reactor, typical steam to oxygen molar ratio ranges from 0.6 to 2.2, and the steam to carbon ratio varies between 2.8 and 4.2. Figure 8 [41] shows the ternary C–H–O diagram for a pressure of 1 bar, indicating a zone with thermodynamic preference for coking and carbon deposition.

To increase the yield of H_2 and reduce the CO content in the generated synthesis gas, the water shift reaction:

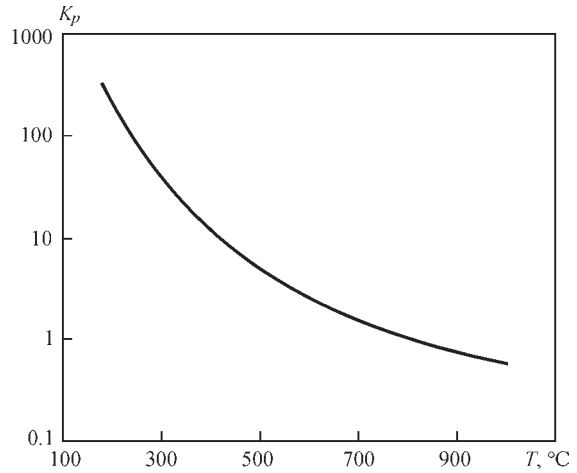

Figure 9. Change in the equilibrium constant (Kp) for the water gas shift reaction depending on temperature [42]

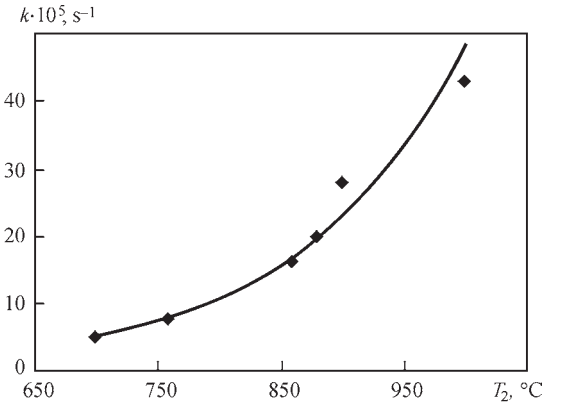

Figure 10. Effect of temperature in the feedstock layer on the carbon conversion rate [43]

$$CO + H_2O \leftrightarrow H_2 + CO_2 \ (\Delta H = -41.2 \text{ kJ/kmol}),$$

is a well-established technology in industrial large-scale hydrogen production plants, or to set the syngas' CO/H_2 ratio.

The water shift reaction converts carbon monoxide and steam into hydrogen and carbon dioxide. The equilibrium constant decreases with temperature, so high conversions are favored at low temperatures, as shown in Figure 9 [42].

When superheated water vapor is used as a heat carrier and reagent for carbon conversion, the conversion rate increases with increasing temperature (Figure 10) [43].

This is entirely consistent with the concepts of thermal activation of chemical processes — with an increase in temperature, their speed increases, and the increase in temperature is ensured by the rise in the temperature of water vapor, i.e. with an increase in the temperature of the vapor, the conversion rate and the depth of the reactions increase. Figure 11 [43] shows typical results of a study of the kinetics of gas evolution in the gasification process of carbonized coal.

The main process of carbon with water vapor interaction:

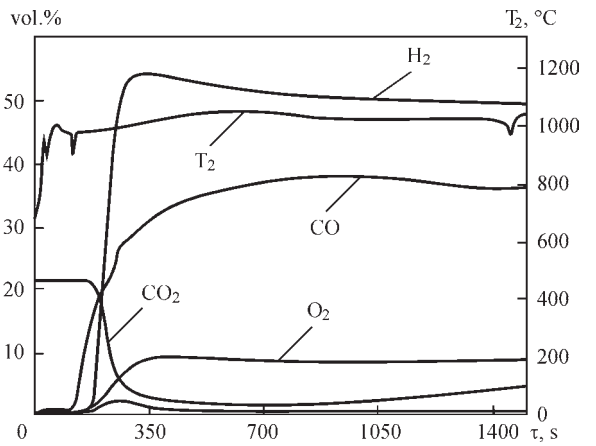

Figure 11. Dependence of the yield of gaseous products of coal gasification on time

$$C + H_2O \rightarrow CO + H_2.$$

The following dependencies on Figure 11 are noteworthy. During the gasification process, the hydrogen concentration decreases while the oxygen content in the mixture increases. At the same time, the ratio of CO and CO_2 concentrations remains virtually unchanged throughout the process. The amount of hydrogen in the reaction products decreases due to its oxidation by oxygen according to the reaction:

$$2H_2 + O_2 \rightarrow 2H_2O,$$

in this case, oxygen obtained by the reaction $CO_2 \rightarrow$ $\rightarrow C + O_2$ is used. This reaction itself becomes possible, on the one hand, due to the oxidation of CO by superheated water vapor $CO + H_2CO \rightarrow CO_2 + H_2$, and on the other hand, due to the presence of mineral impurities in coal that have catalytic activity in the reaction $O_2 \rightarrow C + O_2$ [44].

Based on the above assessment of the state of the art in large-scale biomass gasification, the projection onto plasma technologies today is as follows. Plasma has been recognized as an effective method for destroying hazardous waste for decades. However, plasma generators consume a lot of electricity. As a result, the rising cost of electricity and pollution from coal-fired power plants have made plasma an expensive and environmentally questionable disposal method. Until 2000, most research into plasma use for waste recycling aimed at achieving complete pyrolytic decomposition as far as possible. Nevertheless, the more sophisticated the process, the higher the power consumption. Even with large volumes of waste destroyed, pyrolytic gasification requires much more energy than it produces. Only when the cost of eliminating the hazard posed by the waste is very high does plasma become an economically viable method of waste destruction [45]. Currently, the thermal processing industry is studying ways to analyze and optimize the efficiency of installations [46, 47]. A sensitivity analysis of the operating parameters of the plasma gasification process was performed to maximize the net energy produced and minimize the plant cost. Where available, correlations from the literature and market data were used to calculate the capital and operating costs of the process. For example, a case study of a plasma gasification plant processing 750 tons of municipal solid waste per day was conducted in Greece. This analysis showed that the cost of the plasma gasification process is comparable to the conventional incineration process. In addition, plasma gasification has produced better environmental and technical results [46]. This fact offers a new framework for reconsidering the historical cost and energy consumption issues that have previously limited the development of plasma processing. To compete with fossil fuel-based technologies, large-scale gasification plants still require significant technological development supported by economic subsidies and incentives, efficient operating strategies, and global policies pushing for carbon-neutral solutions. The work [48] shows that specific investments tend to decrease over the years, for gasification plants designed to produce electricity, cogeneration energy and liquid biofuels (Figure 12).

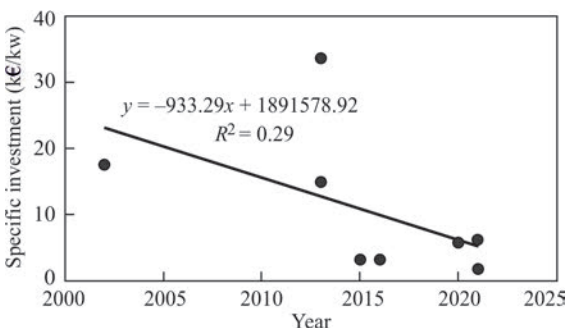

Figure 12. The relationship between investment and year, as well as the corresponding linear regression equation for electricity, cogeneration plants and biofuel gasification plants [48]

While plasma gasification has many advantages, some disadvantages need to be considered before investing in this technology. One of the main disadvantages of plasma gasification is its high cost. The process requires expensive equipment and trained personnel, making it prohibitively expensive for many individuals and organizations. Additionally, the high cost of plasma gasification can make it difficult to justify the price, especially when cheaper methods are available. Another disadvantage of plasma gasification is that it requires specialized training. Individuals wishing to perform the procedure must undergo extensive training to operate specialized equipment safely and effectively. Overall, plasma gasification offers a promising solution to reducing reliance on traditional waste management methods while helping to become more environmentally friendly. Like any other technology or process, this method has advantages and disadvantages that need to be considered. The challenge for those considering using plasma in waste processing is to achieve low energy consumption, high energy value of the gas, low capital and operating costs, and long equipment uptime.

To meet the requirement for long operating times, microwave [49] and induction plasma [50] are currently being considered. The emergence of new plasma technologies in thermochemical conversion methods may open up new avenues for the economical production of H_2 and value-added products. Plasma gasification has been developed commercially, typically using direct current plasma discharge technolo-

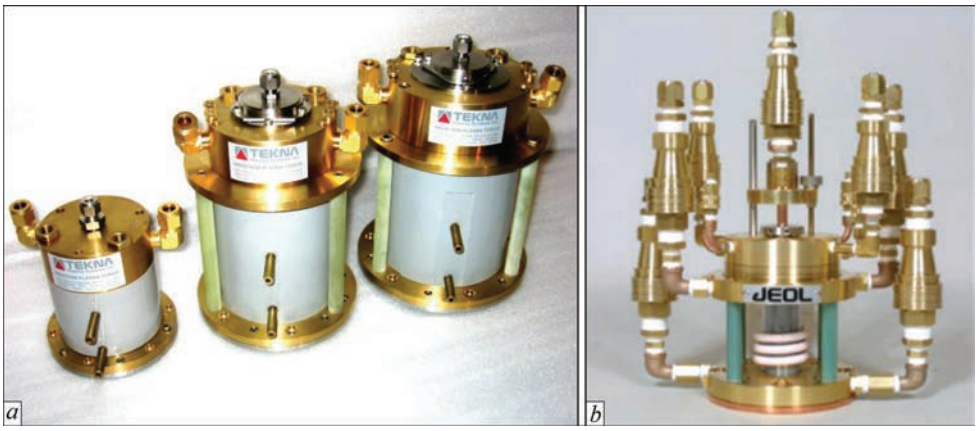

Figure 13. High-frequency induction plasma torches: *a* — Tekna (from 40–200 kW); *b* — JEOL

gy [51]. However, direct current torches suffer from short electrode life in the presence of oxidizing gases, leading to inconvenience and high operating costs associated with their replacement. An alternative is the use of electrodeless plasma torches.

For small and industrial scale waste recycling, three types of advanced thermal plasma technologies are considered: DC atmospheric plasma torches, radio frequency plasma torches and microwave plasma torches. The authors of [52] conducted a comparative study of all three plasma torches for energy and waste recycling applications. The simulation modelling and experimental results were presented with an indirect DC plasma torch and a high-frequency induction plasma torch. The results show that DC plasma torches and high-frequency induction plasma torches are economical and beneficial for large-scale waste recycling and energy production. Meanwhile, a microwave plasma torch can be used for small-scale waste recycling. Overall, minimizing the environmental impact and cost-effectiveness of the process are the most critical parameters to improve the feasibility and sustainability of plasma-based waste recycling plants. High-frequency induction plasma torches with plasma power from 15 to 200 kW are designed for more than 10,000 hours of non-stop operation [53]. They have found application in the chemical and metallurgical industries due to their high reliability and long service life without parts replacement (within 2–3 months).

Modern high-frequency induction plasma torches from TEKNA [54] and JEOL [55] (Figure 13) have reached a prominent level of perfection and meet the requirements for a plasma gasification system.

For adequate control of gasification processes and developing and optimizing plasma reactors, reliable information about the RF discharge and plasma torch parameters is necessary. The task is simplified in biomass gasification since the jet induction plasma torch operates for a long time in one mode. The extended laminar torch of the optimized induction plasma torch has well-filled temperature and velocity profiles (Figure 14, *a–c*) [56]. It should be noted that many studies have been conducted on the temperature and velocity of the jet of induction plasma torches by direct measurements, using probes and optical emission spectra. For clarity, the calculated picture of the temperature and velocity fields in the torch of the plasma torch induction is given here; it agrees with the experiment.

The torch was modeled in ANSYS Fluent; the geometry was meshed to discretize the space. The mesh independence study was performed by refining the cell size, which is expressed as the number of cells per millimeter of axial distance.

The industry uses high-frequency induction (HFI) plasma torches for various applications. To get more benefit, many attempts have been made to improve the HFI plasma torch, which included optimizing its operating conditions, size and shape. However, the optimization efforts [57–59] did not produce long-term results, leaving the original design proposed by Reed [60] in the 1960s, which remains virtually unchanged. However, recent efforts [61] have been revived and developed in [56]. A significant improvement is achieved by using conical geometry (Figure 13, *b*). This geometry significantly reduced gas and power consumption and improved performance. Special HFI plasma torches shown in Figure 13 are available to operate with every class of HF power sources. They feature highly efficient designs to maximize plasma thermal processing effects, excellent ruggedness and stability. Adopts dual-pipe water cooling system: the inner tube is made of ceramic with higher strength than quartz tube, which ensures stable operation for a long time under atmospheric pressure, under ultra-high temperature and strong oxidizing environment such as HCl, HF, or HBr.

In the first years of studying the HFI plasma, experimenters used available power sources (tube generators) and the first results were obtained in a wide frequency range from 0.5 to 60 MHz. Later,

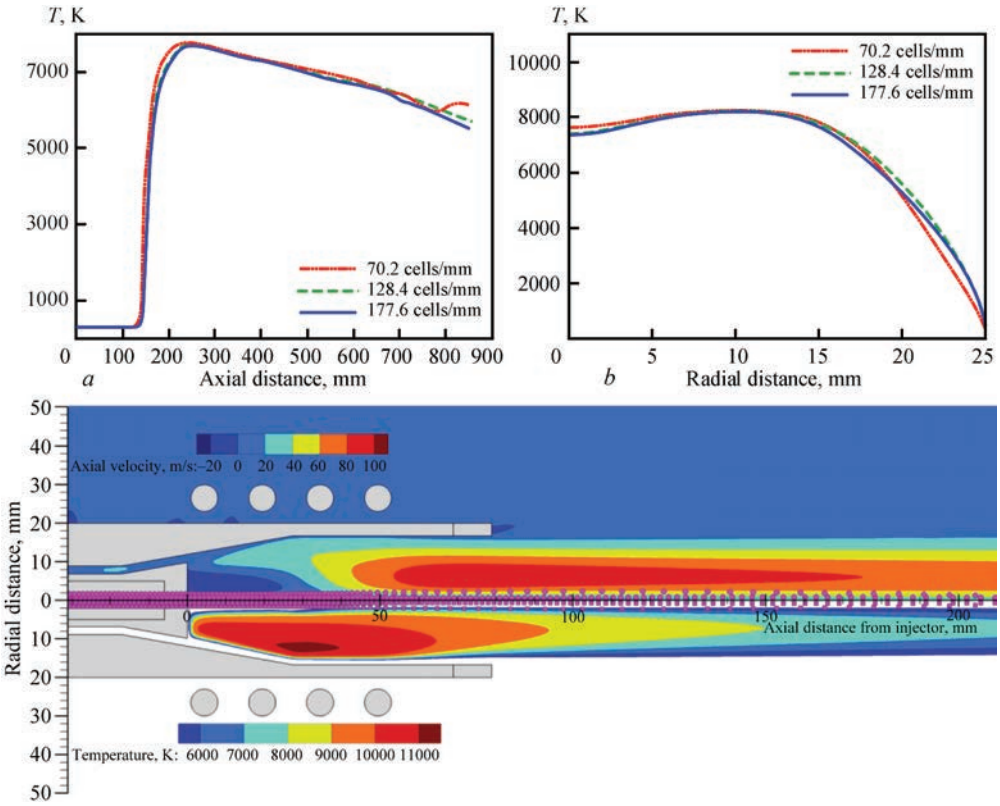

Figure 14. Parameters distribution in the torch of a conventional high-frequency induction plasma torch: *a* — temperature along the central axis for different cell sizes; *b* — radial distribution of temperature at the plasma torch outlet for cells of various sizes; *c* — contours of axial velocity and temperature

a standard series of frequencies of 0.44, 1.76, and 5.28 MHz and oscillatory powers of 60, 160, and 1000 kW tube generators were established [62]. The most important consumer of energy is the generator tube. Energy losses at the anode of the generator tube are 25–33 % of the total electricity consumed; this circumstance determines the entire energy of HFI plasma installations. A good frequency for HFI plasma torches is 5.28 MHz and higher; losses in a metal plasma torch are 1.3 % of the consumed power. A frequency of 1.76 MHz from the point of view of using a metal plasma torch is considered the limiting one, below which one should not go — losses are already 4–6 %. At a frequency of 0.44 MHz, the losses in the plasma torch, inductor, and circuits become equal to those in the generator lamp. The overall efficiency of the HFI plasma installation on the generator lamp at a frequency of 1.76–5.28 MHz is 60–64 %.

High-frequency induction plasma torches, which can currently become the main link in the technological process, with a plasma power of 15 to 200 kW, are designed for more than 10,000 hours of continuous operation. The strategy is to combine gasification and maximum gas purification in a single reactor to obtain high-quality and heat of combustion synthesis gas. Energy recovery and combining primary purification with gasification make the system more compact, reduce heat losses and take up less space in the plant. Increasing the purity of the gas leaving the biomass gasification system, eliminating tar contaminants, maximizing the reduction of alkali metals, solid particles, nitrogen (N_2), sulfur (S), and chlorine (Cl_2) simplifies filtration and purification with the minimization of catalysts and sorbents.

The new concept of organizing the technological process and constructing a reactor using plasma induction ensures a uniform gas-dynamic regime throughout the volume of the gasification zone and an effective and uniform thermal effect on the entire volume of the solid carbon-containing material and the gas phase in the gasification zone, and, consequently, a uniform distribution of temperature and concentrations in the gasification zone. This contributes to the creation of uniform conditions for chemical reactions both in the solid carbon-containing material and in the gas phase, as well as a stable composition and high energy indicators for obtaining synthesis gas with the maximum approximation to thermodynamic equilibrium [50]. Super-equilibrium surface heating from the jet of high-enthalpy dissociated gas mixture of the induction plasma torch is expected [63]. The effect of super-equilibrium heating is observed when a dissociated chemically nonequilibrium gas flow generated by the induction plasma torch flows around a surface with non-uniform catalytic properties. When passing from a non-catalytic to a catalytic surface re-

gion, there is a jump in the heat flux and temperature to levels significantly exceeding the values obtained on a fully catalytic surface or in the case of an equilibrium boundary layer. The effect is due to the fact that, under identical external flow conditions, the concentration of dissociated gas atoms in the boundary layer on a non-catalytic surface is higher than in the case of a catalytic surface, and their recombination further downstream on the catalytic surface leads to its additional heating. In experiments with a sample, sections of which were coated with chromium-nickel spinel, the temperature behind the transition line from the low- to the highly catalytic surface region exceeded the temperature measured in the same area during flow around a fully highly catalytic surface by 140 °C [64]. In subsonic jets of dissociated air on a flat, highly catalytic surface, heat fluxes with a density of 150 to 3750 kW/m^2 were realized. This phenomenon is fundamental at the gasification stage of solid carbon mixed with ash residue.

The key issue in scaling up plasma gasification of biomass is the specific energy consumption of electricity per kilogram of waste. Let us present several illustrative processes. Calculations of plasma gasification processes of waste in a shaft reactor made it possible to estimate energy costs and outline ways to reduce them [65]. Figure 15 shows the dependence of the productivity of the gasification process on the average statistical composition of waste on the power of an external energy source. The heat of combustion was within 7–10 MJ/kg with a mass fraction of carbon and hydrogen in the feedstock of 20–30 %. For comparison, the heat of combustion of sunflower husk biomass is 19.4 MJ/kg with a mass fraction of carbon and hydrogen of 54 %. In the shaft plasma furnace, for which the dependencies were obtained (Figure 15), moisture is used as an oxidizer, determining the initial moisture content of the raw material, and plasma torches can operate with the supply of superheated steam or air, the oxygen of which acts only as an additional oxidizer in the gasification process. For the adopted furnace scheme, with an increase in the temperature in the reactor, there is an increase in electrical energy consumption, but the potential energy of the synthesis gas increases by the same amount. With an increase in temperature from 1100 to 1300 °C, the hydrogen content in dry synthesis gas decreases from 57.5 to 57 %, and the CO content increases from 34 to 36.5 %. Here, the required mass flow rate of the oxidizer does not exceed 5–7 % of the mass flow rate of the resulting synthesis gas. Electrical energy consumption from 0.68 kW·h/kg (humidity close to zero) to 1.5 kW·h/kg (humidity 0.15 g/kg). The main conclusion is that new technologies for processing

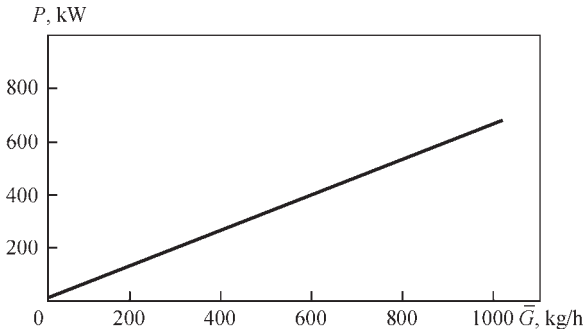

Figure 15. Dependence of the productivity of the waste gasification process on the power of an external energy source [65]

carbon-containing waste accepted for implementation should be based on using oxygen and superheated water vapor to temperatures >1000 °C as an oxidizer.

New technologies should be implemented in weakly oxidizing and reducing atmospheres and have two spatially separated zones: a medium-temperature zone (T < 1000 °C) for drying, pyrolysis and gasification, and a high-temperature zone (T > 1300 °C) for completing the gasification processes, removing the inorganic part of the waste and heating the gaseous product (gas synthesis) to the optimum temperature.

In [66], the use of plasma technology for processing biomass (BM) in the form of mixed manure of cattle, horses, sheep, goats and pigs (moisture content 30 %) is analyzed. The characteristic composition of the biomass (manure) is as follows in mass %: H_2O — 30; C — 29.07; H — 4.06; O — 32.08; S — 0.26; N — 1.22; P_2O_5 — 0.61; K_2O — 1.47; CaO — 0.86; and MgO — 0.37. Most of the organic matter consists of cellulose ($(C_6H_{10}O_5)_n$) and some organic sulfur (S). BM consists of 95.21 % organic matter; the mineral content is 4.79 %. The biomass has a calorific value of 16 MJ/kg. The following mixtures by weight were used for plasma gasification and pyrolysis: 100 % BM + 25 % air and 100 % BM + 25 % nitrogen, respectively. Experimental studies of plasma-chemical gasification and pyrolysis of BM were conducted on a setup whose main elements were a direct-current plasma torch (nominal power 70 kW) and a plasma-chemical reactor with a BM capacity of about 50 kg/h. The degree of gasification and specific energy consumption of the plasma are shown in Figure 16.

It is evident from Figure 16 that the degree of gasification increased with increasing temperature in both cases, but it was slightly faster for gasification than for pyrolysis. However, at a temperature of 950 K, the degree of gasification reached 100 % for both processes. When comparing the parameters of the plasma treatment of biomass, the calculated and experimental data showed satisfactory agreement, with a discrepancy of no more than 16 %. The plasma-treated biomass products were free of harmful impurities in calcula-

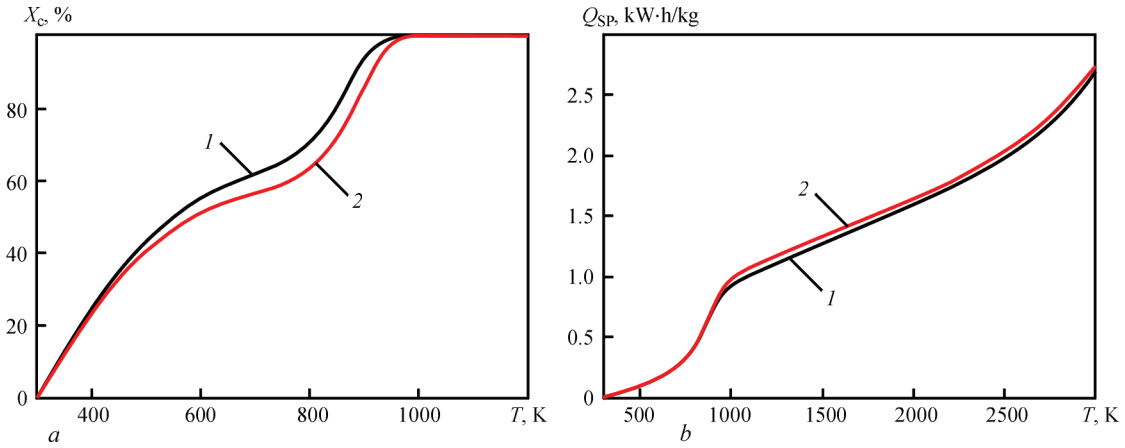

Figure 16. Dependence of the degree of gasification (*a*) and energy consumption of plasma (*b*) during gasification of biomass-manure on temperature: *1* — plasma gasification; *2* — plasma pyrolysis [66]

tions and experiments, confirming the environmental benefits of plasma treatment. Using the exergy coefficients of the heat of combustion of biomass, it was concluded that plasma gasification of biomass is 25 % more efficient than traditional combustion.

The possibility of gasification of wood pellets to synthesis gas in a thermal air plasma environment was determined [67]. The influence of the plasma torch power, plasma-forming gas consumption, and equivalence coefficient on biomass gasification was analyzed. The synthesis gas yield varied from 59.95 to 62.51 %, and the H_2/CO ratio ranged from 0.68 to 0.8. The highest concentrations of H_2 and CO in the resulting gas were 26.6 and 33.35 %, respectively, which gave an H_2/CO ratio of 0.8. The net calorific value of the resulting synthesis gas varied from 7.62 to 8.82 MJ/Nm^3. The carbon and energy conversion coefficients were 85.3–97.2 and 29.23–30.57 %, respectively. Specific energy consumption varied in the range of 165.47–195.61 kJ/mol of synthesis gas. At the same time, the particular energy consumption for wood waste gasification and gasification efficiency were 2.49 kW·h/kg and 82 %, respectively. In addition, the energy and mass balance assessment showed that when gasifying 20.73 kg/h of wood pellets, the resulting synthesis gas can produce 15–18 kW·h and 111–114 kW·h of electrical and thermal energy, respectively.

Of the three biomasses studied [68] (sugar cake, rice husks and sawdust), sawdust is the most suitable for the process of obtaining hydrogen-rich synthesis gas, since it can produce more hydrogen (~97 g/kg biomass). However, plasma torches require higher electricity consumption (2.23 kW·h/kg biomass). In this sense, rice husk shows the worst results with a maximum specific hydrogen production of 54 g/kg biomass at 27.5 kW·h/kg of produced hydrogen. As a conclusion, this study confirmed that plasma gasification with an air-steam mixture as a gasifying agent can be used to produce hydrogen-rich gas with specific production in the range of 1.79–2.80, 1.68–2.37, and 2.09–2.81 Nm^3/kg from sugar cake, rice husk, and sawdust, respectively. And with lower electricity consumption per kilogram of hydrogen than aqueous hydrolysis.

Atmospheric pressure plasma jets are the main tool for gasification. It is estimated that the plasma torch consumes only 2–5 % of the total energy input into the gasification system, and up to 80 % of the total energy input into the feedstock can be recovered in the produced synthesis gas. In 2010, Scientific Certification Systems (SCS) reported that the plasma gasification process resulted in the lowest greenhouse gas emissions for the same amount of energy, with approximately 31 mln tons less CO_2 equivalent/MWh compared to landfill with energy recovery and approximately 50,000 tons less CO_2 equivalent/MWh compared to natural gas combustion [69]. However, based on the above results and the goals of sustainable energy development, integrating highly efficient biomass gasifiers of any type into advanced production systems will occur on a comparative basis in the future global energy market. In recent years, manufacturers have made numerous efforts to reduce the cost of implementing biomass gasifiers. The main inhibitory factor is the higher cost of purchasing plasma equipment in the proposed cycle compared to traditional processes and the use of complex equipment. This study assesses the place of an improved plasma cycle for producing high-power and efficient energy sources. The reduction in equipment cost is directly related to the reduction in electricity consumption by plasma burners (kW·h/kg biomass) while maintaining efficiency. Reduction in overall energy consumption of the system can be achieved by optimizing energy flows in the gasification reactor — minimizing the Gibbs free energy [70] and using plasma not only as an additional heat source, but also for local stimu-

lation of chemical reactions in the superequilibrium heating zone. The following should be considered. 1. The temperature of the exhaust synthesis gas is high, 1000 °C and above, and there are many opportunities for waste heat utilization in addition to the input of plasma energy and partial combustion of the waste material. The authors performed energy optimization of the biomass gasification system using high-temperature effluent synthesis gas for preheating the incoming water vapor. 2. Using high-volume HFI plasma (Figure 14) increases the effective area available for interaction with surfaces. 3. Using HFI plasma for local super-equilibrium heating and stimulation of chemical reactions. The reactor scheme adopted for modeling is shown in Figure 17.

Fulfilment of these conditions creates preconditions for reducing the plasma equipment's installed capacity with corresponding weight, dimensions and cost reduction. As a rule, RFI plasma equipment includes a power source (radio frequency generator and matching network), plasma torch and reactor. Most processes based on HFI plasma use equilibrium plasma in the temperature range of 8000–12000 K. Regarding commercial application of RFI plasma up to now it is mainly powder processing and space research, as well as some environmental applications: dissociation of hydrogen chloride, treatment of medical waste [71], decomposition of polyvinyl chloride (PVC) [72]. HFI plasma at low pressures is not considered here; only thermal plasma with high enthalpy is considered. The HFI method is essential for obtaining thermal plasma with high gas temperature at high pressures for biomass and waste processing gasification. Several problems require further study and development, such as the excitation of the HFI plasma discharge at atmospheric pressure and the efficiency of the HFI power supplies. They are based on the oscillator tube in the electrical circuit of the power electronics (Figure 18) [59, 61, 73]. Common problems in plasma generation are: size — HFI generators are usually large, heavy units; reliability — generators use tubes with a limited life; efficiency — generators with a power tube have always been inefficient. The reasons are: power losses — most of the power is dissipated in the tube; low reliability — in generators using power tubes, they are replaced approximately every two years, depending on the use; high voltage of the order of 10 kV is present in the generator, which increases the likelihood of failure; maintenance problems — generators are complex elements that require labor-intensive procedures for repair if a malfunction occurs. Most modern plasma HFI generators are beginning to use solid-state electronic components. This significantly reduces the size of contemporary plasma generators and is much more suitable for operation. HFI generators with an efficiency of 90 % and higher are currently successfully used at low-pressure and low-power plasma torches. Solid-state HFI generators (like Figure 19) of high power (>25 kW) are under development.

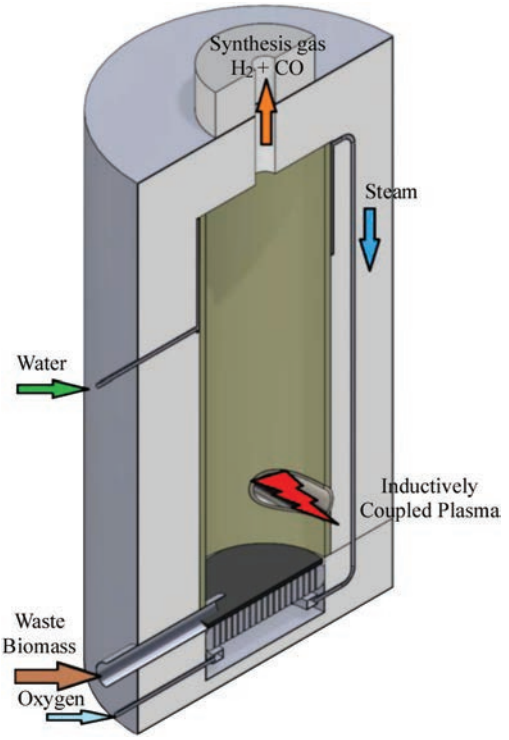

Figure 17. Scheme of the reactor adopted for modeling

Figure 19 shows the electrical circuit of the solid-state power supply for the HFI plasma torch [74].

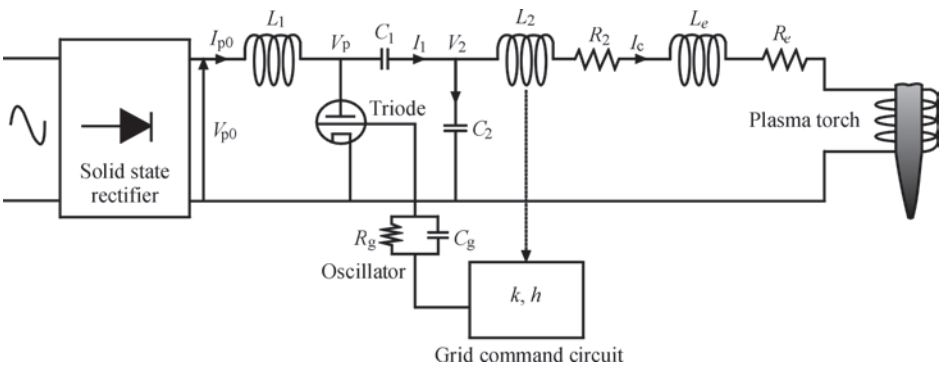

Figure 18. Typical structural electrical diagram of the power source of the HFI plasma torch with a generator lamp [59, 73]

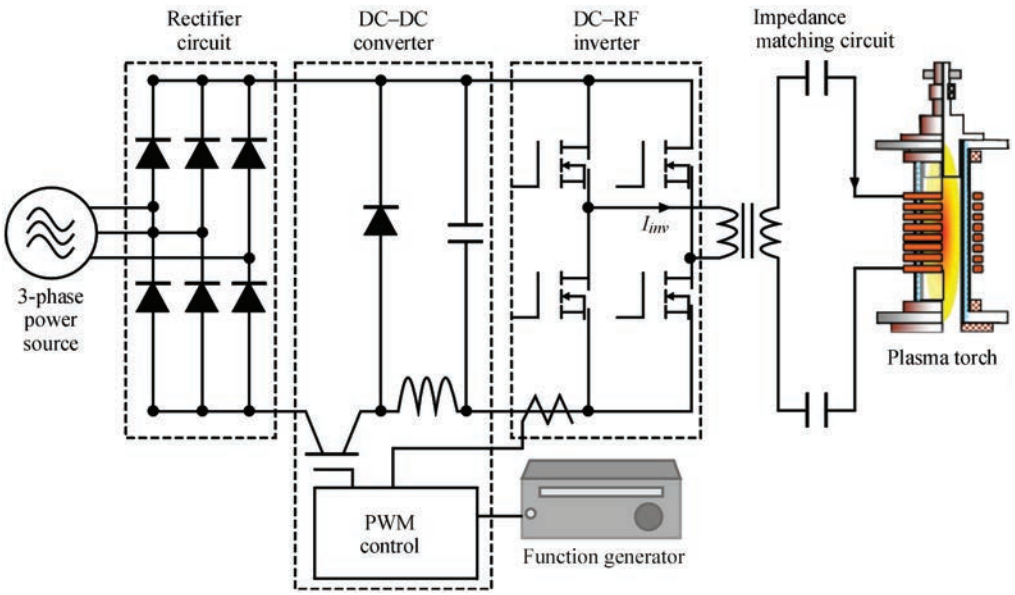

Figure 19. Scheme of a solid-state HFI generator for powering a plasmatron [74]

The power supply consists of four main parts: A rectifier circuit, an insulated gate, an IGBT bipolar transistor, a DC–DC chopper circuit, a full-bridge MOSFET inverter circuit, and an impedance matching circuit with a matching transformer and an LC series circuit. The MOSFET inverter frequency is adjusted within 350~450 kHz by phase-locked loop control to match the load impedance. This frequency of 350~450 kHz is much lower than that used in HFI plasma torches. In this case, the lower frequency electromagnetic field realizes a larger plasma skin depth, which helps maintain a large plasma volume. In addition, adopting this lower frequency allows the use of MOSFET energy at a low cost. It has been confirmed in experiments that this power supply's overall energy conversion efficiency is higher than 95 % for all cases. This higher energy conversion efficiency is an advantage of using semiconductors to support the high-power HFI plasma. The DC input power was recorded at 10 kW.

Modern powerful 13.56 MHz or 27.12 MHz, 120 kW, 50 Ω RF quartz-driven GENERATOR [75] on a generator tube still has low energy efficiency, significant dimensions, and cost. Therefore, transistor amplifiers are considered as a power supply for the next generation of HFI sources. Advantages compared to vacuum tube oscillators: higher efficiency (90 % and higher), lower cost, circuit simplifications with lower cooling requirements, and, due to proven reliability, plus excellent characteristics, make solid-state amplifiers a desirable option for the next generation of power supplies [76]. Although these are weighty arguments, a solid-state oscillator must be experimentally confirmed by practical experience in working with plasma devices. Solid-state oscillators have replaced vacuum tube oscillators in radio broadcasting for many years. The advantages of using such well-designed serial products for the power supply of plasma sources are potentially higher reliability and lower costs than vacuum tubes.

The increase in power is achieved by combining. The tested solid-state generator consists of 50 modules, each with a maximum power of 1.5 kW. Four transistors switch each module. The resulting square waves are arranged in parallel on a "summator" ferrite core and then converted into a sine wave by an output filter. Even if one or more modules fail, the generator will still be operational, albeit at a lower maximum output power. The module can be replaced quickly, which increases the reliability and maintainability of the system compared to self-excited vacuum tube generators. Unlike vacuum tube generators, there is no high voltage inside the solid-state generator, and therefore, no stored energy must be removed during a quick shutdown. The modular concept and the absence of high voltage are other reasons to expect high reliability.

To scale up plasma gasification, generators must have a maximum output power of up to 200 kW to provide sufficient power reserve. For inductively coupled plasma, most modern solid-state systems provide an efficiency of about 70–75 %, i.e., 70–75 % of the consumed power goes into the plasma.

An increase in power based on solid-state generators can also be achieved based on a newly developed tandem-type induction thermoplasma system using two HFI power sources and two inductor coils for one plasma torch (Figure 20) [77].

A 40 kW, 1 MHz solid-state RF ICP power supply has been developed and tested at the ITER-India Institute for Plasma Research [78]. The 40 kW supply was

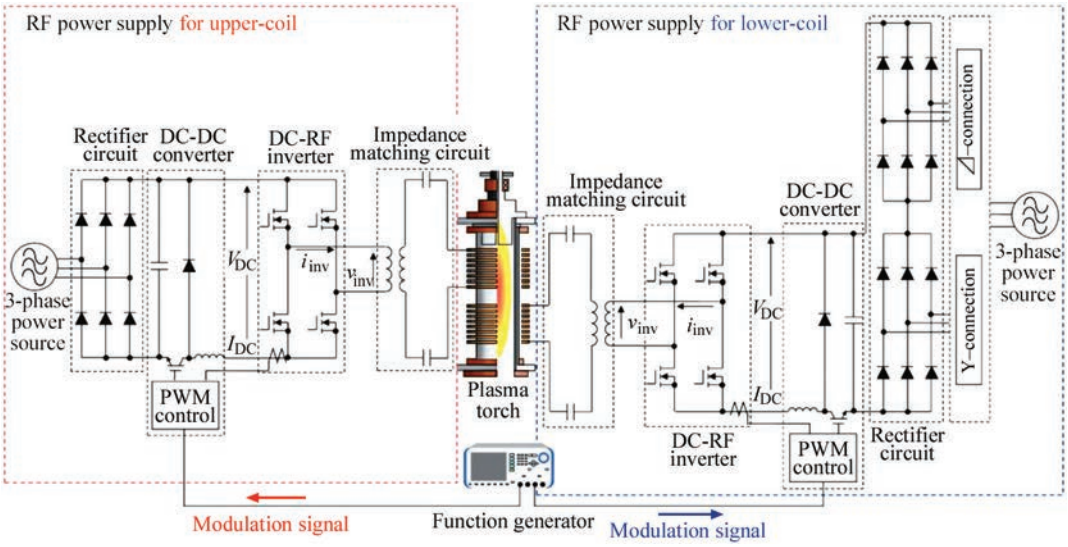

Figure 20. Tandem-type induction thermoplasma system

created by configuring multiple bridge inverter modules using latest generation switching semiconductors, magnetic combiners and LC network tuning to provide a 1 MHz sinusoidal output into a typical 50 Ω load (Figure 21). The experience with 40 kW HVHF provides significant insight into real-world scenarios in combination with RF-based plasma sources. This should form the basis for the next step, developing a 200 kW supply.

The problem of increasing the energy efficiency of induction plasma generators is quite solvable through energy-efficient conversion technology, the basis of which is the electronic component base of power electronics based on wide-bandgap semiconductors. The main semiconductor materials for power electronics are Si, GaAs, SiC, and GaN. All modern advances in high-power and ultra-high-power electronics are associated with silicon IGBTs. Is it possible to create IGBT devices based on GaAs, SiC, and GaN? [79]. When developing power electronic converters for plasma generators, they strive to achieve high efficiency and, at the same time, high power density. Increasing the switching frequency poses new challenges, since switching losses are proportional to the switching frequency, which limits the system's efficiency at high frequencies. At the same time, many standards put forward more stringent requirements for system efficiency. As for the operating frequency, most silicon-based designs today operate at 60–300 kHz. If the switching frequency is 500 kHz or higher, this can only be achieved with GaN. SiC is usually designed for 650–1200 V and higher operating voltages. Figure 22 shows a diagram of the dependence of power on frequency of various devices using them [80].

Silicon carbide is expected to grow in power electronics over the next five years to become the largest

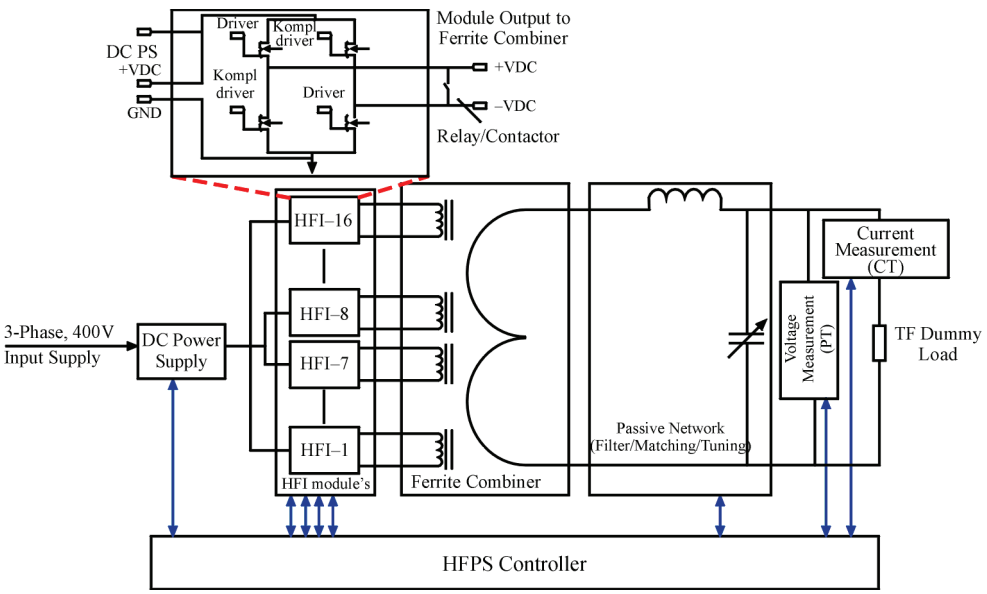

Figure 21. Schematic diagram of a 40 kW solid-state power supply for an induction plasma torch

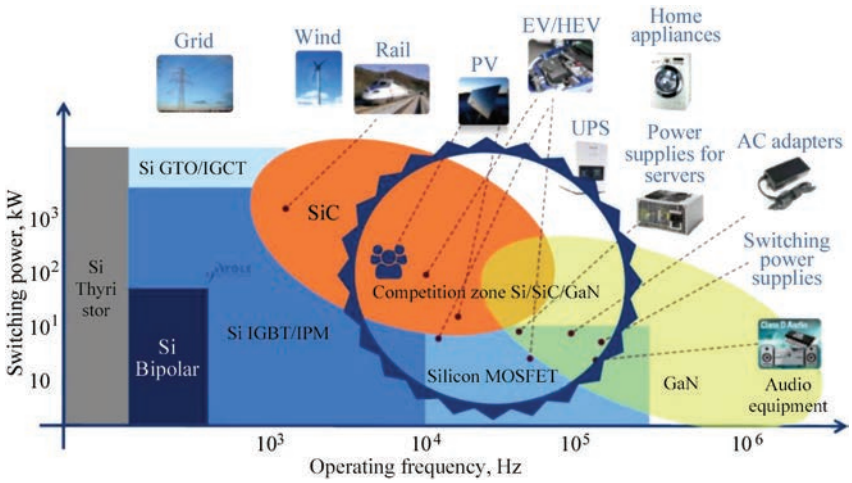

Figure 22. Diagram of the dependence of power on frequency and the area of application of power devices [80, 81]

broadband power market, followed by gallium nitride (in terms of power and FI demand). SiC enables higher voltage and power handling, while GaN enables higher frequency, which expands power applications to include HFI plasma generators.

The task is to transfer the latest research results to complex production quickly. Until now, the demand for power electronics for plasma engineering has mainly been associated with vacuum technology of thin films and etching. HRF plasma sources began to be studied in the late 1990s and eventually began to be widely used in the production of semiconductors [82, 83]. Solid-state devices of the Vacuum Power Plasma Supply (RF) 6 kW, 13.56 MHz are produced in serial production [84]. Further development of powerful RF plasma generators is possible in various directions, particularly as a space engine technology. Experimental results are presented for a powerful (up to 180 kW) inductive plasma generator with a high thermal efficiency of up to 84 % when exciting plasma in molecular gases [85].

Currently, solid-state power electronics technologies are rapidly evolving. New models represent innovative devices that utilize the good properties of wide band gap materials such as silicon carbide and gallium arsenide. Industrial and academic research interests are focused on developing proven and new power devices aimed at achieving good performance and increased energy savings, with an emphasis on the critical aspects and challenges that need to be addressed, in the authors' opinion, to fully realize the paradigm of better recycling of waste into useful products.

CONCLUSIONS

This paper presents positive arguments in favor of plasma gasification of biomass as a promising, viable and cost-effective technology. It is shown that the process is not limited to any specific feedstock and specific product, but is flexible in terms of processing biomass waste, which may be toxic or contaminated, into valuable products.

The effects of various plasma gasification parameters on the properties and yield of the syngas are analyzed to facilitate optimization of future research and the overall process. Plasma gasification can be an effective way to convert toxic and wet biomass into hydrogen-rich syngas, making the gasification process cleaner and operating at higher efficiency. Gasification, in general, has a number of negative social and environmental impacts, which can be minimized by appropriate plasma technology implementation.

As a result of many years of operation, plasma has been recognized as an effective method for destroying hazardous waste. However, plasma installations are expensive and use a lot of electricity. The article shows new technological solutions to these problems by optimizing energy flows in the gasification reactor, rational use of plasma as a concentrated energy flow, reducing electricity consumption by plasma burners, reducing the power and cost of plasma installations, and radically solving the problem of their reliability.

As can be seen from the study, plasma gasification of biomass has advantages over traditional options in obtaining hydrogen-enriched synthesis gas. As for the economic outlook, lower capital and operating costs are expected in the new approach to constructing large-scale production.

REFERENCES

1. Sikarwar, V.S., Zhao, M., Clough, P. et al. (2016) An overview of advances in biomass gasification. *Energy & Environmental Sci.*, 9(**10**), 2927–3304. DOI: https://doi.org/10.1039/c6ee00935b
2. *World Energy Outlook 2015*. https://iea.blob.core.windows.net/assets/5a314029-69c2-42a9-98ac-d1c5deeb59b3/WEO2015.pdf
3. Song, H., Yang, G., Xue, P. et al. (2022) Recent development of biomass gasification for H2 rich gas production. *Applications in Energy and Combustion Sci.*, **10**, 100059. DOI: https://doi.org/10.1016/j.jaecs.2022.100059

4. de Lasa, H., Salaices, E., Mazumder, J., Lucky, R. (2011) Catalytic steam gasification of biomass: Catalysts, thermodynamics and kinetics. *Chemical Reviews*, 111(**9**), 5404–5433. DOI: https://doi.org/10.1021/cr200024w
5. Nipattummakul, N., Ahmed, I.I., Gupta, A.K., Kerdsuwan, S. (2011) Hydrogen and syngas yield from residual branches of oil palm tree using steam gasification. *Inter. J. of Hydrogen Energy*, 36(**6**), 3835–3843. DOI: https://doi.org/10.1016/j.ijhydene.2010.04.102
6. Dincer, I. (2012) Green methods for hydrogen production. *Inter. J. of Hydrogen Energy*, 37(**2**), 1954–1971. DOI: https://doi.org/10.1016/j.ijhydene.2011.03.173
7. Franco, C., Pinto, F., Gulyurtlu, I., Cabrita, I. (2003) The study of reactions influencing the biomass steam gasification process. *Fuel*, 82(**7**), 835–842. DOI: https://doi.org/10.1016/S0016-2361(02)00313-7
8. Larsson, A., Kuba, M., Vilches, T.B. et al. (2021) Steam gasification of biomass – Typical gas quality and operational strategies derived from industrial-scale plants. *Fuel Proc. Technol.*, **212**, 106609. DOI: https://doi.org/10.1016/j.fuproc.2020.106609
9. Khan, M.J., Al-Attab, K.A. (2022) Steam gasification of biomass for hydrogen production – A review and outlook. *J. of Advanced Research in Fluid Mechanics and Thermal Sci.*, 98(**2**), 175–204. DOI: https://doi.org/10.37934/arfmts.98.2.175204
10. Henriksen, U., Ahrenfeldt, J., Jensen, T.K. et al. (2006) The design, construction and operation of a 75 kW two-stage gasifier. *Energy*, 31(**10–11**), 1542–1553. DOI: https://doi.org/10.1016/j.energy.2005.05.031
11. Trippe, F., Fröhling, M., Schultmann, F. et al. (2011) Techno-economic assessment of gasification as a process step within biomass-to-liquid (BtL) fuel and chemicals production. *Fuel Proc. Technol.*, 92(**11**), 2169–2184. DOI: https://doi.org/10.1016/j.fuproc.2011.06.026
12. Hasler, P., Nussbaumer, Th. (1999) Gas cleaning for IC engine applications from fixed bed biomass gasification. *Biomass and Bioenergy*, 16(**6**), 385–395. DOI: https://doi.org/10.1016/S0961-9534(99)00018-5
13. Asadullah, M. (2014) Barriers of commercial power generation using biomass gasification gas: A review. *Renewable and Sustainable Energy Rev.*, **29**, 201–215. DOI: https://doi.org/10.1016/j.rser.2013.08.074
14. Petrov, S.V., Katircioğlu, T.Y. (2020) *Technological aspects of steam and water plasma*. OmniSkriptum Publishing Group.
15. Zhang, Q., Dor, L., Fenigshtein, D. et al. (2011) Gasification of municipal solid waste in the plasma gasification melting process. *Applied Energy*, 90(**1**), 106–112. DOI: https://doi.org/10.1016/j.apenergy.2011.01.041
16. Sanjaya, E., Abbas, A. (2023) Plasma gasification as an alternative energy-from-waste (EFW) technology for the circular economy: An environmental review. *Resources, Conservation and Recycling*, **189**, 106730. DOI: https://doi.org/10.1016/j.resconrec.2022.106730
17. (2008) Independent waste technology report. The alter NRG/WESTINGHOUSE plasma gasification process. http://energy.cleartheair.org.hk/wp-content/uploads/2013/09/Westinghouse_Plasma_Gasification.pdf
18. Hrabovsky, M. (2011) Thermal plasma gasification of biomass. In: *Progress in Biomass and Bioenergy Production*. DOI: https://doi.org/10.5772/18234
19. Lopez, G., Artetxe, M., Amutio, M. et al. (2018) Recent advances in the gasification of waste plastics. A critical overview. *Renewable and Sustainable Energy Rev.*, 82(**1**), 576–596. DOI: https://doi.org/10.1016/j.rser.2017.09.032
20. Hlina, M., Hrabovsky, M., Kavka, Konrad T.M. (2014) Production of high quality syngas from argon/water plasma gasification of biomass and waste. *Waste Management*, 34(**1**), 63–66. DOI: https://doi.org/10.1016/j.wasman.2013.09.018
21. Tamošiūnas, A., Valatkevičius, P., Valinčius, V., Levinskas, R. (2016) Biomass conversion to hydrogen-rich synthesis fuels using water steam plasma. Comptes Rendus. Chimie. *Inter. Renewable Energy Congress*, 19(**4**), 433-440. DOI: 10.1016/j.crci.2015.12.002
22. Zhovtyanskij, V., Ostapchuk, M. (2022) Plasma technologies in the problem of producing "more than green hydrogen". *Gorenie i Plazmohimiya*, 20(**1**), 11–32. DOI: https://doi.org/10.18321/cpc478
23. Obiora, N.K., Ujah, C.O., Asadu, C.O. et al. (2024) Production of hydrogen energy from biomass: Prospects and challenges. *Green Technol. and Sustainability*, 2(**3**), 100100 DOI: https://doi.org/10.1016/j.grets.2024.100100
24. Nagar, V., Kaushal, R. (2024) A review of recent advancement in plasma gasification: A promising solution for waste management and energy production. *Inter. J. of Hydrogen Energy*, 77(**5**), 405–419. DOI: https://doi.org/10.1016/j.ijhydene.2024.06.180
25. (2015) "World's largest" gasification plant nears completion. Ed. by T. Goulding. https://www.letsrecycle.com/news/worlds-largest-gasification-plant-nears-completion/
26. *Development of a commercial reactor for high-temperature plasma gasification of waste*. https://www.inews24.com/view/1469770
27. Borges, P.T., Lora, E.E.S., Venturini, O.J. et al. (2024) A comprehensive technical, environmental, economic, and biometric assessment of hydrogen production through biomass gasification, including global and brazilian potentials. *Sustainability*, 16(**21**), 9213. DOI: https://doi.org/10.3390/su16219213
28. DNV Report: *Hydrogen Forecast to 2050*. https://aben.com.br/wp-content/uploads/2022/06/DNV_Hydrogen_Report_2022_Highres_single1.pdf
29. Ball, M., Wietschel, M. (2009) The future of hydrogen-opportunities and challenges. *Inter. J. of Hydrogen Energy*, **34**, 615–627. DOI: https://doi.org/10.1016/j.ijhydene.2008.11.014
30. Arregi, A., Amutio, M., Lopez, G. et al. (2018) Evaluation of thermochemical routes for hydrogen production from biomass: A review. *Energy Conversion and Management,* **165**, 696–719. DOI: https://doi.org/10.1016/j.enconman.2018.03.089
31. *Oregon. Biomass energy*. http://www.oregon.gov/ENERGfi/RENEW/Biomass/
32. Demirbas, A. (2005) Potential applications of renewable energy sources, biomass combustion problems in boiler power systems and combustion related environmental issues. *Progress in Energy and Combustion Sci*., 31(**2**), 171–192. DOI: https://doi.org/10.1016/j.pecs.2005.02.002
33. (2015) *IEA. Technology roadmap — hydrogen and fuel cells*. https://www.iea.org/reports/technology-roadmap-hydrogen-and-fuel-cells
34. *Phyllis — database for biomass and waste*. https://www.fao.org/4/y0909e/y0909e09.htm
35. Jia, G. (2021) Combustion characteristics and kinetic analysis of biomass pellet fuel using thermogravimetric analysis. *Processes*, 9(**5**), 868. DOI: https://doi.org/10.3390/pr9050868
36. Mason, P.E., Darvell, L.I., Jones, J.M. et al. (2015) Single particle flame-combustion studies on solid biomass fuels. *Fuel*, **151**, 21–30. DOI: https://doi.org/10.1016/j.fuel.2014.11.088
37. Bryers, R.W. (1996) Fireside slagging, fouling, and high temperature corrosion of heat-transfer surface due to impurities in steam-raising fuels. *Progress in Energy and Combustion*

Sci., 22, (**1**), 29–120. DOI: https://doi.org/10.1016/0360-1285(95)00012-7
38. Mason, P.E., Riaza, J., Chalmers, H. et al. (2016) Biomass fuel flexibility in future conventional power generation. In: *Proc. of 5th IET Inter. Conf. on Renewable Power Generation 2016*. DOI: https://doi.org/10.1049/cp.2016.0559
39. Petrov, S., Stukhlyak, P., Bondarenko, S. et al. (2024) Steam plasma gasification of biomass using electrodeless plasmatrons. *The Paton Welding J.*, **6**, 20–28. DOI: https://doi.org/10.37434/tpwj2024.06
40. Sidek, F.N., Abdul Samad, N.A.F, Saleh, S. (2020) Review on effects of gasifying agents, temperature and equivalence ratio in biomass gasification process. In: *Proc. of IOP Conf. Series: Materials Science and Engineering, Kuantan, 1–2 October 2019*, 012028. DOI: https://doi.org/10.1088/1757-899X/863/1/012028
41. Jaworski, Z., Zakrzewska, B., Pianko-Oprych, P. (2017) On thermodynamic equilibrium of carbon deposition from gaseous C–H–O mixtures: Updating for nanotubes. *Rev. in Chemical Eng.*, 33(**3**), 217–235. DOI: https://doi.org/doi:10.1515/revce-2016-0022
42. Liu, K., Song, C., Subramani, V. (2010) Hydrogen and syngas production and purification technologies. *Wiley, Hoboken, New Jersey*, **533**. DOI: https://doi.org/10.1002/9780470561256
43. Kagakin, E.I., Bogomolov, A.R., Shevyrev, S.A., Pribaturin, N.A. (2013) Interaction of carbonized coal with superheated water vapor. *Polzunovskij Vestnik*, **1**, 135–138.
44. Balat, M. (2008) Hydrogen-rich gas production from biomass via pyrolysis and gasification processes and effects of catalyst on hydrogen yield. *Energy Sources, Pt. A: Recovery, Utilization and Environmental Effects*, **30**, 552–554. DOI: https://doi.org/10.1080/15567030600817191
45. (2006) *Plasma progress: Low-cost operation and clean energy at long last*? https://waste-management-world.com/artikel/plasma-progress-low-cost-operation-and-clean-energy-at-long-last
46. Zitouni, A., Voutsas, E. (2021) Modeling, optimization and cost analysis of municipal solid waste treatment with plasma gasification. *Environmental Proc.*, **8**, 747–767. DOI: https://doi.org/10.1007/s40710-021-00518-y
47. Mayoko, J.C., Lee, B., Nyazabe, S. et al. (2023) Plasma gasification, an eco-friendly solution for power generation and MSW treatment in Kinshasa, DR Congo. *Open Access Library J.*, 10(**12**). DOI: https://doi.org/10.4236/oalib.1110424
48. Lourinho, G., Alves, O., Garcia, B. et al. (2023) Costs of gasification technologies for energy and fuel production: Overview, analysis, and numerical estimation. *Recycling*, 8(**3**), 49. DOI: https://doi.org/10.3390/ recycling8030049
49. Panicker, P.K., Magid, A. (2016) Microwave plasma gasification for the restoration of urban rivers and lakes, and the elimination of oceanic garbage patches. In: *Proc. of 10th Inter. Conf. on Energy Sustainability Collocated with the ASME 2016 Power Conf. and the ASME 2016 14th Inter. Conf. on Fuel Cell Science, Engineering and Technology, June 26–30, 2016, Charlotte, North Carolina*, *USA*. ES2016-59632, V001T02A011; 14. DOI: https://doi.org/10.1115/ES2016-59632
50. *Industrial microwave generators for next generation waste gasification*. https://rfhic.com/case-studies/industrial-microwave-generators-for-waste-gasification-applications/
51. Petrov, S.V., Zhovtyansky, V.A. (2019) *Energy efficient steam-plasma technologies for waste processing*. Kyiv, Naukova Dumka [in Russian].
52. Gabbar, H.A., Darda, S.A., Damideh, V. et al. (2021) Comparative study of atmospheric pressure DC, RF, and microwave thermal plasma torches for waste to energy applications. *Sustainable Energy Technologies and Assessments*, **47**, 101447. DOI: https://doi.org/10.1016/j.seta.2021.101447
53. *Applied plasma technologies. More products: Plasma torches*. https://www.plasmacombustion.com/product-torches.html
54. Leblanc, D., Dolbec, R., Guerfi, A. et al. (2017) Silicon nanopowder synthesis by inductively coupled plasma as anode for high-energy Li-ion batteries: Arrays, functional materials, and industrial nanosilicon: In: *Silicon Nanomaterials Sourcebook*, 463–484. DOI: https://doi.org/10.1201/9781315153551-24
55. *JEOL. TP series. RF induction thermal plasma. Products*. https://www.jeol.com/products/industrial/eb/TPseries.php
56. Mirek, P. (2019) *Novel industrial scale radio frequency inductively coupled plasma torch. Master of applied science*. Department of Mechanical and Industrial Engineering, University of Toronto. https://utoronto.scholaris.ca/server/api/core/bitstreams/b3fe4d3a-233b-421f-a5f3-8c36491dec3a/content
57. Strelko, O., Berdnychenko, Y., Pylypchuk, O. et al. (2021) Historical milestones in the development and creation of radio frequency inductively coupled plasma torches. In: *Proc. of Inter. 3rd Ukraine Conf. on Electrical and Computer Engineering, 26-28 August 2021*. DOI: https://doi.org/10.1109/UKRCON53503.2021.9575482
58. Bottin, B., Chazot, O., Carbonaro, M. et al. (2000) The VKI plasmatron characteristics and performance. *72 Chaussee de Waterloo B-1640 Rhode-Saint-Genese, Belgium*. https://apps.dtic.mil/sti/pdfs/ADP010745.pdf
59. Merkhouf, A., Boulos, M.I. (1998) Integrated model for the radio frequency induction plasma torch and power supply system. *Plasma Sources Sci. and Technology*, 7(**4**), 599. DOI: https://doi.org/10.1088/0963-0252/7/4/017
60. Reed, T.B. (1961) Induction-coupled plasma torch. *J. of Applied Physics*, 32(**5**), 821–824. DOI: http://dx.doi.org/10.1063/1.1736112
61. Alavi, S., Khayamian, T., Mostaghimi, J. (2017) Conical torch: The next-generation inductively coupled plasma source for spectrochemical analysis. *Analytical Chemistry*, 90(**5**), 3036–3044. DOI: http://dx.doi.org/10.1021/acs.analchem.7b04356
62. Boulos, M.I., Fauchais, P., Pfender, E. (2016) Inductively coupled radio frequency plasma torches*: Handbook of Thermal Plasmas.* Springer, Cham. DOI: https://doi.org/10.1007/978-3-319-12183-3_17-1
63. Chung, P.M., Liu, S.W., Mirels, H. (1963) Effect of discontinuity of surface catalycity on boundary layer flow of dissociated gas. *Inter. J. of Heat and Mass Transfer*, 6(**3**), 193–210. DOI: https://doi.org/10.1016/0017-9310(63)90106-6
64. Chazot, O., Panerai, F., Muylaert, J.M., Thoemel, J. (2010) Catalysis phenomena determination in plasmatron facility for flight experiment design (Invited). In: *Proc. of 48th Aerospace Sciences Meeting Including the New Horizons Forum and Aerospace Exposition, 04–07 January, 2010 Orlando, Florida*. DOI: https://doi.org/10.2514/6.2010-1248
65. Danilenko, A.A. (2012) *Experimental and theoretical studies of plasma gasification processes of carbon-containing technogenic waste*: In: Syn. of Thesis for Cand. of Tech. Sci. Degree. Novosibirsk, 21.
66. Messerle, V.E., Ustimenko, A.B., Lavrichshev, O.A., Nugman, M.K. (2024) The gasification and pyrolysis of biomass using a plasma system. *Energies*, 17(**22**), 5594. DOI: https://doi.org/10.3390/en17225594
67. Aikas, M., Gimžauskaitė, D., Tamošiūnas, A. et al. (2024) Thermal arc air plasma application for biomass (wood pellets) gasification. *Clean Technol. and Environmental Policy*, 26(**1**), 31–43. DOI: https://doi.org/10.1007/s10098-023-02566-4
68. Tamayo-Pacheco, J.J., Peña-Pupo, L., Vázquez-Peña, A., Brito-Sauvanell, Á.L. (2020) Hydrogen-rich syngas pro-

duction by plasma gasification of existing biomasses in Cuba. *Revista Ciencias Técnicas Agropecuarias*, 29(**4**), 53–63. https://go.gale.com/ps/i.do?p=IFME&u=anon~f-3c66468&id=GALE%7CA652867273&v=2.1&it=r&-sid=googleScholar&asid=628dc909
69. *ISC3*. International Sustainable Chemistry Collaborative Centre. https://www.isc3.org › page › best-practice-detail › plasma-gasification
70. Yao, S., Zhang, Y., Xia, J. et al. (2023) Cascade utilization of energy in high temperature syngas to reduce energy consumption in biomass gasification processes. *Case Studies in Thermal Engineering*, **52**, 103680. DOI: https://doi.org/10.1016/j.csite.2023.103680
71. Paskalov, G. (2015) RF PLASMA: From R&D to commercial applications. In: *Proc. of 22nd Inter. Symp. on Plasma Chemistry, July 5–10, 2015, Antwerp, Belgium*. https://www.ispc-conference.org/ispcproc/ispc22/O-23-2.pdf
72. Fazekas, P., Czégény, Z., Mink, J. et al. (2016) Decomposition of poly (vinyl chloride) in inductively coupled radiofrequency thermal plasma. *Chemical Eng. J.*, 302(**15**), 163–171. DOI: https://doi.org/10.1016/j.cej.2016.05.044
73. Merkhouf, A., Boulos, M.I. (2000) Distributed energy analysis for an integrated radio frequency induction plasma system. *J. of Physics D: Applied Physics*, 33(**13**), 1581–1587. DOI: https://doi.org/0022-3727/33/13/304
74. Tanaka, Y. (2021) Recent development of new inductively coupled thermal plasmas for materials processing. *Advances in Physics: X*, 6(**1**): 1867637. DOI: https://doi.org/10.1080/23746149.2020.1867637
75. *Sairem. Microwave and radio frequency*. https://www.sairem.com/
76. Kraus, W., Fantz, U., Heinemann, B., Franzen, P. (2015) Solid state generator for powerful radio frequency ion sources in neutral beam injection systems. *Fusion Eng. and Design*, **91**, 16–20. DOI: https://doi.org/10.1016/j.fusengdes.2014.11.015
77. Kuraishi, K., Akao, M., Tanaka, Y. et al. (2016) Temperature behavior in a tandem type of modulated induction thermal plasma for materials processing. *J. of Physics Conf. Series*, 441(**1**). https://doi.org/10.1088/1742-6596/441/1/012016
78. Gajjar, S., Upadhyay, D., Singh, N. et al. (2021) Experimental results of 40 kW, 1 MHz solid state high frequency power supply with inductively coupled plasma. In: *Proc. of AIP Conf.*, 2373, 100002. DOI: https://doi.org/10.1063/5.0057477
79. Vojtovich, V., Gordeev, A., Dumanevich, A. (2010) Si, GaAs, SiC, GaN — power electronics. Comparison, new possibilities. *Silovaya Elektronika*, 5, **4**–10.
80. *Semiconductor today*. https://www.semiconductor-today.com/features.shtml
81. https://www.eetrend.com/content/2021/100555218.html Debuted at CICD 2021 to empower the third-generation semiconductor industry with advanced ALD technology
82. *Proc. of 9th Inter. Conf. on Power Electronics for Plasma Eng. May 14–17, 2018, Freiburg, Germany*. https://publica.fraunhofer.de/entities/mainwork/477cb287-1b40-424d-9d5c-ac4572604026
83. Okumura, T. (2010) Inductively coupled plasma sources and applications. *Physics Research Inter.*, **1**. DOI: https://doi.org/10.1155/2010/164249
84. *PSTEK*. https://pstek.co.kr/wp-content/uploads/2019/12/PSTEK_Plasma-Power-Supplies.pdf
85. Georg, R., Chadwick, A.R., Dally, B.B., Herdrich, G. (2021) Power efficiency estimation of an inductive plasma generator using propellant mixtures of oxygen, carbon-dioxide and argon. *Acta Astronautica*, **179**, 536–545. DOI: https://doi.org/10.1016/j.actaastro.2020.11.020

ORCID
S.V. Petrov: 0000-0003-0373-8003,
O.I. Som: 0009-0009-4152-4832,
S.G. Bondarenko: 0000-0003-2305-6691,
O.V. Sanginova: 0000-0001-6378-7718,
M. Ganczarski: 0009-0009-0355-0677,
E. Rój: 0000-0002-8691-3315

CONFLICT OF INTEREST
The Authors declare no conflict of interest

CORRESPONDING AUTHOR
S.V. Petrov
The Gas Institute of the NASU
39 Degtyarivska Str., 03113, Kyiv, Ukraine
E-mail: vizana.sp@gmail.com

SUGGESTED CITATION
S.V. Petrov, O.I. Som, S.G. Bondarenko, O.V. Sanginova, M. Ganczarski, E. Rój (2025) Implementation and sustainability of biomass gasification using plasma technologies. *The Paton Welding J.*, **5**, 10–29. DOI: https://doi.org/10.37434/tpwj2025.05.02

JOURNAL HOME PAGE
https://patonpublishinghouse.com/eng/journals/tpwj

Received: 25.03.2025
Received in revised form: 29.04.2025
Accepted: 23.06.2025

DOI: https://doi.org/10.37434/tpwj2025.05.03

SYNTHESIS AND STUDY OF A PHARMACEUTICAL COMPOSITION WITH SILVER NANOPARTICLES, PRODUCED BY ELECTRON BEAM EVAPORATION

G.G. Didikin

E.O. Paton Electric Welding Institute of the NASU
11 Kazymyr Malevych Str., 03150, Kyiv, Ukraine

ABSTRACT

A technological scheme for generating and forming a directed atomic and molecular flow of silver in the process of electron beam evaporation and condensation for the synthesis of nanocomposites is considered. The influence of the initial mass of silver, beam current, evaporation time, and evaporation rate on the mass of evaporated silver was evaluated. The distribution of the average size of silver nanoparticles depending on the evaporated silver velocity was estimated. The obtained results make it possible to synthesize nanocomposites with a predetermined most probable average size of silver nanoparticles. The structure of the PVP–Ag composite and of the H_2O–PVP–Ag and Ethanol–PVP–Ag colloidal systems was investigated by TEM and photon correlation spectroscopy (PCS). The results of the study of glucosamine substance with PVP and nanosilver in the form of a gel with antimicrobial (antistaphylococcal, antipseudomonal), wound healing and antiinflammatory effects, which has low toxicity and can be used for the local treatment of infected wounds and purulent inflammatory skin lesions, are presented.

KEYWORDS: composite powders, nanostructured coatings, electron beam evaporation and condensation (EB–PVD), evaporator design, directed vapor flow in vacuum, deposition, colloidal systems, polyvinylpyrrolidone, photon correlation spectroscopy

INTRODUCTION

With active development of nanotechnology research on creation of new nanomaterials and their application as active pharmaceutical ingredients in medicines is growing [1]. Of great interest in this area are nanoparticles (NP) of metals, having antimicrobial properties. This is due to the fact that at present the issue of combating the increasing resistance of microorganisms to chemotherapeutic antimicrobial drugs is extremely acute in medicine [2, 3].

Introduction into medical practice of antibiotics of various origin, chemical structure, spectrum of antimicrobial activity, and mechanism of action promoted improvement of the effectiveness of treatment of many infectious diseases, and at the same time posed new, difficult-to-solve problems for theoretical and clinical medicine, which concern the correct choice of the necessary drug and prevention of side effects. Development of the acquired microorganism resistance is one of the complex issues of modern antibiotic therapy. Antimicrobial agents of new chemical groups are introduced, and combination drugs are used in order to overcome this complication. However, microorganism resistance is growing many times faster than the new antimicrobial agents are created. Against the background of a significant increase in the acquired bacterial resistance a very limited number of new antibacterial drugs have been introduced into the clinical practice in recent years.

Numerous literature data of the last years are indicative of the effectiveness of the action of metal nanoparticles, in particular, silver, against a wide range of aerobic, anaerobic, gram-positive and gram-negative bacteria, yeast fungi, filamentous fungi and viruses, absence of resistance to them on the part of microorganisms and the relevance of using silver nanoparticles as an antimicrobial agent for treatment of infectious diseases [1, 5–8].

Silver has been approved for use as an antimicrobial agent for the first time in the 20s of the previous century, but its usage has decreased with the beginning of application of antibiotics for treatment of bacterial infections since the 40s of the previous century. Recently, silver has become popular again, particularly in treatment of open wounds with the spreading of methicillin-resistant Staphylococcus aureus [6]. Silver is regarded as an element, required for normal functioning of internal organs and systems, as well as a powerful remedy that improves immunity.

Increasing use of silver for local treatment leads to increased problems associated with studying its antimicrobial action [6]. Since the time, when it was first established that the destruction of pathogenic microorganisms ceases, when penicillin concentration in the plasma drops below the minimal inhibitory concentration (MIC), determination of the pharma-

cological index became the main parameter during comparison of antimicrobial agents and development of optimal dosing regimens. Silver MIC is actively studied in various areas of its application [6]. MIC_{50} and MIC_{90} values, most often studied during evaluation of microorganism sensitivity to antibiotics, are not adapted to studying the action of silver-containing agents. According to literature data, silver MIC relative to *St*. *aureus* (close to 100 strains) is in the range from 8 to 80 mg/l, relative to Ps. Aeruginosa (close to 100 strains) it is in the range of 8–70 mg/l [6].

To summarize the above-said, there is no doubt that development of new medicines based on silver NPs, is a relevant and in-demand area of research.

The objective of the work was studying the possibility and evaluation of the prospects for application of the process of vacuum electron beam evaporation to produce silver nanoparticles; investigation of the dependence of the evaporated silver weight on the initial weight of the silver sample, current of the beam heating the reactor for oriented deposition of the vapor flow on the powder, evaporation rate and duration of the process of silver evaporation to produce silver nanoparticles on the surface of a powderlike carrier; providing recommendations on practical application of the technological parameters of silver evaporation for assessment of the preset average size of silver NPs; using the technology of silver deposition on the surface of a powderlike carrier, synthesizing a nanomaterial of PVP–Ag composition; using the produced material of PVP–Ag composition to develop a new medicine with bactericidal action.

INVESTIGATION MATERIALS AND PROCEDURES

At present, local antiseptic agents, in particular, silver preparations, are used to treat purulent wounds. Dermasin, Sulfargin, Argedin Bosnaliek creams contain 1 % of silver sulfadiazine, Argosulfan cream contains 2 % of sulfatiazole [9]. A disadvantage of these drugs is the fact the silver is in an ionized shape in their composition, which increases the toxicity risk. For instance, at topical application of silver sulfadiazine agents (Dermasin, Argosulfan, Sulfargin) up to 1 % of silver ions and up to 10 % of sulfadiazine can penetrate into the systemic blood circulation from the damaged surface. Thus, long-term application of these preparations can result in side effects, characteristic for sulfanilamides: allergic reactions, circulatory problems, digestive disorders, hepatite, etc.

A task was set to expand the range of drugs for the treatment of purulent wounds and purulent-inflammatory lesions through development of an original pharmaceutical composition in gel form, which contains a combination of active and additional substances, exhibits a wide spectrum of antimicrobial activity and at the same time has antiinflammatory, reparative and detoxication properties. The posed task is solved so that the pharmaceutical composition in the gel form for treatment of purulent wounds and purulent-inflammatory lesions contains silver nanoparticles as the active substance, produced by electron beam vacuum evaporation and condensation of silver on the carrier material — polyvinylpyrrolidone (PVP) and glucosamine and has carbopol, glycerin and water in the composition of the hydrophilic gel base. Addition of glucosamine allows expanding the spectrum of pharmacological action of the drug and revealing the antiinflammatory and reparative activity. It inhibits the formation of peroxide radicals and the activation of proteolytic enzymes in the area of inflammation, which damage the tissue, reduces the manifestations of inflammation, inhibits the formation of antiinflammatory cytokines, and exerts an endothelium-protective effect. Glucosamine also has analgesic effect. PVP promotes adsorption and removal of toxins from the wound. The gel hydrophilic base does not dry out or irritate the skin. Active components and drug base components are approved for use in the pharmaceutical industry. Introduction of the nanotechnologies allows reducing the toxicity of silver preparations. It is known that PVP stabilized silver nanoparticles, unlike the ionized species, do not exhibit any toxic properties in the human body and have unique physicochemical and biological properties, which ensure their high antibacterial, antifungal and antiviral activity, and additionally demonstrate antioxidant properties, stimulate the healing processes in the skin, and increase local immunity. Therefore, the problem of searching for and development of new preparations with silver nanoparticles for treatment of wounds is relevant for modern pharmaceutical medicine.

Polymers of PVP–Ag system were synthesized using Plasdon® (PVP) K-15 and Plasdon® K-17 polymers with the molecular weight 8000 and 10000 from the series of synthetic homopolymers, which have surfactant properties, are highly soluble in water, alcohol (ethanol) [10] and a number of organic solvents.

Works [11–13] highlight the technological capabilities for realization of the process of oriented deposition of the vapour flow on the powder surface. This method allows dosing the amount of silver in its vapour flow and ensuring deposition of the required amount on the carrier particle surface to produce a composite of the specified composition and structure. Surfactants (SA) in the powderlike form were predominantly used, when the material dispersion and its mixing can ensure a uniform distribution of silver

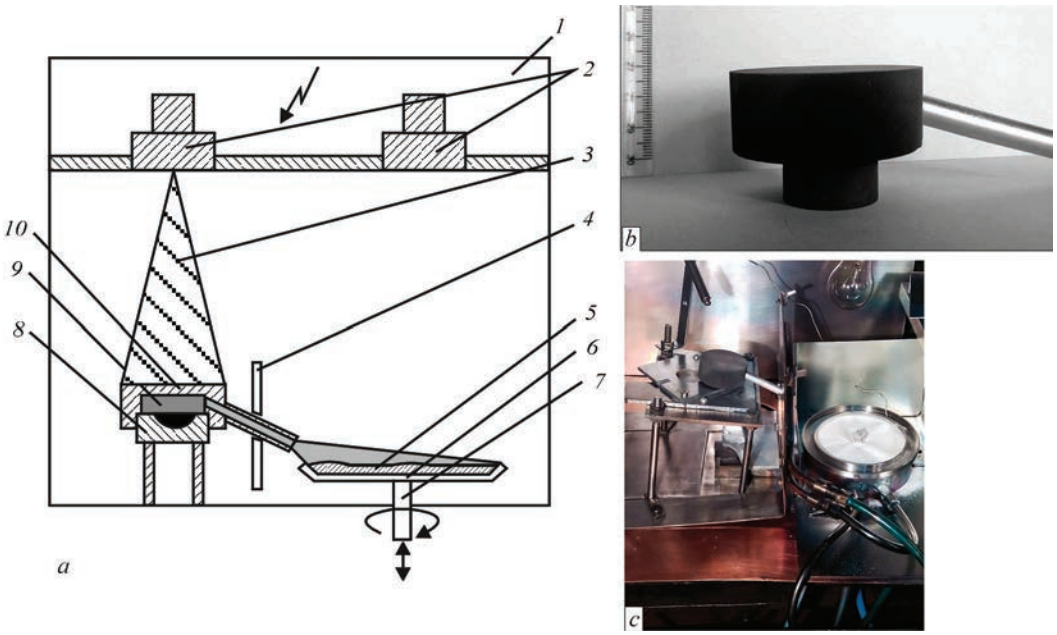

Figure 1. Scheme (*a*), and appearance of the evaporator (reactor) (*b*) for oriented deposition of the vapour flow on the powder and general view inside the process chamber of EBU UE-142 with the reactor and container with powder for silver deposition (*c*): *1* — vacuum chamber; *2* — electron beam gun; *3* — electron beam; *4* — water-cooled screen; *5* — powder; *6* — powder container; *7* — device for rotation and vibration of the powder container; *8* — lower part of evaporator (reactor); *9* — evaporation material; *10* — upper part of the evaporator with a hole and nozzle for directed vapour flow outlet [12]

particles on the carrier granule surface. Selection of a carrier from such SA, which are capable of stabilizing silver particles in the dispersed medium of a colloidal solution, allows obtaining a colloidal solution by dissolution of the nanocomposite directly in the dispersed medium without preliminary releasing of the silver nanoparticles from the nanocomposite by the carrier dissolution in the intermediate fluid. Such carriers can be SA soluble in water and/or other liquids, selected from a group which includes: polyvinylpyrrolidone, polyethylene oxide, polyacrylamide, dextran, and starch. PVP was used as the carrier material.

Figure 1, *a* shows the technological scheme of the process of vacuum electron beam evaporation and condensation of Ag molecular beams, in order to produce Ag nanoparticles, and the general view from the inside of the process chamber of an electron beam unit (*c*) with application of a reactor (*b*) which is used for generation and formation of a directed atomic-molecular Ag flow. Synthesis of nanocomposites from silver NPs was performed in UE-142 unit. In the presented variant of the technological scheme the graphite evaporator consists of the upper and lower parts, forming a closed volume. The evaporation material is located in the evaporator lower part, its upper part has an opening for the molybdenum tip. During heating of the evaporator by the electron beam, the material (silver), which is in its lower part, is brought to melting, evaporated and a molecular silver flow directed to the container with the powder is formed by the tip. At contact of the silver vapours with the carrier powder silver condensation occurs on the surface of its granules and a nanocomposite with Ag NPs is formed.

In the conducted experiments the powders were placed into flat copper cooled containers, and stirred with simultaneous deposition of the vapour flow. Produced Ag–PVP nanocomposites were used to prepare colloidal systems (CS) based on water and ethyl alcohol. Particle distribution by size in PVP–Ag–H_2O CS was determined by the method of photon-correlation spectroscopy (PCS) in the laser correlation spectrometer Zeta Sizer-3 (Malvern, Great Britain). A feature of the PCS method consists in that the results of separate measurement can be calculated both as monomodal, and as a polymodal approximation (in our case, using the Contin program). The monomodal approximation allows obtaining the average size of all the particles present in the solution, while the polymodal approximation shows the average size and quantity of each type of particles in the case of a polydisperse suspension. The method of transmission electron microscopy (TEM) was used to study in the transmission mode in HITACHI H-800 microscope at 150 kV accelerating voltage the precipitates obtained after removal of PVP and water from PVP–Ag–H_2O colloid. Mathematical processing of the obtained results was performed using Microsoft Excel statistical analysis programs.

Water, other polar, as well as nonpolar fluids: aliphatic and aromatic carbohydrates, their derivatives, etc., can be used to produce colloidal solutions. PVP application as the silver particle carrier, in which the

silver particles are fixed, allows producing by a simple and effective method the silver nanocomposite, which already contains a stabilizer, preventing silver particle aggregation during dissolution directly in the disperse medium of a target colloidal solution or in another intermediate liquid. This way, the process simplification is achieved both at the stage of silver nanoparticle synthesis, and at the stage of preparation of the colloidal solutions with provision of their aggregative resistance.

Colloidal solutions based on PVP with water are traditionally used in medicine as plasma substitutes. In order to prepare a CS of silver in water, a sample of powder of PVP–Ag nanocomposite (PVP of K-17 grade) is placed into a clean dry glass, 20 ml of deionized distilled water are added, the glass is capped, and placed into a water bath with 50–60 °C temperature to accelerate dissolution. After a ten minute soaking with mixing and ultrasonic treatment, a transparent colloidal solution of silver of a light-brown colour is produced.

PVP readily dissolves in ethyl alcohol. Therefore, CS of Ethanol-2 % PVP–Ag composition were also prepared, in order to determine the size of the nanoparticles in PVP–Ag compositions produced in the technological modes. CS were prepared in 20 ml test tubes as follows: sample of PVP-Ag powder was poured into the tube, 15 ml of ethyl alcohol was added, and the tube was capped. Stirring the tube contents, we tried to produce a transparent colloidal solution of silver of a light-brown colour. After that, the tubes (without the cap) with their contents were placed into an ultrasonic bath, heated up to 55 °C, and subjected to US treatment in "SWEEP" mode for 30 min. Twenty hours after preparation particle distribution was measured by PCS method.

The produced samples were studied at O.V. Palladin Institute of Biochemistry of the NAS of Ukraine. Investigations of antimicrobial activity of medicinal forms with silver nanoparticles were conducted at the National University of Pharmacy (NUPh, Kharkiv).

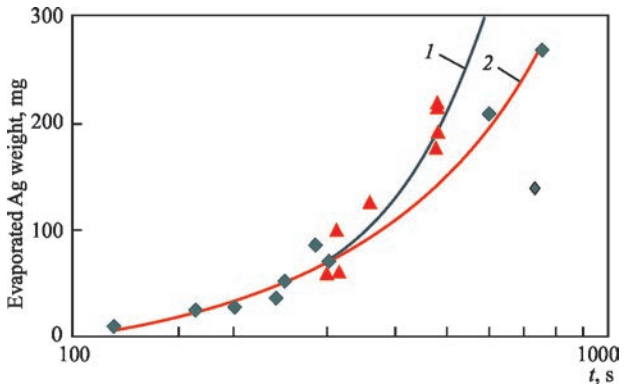

Figure 2. Dependence of the evaporated silver weight on the initial weight of silver, reactor heating current and evaporation time: *1* — 1230–1470; *2* — 900–1000 mg; graphite reactor, reactor heating current – 0.19–0.20 A (*1*); 0.15–0.17 (*2*)

INVESTIGATION RESULTS

To assess the possibility of practical application of the electron beam technology for synthesis of silver NPs of the specified size, first the dynamics of evaporation of a silver sample of 900 mg and greater weight placed into the reactor, was studied. Figure 2 shows examples of the dynamics of silver evaporation during the evaporation process, depending on the evaporation process parameters. Following the evaporation dynamics in time, as will be shown below, will allow determination of the average size of silver nanoparticles by the average rate of silver evaporation.

However, as shown by the first series of experiments, it turned out to be problematic to evaporate a precisely specified amount of silver, using a sample of a weight much greater than the amount required for evaporation. If you need to evaporate, for instance, 100 mg of silver, and load 900 or 1500 mg of silver into the reactor, it is a difficult task. In order to conduct the experiments, the weight of the loaded sample was close to the required mass of evaporated material. Figure 3 gives the results of such numerical experiments, conducted in order to determine the dependence of the evaporated silver weight on the duration of the evaporation process. The technological parameters of the process of silver evaporation from the reactor were varied, namely: initial weight of silver, current of the reactor heating beam, silver evaporation rate and angle of the reactor tip inclination. The work does not give the results of using the reactor with the vertically directed reactor tip. It should be noted that the efficiency factor of the reactor increases with increase of the angle of the tip inclination up to the maximum at the angle of 90°, reaching 30 % and more, depending on the size of the container for the powder and the distance from the tip outlet to the surface of the powder in the container. Results given in Figure 3 allow determining the silver evaporation rate, and, as shown by further studies, the silver evaporation rate determines the average size of NPs. The initial weight of silver samples, the current

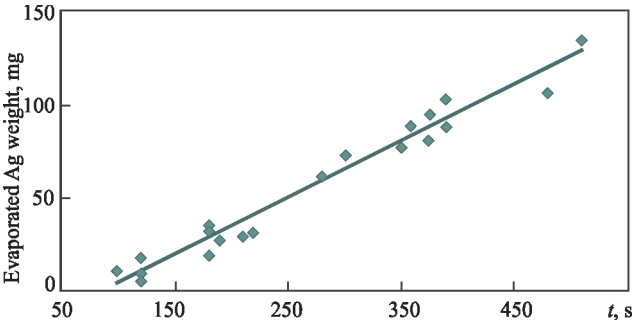

Figure 3. Dependence of the evaporated silver weight on the evaporation process duration

Table 1. Technological parameters of the processes of silver evaporation from a graphite reactor

Initial weight of Ag, mg	Evaporated Ag, mg	Beam current, A	Evaporation time, s	Average evaporation rate, mg/min
53.8	10.0	0.20–0.21	100	5.8
120.6	18.3	0.18–0.19	120	9.15
135.1	8.7	–»–	–»–	4.35
172.1	4.0	0.19...0.20	–»–	2.0
50.1	26.0	0.20	150	10.0
48.7	35.	0.21	180	13.0
49.8	30.8	0.210–0.215	–»–	10.3
54.70	18.3	0.23–0.21	–»–	6.1
31.7	27.7	0.18	190	8.8
51.0	28.0	0.21	210	8.0
39.8	31.3	0.21–0.22	220	8.5
75.9	61.4	–»–	280	13.2
83.6	73.5	0.20	300	14.7
80.0	77.2	–»–	350	12.9
136.4	87.9	0.21...23.0	360	13.5
79.3	79.3	0.19...0.20	375	12.2
98.0	95.6	0.20	–»–	14.7
98.0	95.6	–»–	–»–	–»–
115.6	87.4	0.20–22.0	390	13.4
148.4	103.7	0.21–0.23	–»–	16.0
116.4	105.0	0.20–22.0	480	13.1
142.0	136.2	–»–	510	16.0

Table 2. Fractional composition of silver NPs in H_2O–5 % PVP–Ag CS

Ag NPs	Most probable particle size, nm	Polymodal distribution		
		Fraction size, nm	Total particle weight, %	Total quantity of particles, %
First fraction	5.7	2–20	99.9	99.9
Second fraction	161	50–500	0.1	Less than 0.1

of the reactor heating beam, and the silver evaporation rate are shown in Table 1.

The average size of silver NPs was determined by the method of PCS of H_2O–1.4 % PVP–Ag H_2O–5 % PVP–Ag and Ethanol-2 % PVP–Ag colloidal systems. It was established earlier that the intensity of light scattering in colloidal solutions of H_2O–PVP and Ethanol-PVP systems is by 2 orders of magnitude lower on average, than that in H_2O–PVP–Ag and Ethanol–PVP–Ag systems. Given below are the results of investigation of the fractional composition and average size of silver NPs of the above CS.

The results of studying a sample of H_2O–5 % PVP–Ag CS (silver concentration in the CS was approximately 0.06 wt.%) one day after preparation are shown in Table 2 and in Figure 4.

Figure 5 gives the results of PCS-measurement of silver particle distribution in H_2O–14 % PVP–Ag CS (PVP

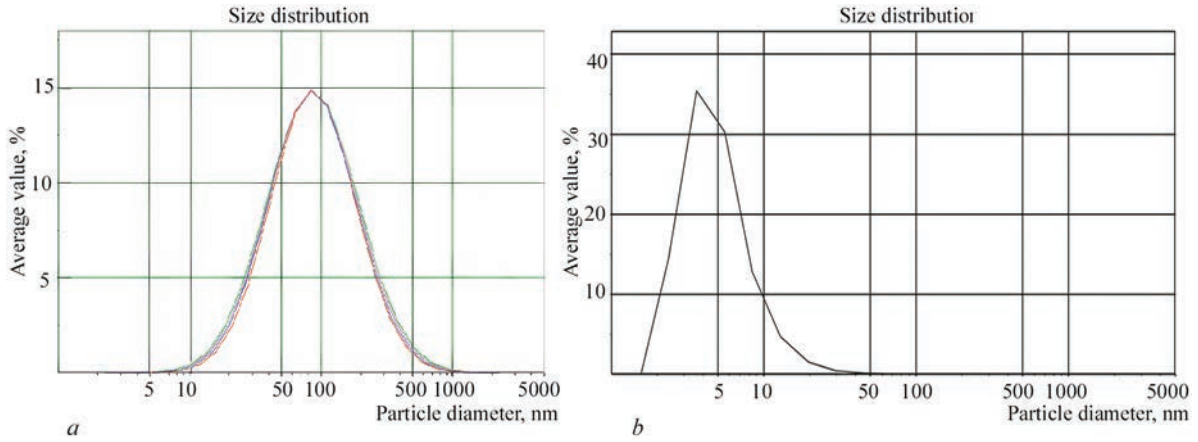

Figure 4. Laser correlation spectrum of H_2O–5 % PVP–Ag CS (*a*); particle size distribution by in CS (volume), 1 day after preparation

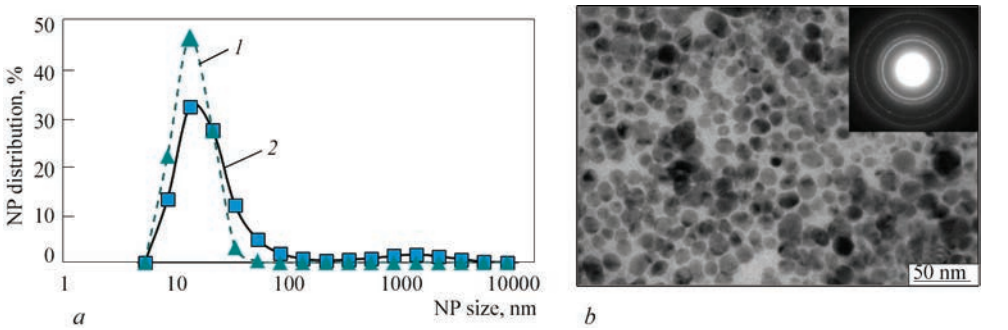

Figure 5. Silver particle size distribution in H_2O–1,4 % PVP–Ag CS determined by PCS measurement method: *1* — quantity; *2* — volume (*a*); silver particles (*b*)

Table 3. Composition of gels containing silver nanoparticles

Gel	Active ingredients	Base
1	Glucosamine (1.0 %) + PVP (2.0 %)	Hydrophylic: carbopol Ultrez — 2.0 %, glycerin — 5.0 %, purified water — up to 100 %
2	PVP (Ag 0.164 % - 0.1%) + PVP (2.0%)	
3	PVP (2.0 %)	
4	Glucosamine (1.0 % + PVP (Ag 0.164 % — 0.1 %) + PVP (up to 2.0%)	
5	Glucosamine (Ag 0.175 % — 0.1 %) + glucosamine (up to 1.0 %) + PVP	
6	Glucosamine (Ag 0.175 % — 0.01 %) + glucosamine (up to 1.0 %) + PVP	

Plasdon® K-15, molecular weight 8000) (*a*) and TEM of silver particles (*b*); molecular weight; average rate of silver evaporation was equal to 14.4 mg/min.

Figure 6 gives the dependence of average particle size in Ethanol-2 % PVP–Ag CS on silver evaporation rate, during obtaining of PVP–Ag composition according to the results of experiments and PCS measurements. As one can see, the average size of silver NPs depends on silver evaporation rate and with increase of the evaporation rate the general trend of the change of NP average size is directed towards decreasing of their size.

RESULTS OF STUDYING THE ANTIMICROBIAL ACTIVITY OF DRUG FORMS WITH SILVER NANOPARTICLES

As an example of practical application of PVP–Ag composition for development of medicinal substances with antimicrobial activity based on Ag nanoparticles we can cite investigation of antimicrobial activity of drug forms with silver nanoparticles of the average size of 10–12 nm in gel form. Six gels were developed at the Department of Plant Technology of Drugs of the National University of Pharmacy (NUPh, Kharkiv) (Table 3). Acute toxicity of the substances of glucosamine with nanosilver and PVP with nanosilver, as well as the gels, which were administered intragastrically, was studied using express-method on mice. Based on the results of previous studies of antimicrobial activity in vitro four promising samples of the gels were selected: 1, 2, 4 and 6 (Table 3). Reparative activity was studied in parallel with antimicrobial activity under in vivo conditions on a rat wound model. This model was selected as it allows studying not only the antibacterial activity of the drug, but also its reparative properties, as it reproduces three phases of the wound healing process at once: purulent-necrotic, granulation and epithelialization. Based on their composition, the studied gels should be the most active exactly in the first phase, demonstrating antibacterial (nanosilver), antiinflammatory and analgesic properties (glucosamine). As it is known, adequate therapy of the first phase of the wound process determines the speed of further reparative processes in the wound. The reference drug (Dermazin cream) was selected based on the fact that it contains 1 % sulphadiasine and is indicated for treatment of purulent wounds, that is compares well with the studied gels by its composition and indications. Treatment was begun three days after the wound infection, and the gels were applied once a

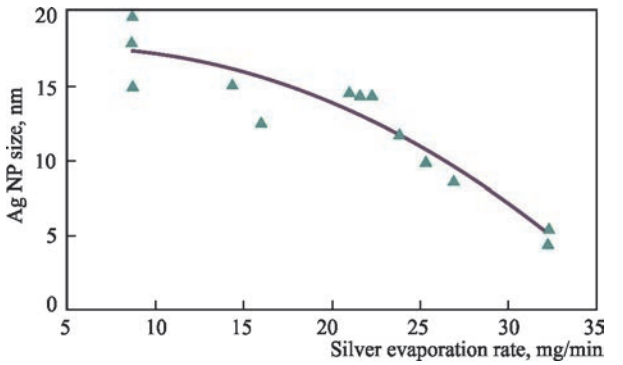

Figure 6. Average size distribution of silver NPs depending on silver evaporation rate. Measurements performed in Ethanol-2 % PVP–Ag CS

day in a thin layer in an empirical dose of 20 mg/cm^2. Wound suppuration was observed dynamically on the 1, 3, 5, 7, 9th day of the experiment. For an objective assessment of the therapeutic effect of the studied gels a morphological investigation of the wound surface zone was performed, and individual internal organs were examined for verification of the systemic action. Histological examination was performed on samples of the skin, heart, liver, and kidneys of the rats, for which the model pathology was reproduced — infected wounds, which healed naturally (control pathology), as well as samples of similar organs of the rats with infected wounds, which were treated with one of the gels with nanosilver (1, 2, 4 and 6) or with comparison drug — Dermazin ointment. Treatment with the studied gels with nanosilver and with the comparison drug was conducted for 9 days, beginning with the 3rd day after pathogen infection.

Based on the results of the conducted investigations, it was established that test-samples of gels 1, 2, 4, 5, 6 showed antimicrobial activity against gram-positive microorganisms (S. aureus). In relation to representatives of gram-negative microorganisms the following results were obtained: test-sample 1, 2, 3, 4 showed antimicrobial activity to P.aeruginosa; samples 2, 3 — to Kl.pneumoniae; sample 6 — to E.coli, respectively. Test-samples 2, 6 demonstrated moderate fungistatic activity. Investigations showed that the widest spectrum of selectively expressed antibacterial properties against the appropriately specified test strains is inherent in test samples 2, 6, 4. Considering the features of the composition of test-sample 2 (PVP (Ag 0.164 % — 0.1 %) + PVP (2.0 %) and the level of antimicrobial activity of test sample 6, it should be noted that the studied test-sample 4 is positively characterized by a pronounced bactericidal action against gram-positive (S.aureus) and gram-negative (P.a-eruginosa) microorganisms.

At application of the gel with glucosamine and silver nanoparticles, the wound area decreased by 51 %, that of the gel with glucosamine — by 13 %, that of the gel with silver nanoparticles — by 49 %, and that of Dermazin cream — by 32 %. On the 9th day the speed of reduction in the wound area of the declared sample was at the same level as the comparison drug. By epithelialization parameter already on the 9th day of the experiment in the group treated with helium with glucosamine and silver nanoparticles, complete healing of the wound had occurred in 40 % of the animals. While in the rest of the experimental samples epithelialization was observed only on the 11th day of treatment and was equal to 60 %, and in the group of officinal cream Dermazin it was 40 %.

Proceeding from the results of experimental planimetric studies we can conclude that the gel with glucosamine and silver nanoparticles contributes most to the acceleration of the regeneration and epithelialization processes, and by the expressiveness of the therapeutic effect it exceeds other gel samples and the reference drug. Analysis of the results of biochemical blood tests shows that wound treatment in animals with the declared gel helps reduce systemic manifestations of inflammation and destruction of the tissues.

CONCLUSIONS

1. Electron beam technology of evaporation and condensation in vacuum using a reactor for evaporation of Ag elements allowed synthesizing nanomaterials of PVP–Ag composition.

2. Dependence of the evaporated silver weight on the initial weight of silver, reactor heating current and process duration and average size distribution of silver NPs, depending on silver evaporation rate was established.

3. Obtained nanomaterial of PVP–Ag composition was used at the National University of Pharmacy (Kharkiv) to develop medicinal gels based on glucosamine with a low toxicity, wound healing ability and expressed bactericidal action under the conditions of purulent-necrotic wound process.

4. The best wound heating ability by the parameters of reliable normalization of biochemical, immunobiochemical and hematologic parameters during treatment was demonstrated by the gel of the following composition: glucosamine + 1.0 %; PVP + 0.164 % Ag, recalculated to silver it is 0.10; PVP — up to 2.0 %; carbopol Ultrez — 10–2.0 %; triethanolamine — up to pH 6.4; glycerin — 5.0 %; purified water — up to 100%, which exceeded the reference drug — Dermazin ointment by the epithelialization rate.

REFERENCES

1. Chekman, I.S., Movchan, B.A., Zagorodnyi, M.I. et al. (2008) Nanosilver: Technologies of manufacturing, pharmacological properties, indications for use. *Preparaty i Tekhnologii,* 51(**5**), 32–34 [in Russian].
2. Mokienko, A., Petrenko, N., Bozhenko, A. (2010) Stability of bacteria as an interdisciplinary problem. *Visnyk NANU,* **8**, 49–56 [in Ukrainian]. https://nasu-periodicals.org.ua/index.php/visnyk/article/view/4493
3. (2010) Weekly Pharmacy: A problem that needs an immediate solution! *Ezhenedelnik Apteka,* 766(**45**) [in Ukrainian]. www.apteka.ua
4. Jung, W.K., Koo, H.C., Kim, K.W. (2008) Antibacterial activity and mechanism of action of the silver ion in staphylococcus aureus and escherichia coli. *Appl. Environ. Microbiol.*, **74**, 2171–2178. DOI: https://doi.org/10.1128/aem.02001-07
5. Kim, J.S., Kuk, E., Yu, K.N. (2007) Antimicrobial effects of silver nanoparticles. *Nanomedicine,* 3(**1**), 95–101. DOI: http://dx.doi.org/10.1016/j.nano.2006.12.001
6. Chopra, I. (2007) The increasing use of silver-based products as antimicrobial agents: Useful development or a cause for concern? *J. Antimicrob. Chem.*, **59**, 587–590. DOI: https://doi.org/10.1093/jac/dkm006

7. Panacek, A., Kvitek, L., Prucek, R. et al. (2007) Silver colloid nanoparticles: Synthesis, characterization, and their antibacterial activity. *J. Phys. Chem*., 110(**33**), 16248–16250. DOI: https://doi.org/10.1021/jp063826h
8. Morones, J.R., Elechiguerra, J.L., Camacho, A.A. et al. (2005) The bactericidal effect of silver nanoparticles. *Nanotechnology,* **16**, 2346–2353. DOI: https://doi.org /10.1088/0957-4484/16/10/059
9. (2012) Compendium. *Medicinal preparations.* Kyiv, Morion [in Russian]. http://www. compendium.com.ua
10. Christian, P., Kammer, V., Balousha, P., Hofman, Th. (2008) Nanoparticles: Structure, properties, preparation and behavior in environmental media. *Ecotoxicology*, **17**, 326–343. DOI: http://dx.doi.org/10.1007/s10646-008-0213-1
11. Movchan, B.O., Yakovchuk, K.Yu. (2012) *Device and method of electron beam evaporation and vacuum directed deposition of vapor flow on substrate.* Pat. Ukraine, No. 98085, 10.04.2012 [in Ukrainian].
12. Yakovchuk, K.Yu. (2013) Application of electron beam evaporation technology for deposition of coatings on powder granules. *Tekhnologicheskie Systemy,* **3**, 49–55 [in Russian].
13. Kovinskii, I.S., Gornostai, A.V. (2012) Nanosized discrete copper oxide coatings on sodium chloride crystals deposited in vacuum from the vapour phase. *Advances in Electrometallurgy*, **2**, 146–149.

ORCID
G.G. Didikin: 0000-0002-9268-5072

CORRESPONDING AUTHOR
G.G. Didikin
E.O. Paton Electric Welding Institute of the NASU
11 Kazymyr Malevych Str., 03150, Kyiv, Ukraine.
E-mail: didikin@paton-icebt.kiev.ua

SUGGESTED CITATION
G.G. Didikin (2025) Synthesis and study of a pharmaceutical composition with silver nanoparticles, produced by electron beam evaporation. *The Paton Welding J.*, **5**, 30–37. DOI: https://doi.org/10.37434/tpwj2025.05.03

JOURNAL HOME PAGE
https://patonpublishinghouse.com/eng/journals/tpwj

Received: 22.01.2025
Received in revised form: 19.03.2025
Accepted: 30.05.2025

DOI: https://doi.org/10.37434/tpwj2025.05.04

STUDIES OF HYDRODYNAMIC PROCESSES DURING INGOTS CRYSTALLIZATION IN A CASTING MOLD UNDER CONDITIONS OF ELECTROSLAG HEATING AND STIRRING OF THE METAL POOL

I.V. Protokovilov, V.V. Barabash

E.O. Paton Electric Welding Institute of the NASU
11 Kazymyr Malevych Str., 03150, Kyiv, Ukraine

ABSTRACT

The results of the physical simulation of hydrodynamic processes at the crystallization of ingots in a casting mold under conditions of electroslag heating and stirring of the metal pool by a gas jet are presented. The studies were carried out on a cold transparent model that simulates the crystallization of a 205-ton steel ingot in a casting mold and allows visualizing hydrodynamic processes in the metal pool and forming a solid phase. New experimental data on the structure of hydrodynamic flows at various options of stirring the metal pool by a gas jet were obtained. It is shown that the use of a gas jet allows creating toroidal melt flows with upward flows spreading from the gas-supplying nozzle and downward flows near the walls of a casting mold. It was established that for effective stirring of the entire volume of the metal pool and to affect the crystals growing on the crystallization front, it is advisable to place the gas tuyere along the axis of the pool and choose its immersion depth within 70–80 % of the pool depth.

KEYWORDS: ingot, casting mold, physical simulation, hydrodynamics, electroslag heating, gas jet, stirring

INTRODUCTION

Today, the conventional technology of casting steel in a casting mold remains one of the most common methods of producing large forging ingots and slabs. This process is characterized by the presence of large volumes of liquid metal that solidifies for a long time under conditions of low-intensity thermal convection. This leads to a significant propagation of liquation and shrinkage processes and, as a result, physical and chemical heterogeneity of the cast metal [1–5]. Such defects cannot be completely eliminated during subsequent thermodeformational treatment. They are inherited by forgings and semi-finished products made from an ingot, which leads to a deterioration in the mechanical properties of the metal. Therefore, the problem of improving the technologies for making large ingots in a casting mold is still relevant.

One of the most promising ways to improve metal solidification conditions and eliminate defects of shrinkage and liquation origin is to apply a complex thermal and hydrodynamic effect on the metal pool [6]. It can be realized by means of electroslag heating (ESH) and feeding the ingot head and forced stirring of the metal pool with a gas jet. Under these conditions, it is important to understand the nature and intensity of hydrodynamic flows in the metal pool.

Experimental studies of the hydrodynamic processes that occur at the solidification of large ingots are very complex and expensive. In this case, it is advisable to apply physical modeling methods on cold transparent models, taking into account the following similarity criteria [7–10].

The aim of this study is to determine the effect of electroslag heating and forced purging of liquid metal with gas flows on hydrodynamic processes in the metal pool at the solidification of ingots in a casting mold.

RESEARCH PROCEDURE

The experiments were carried out on a cold, transparent physical model that allows visualizing hydrodynamic processes in the pool and forming the solid phase (Figure 1). The model represents a plane vessel simulating the longitudinal section of a 205-ton forging ingot. It is made at a scale of 1:15 to maintain the geometric similarity to a full-scale object. The bottom and side walls of the model are made of a water-cooled profile, while the front and rear walls are made of optically transparent material. The upper part of the vessel has polystyrene foam overlays simulating the heat-insulating inserts of the yield top.

A melt of sodium thiosulfate ($Na_2S_2O_3$) was used as a model liquid that simulates molten steel, which solidifies by the dendritic mechanism and retains optical transparency in the solid state. To visualize hydrodynamic flows, a coloring pigment was added to the sodium thiosulfate melt, which was precipitated in the form of suspended particles with neutral (zero) buoyancy (Figure 1, *b*).

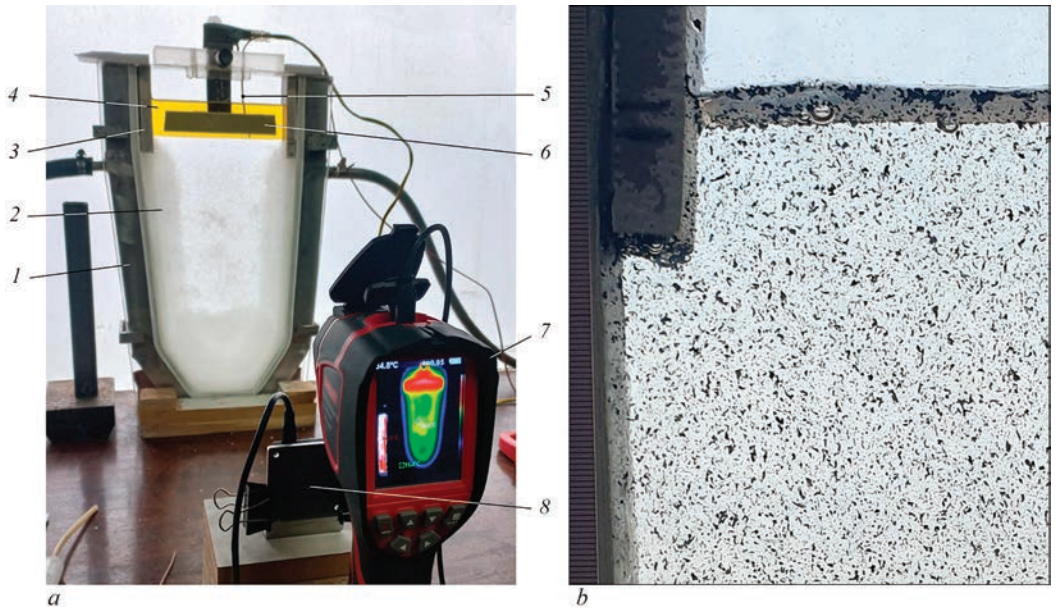

Figure 1. Appearance of a physical model for studying hydrodynamic processes at the ingot crystallization in a casting mold (*a*) and suspended particles in the model melt (*b*): *1* — water-cooled wall; *2* — wall made of optically transparent material; *3* — heat-insulating overlays; *4* — liquid simulating the slag pool; *5* — thermocouple; *6* — heating element; *7* — thermal imager; *8* — video camera

The correspondence between the hydrodynamic processes occurring during the simulation and in real conditions was assessed using the similarity criteria: Froude's criterion (Fr), which characterizes the ratio of inertia and gravity forces; Reynolds' criterion (Re), which determines the nature of hydrodynamic flows in the melt (laminar or turbulent); Weber's criterion (We), based on the ratio of liquid inertia forces to liquid surface tension forces; Grashof's criterion (Gr), which determines the melt motion caused by the non-uniformity of the temperature field.

Below are the calculated ratios for these similarity criteria:

$$\mathrm{Fr} = V^2/gL,\ \mathrm{Re} = VL/\nu,$$
$$\mathrm{We} = \rho V^2 L/\sigma,\ \mathrm{Gr} = g\beta(T_m - T_w)L^3/\nu^2,$$

where V is the flow velocity (m/s); g is the free fall acceleration (m/s^2); L is the characteristic size (m); ν is the kinematic viscosity of the liquid (m^2/s); ρ is the density of the liquid (kg/m^3); σ is the surface tension coefficient (N/m); β is the coefficient of thermal expansion (1/K); T_m is the melt temperature (K); T_w is the temperature of the casting mold wall (K).

The values of the relevant physical parameters and similarity criteria calculated for the model and the full-scale process are given in Tables 1 and 2. In both cases, the Fr criterion is significantly less than 1, which indicates the dominance of gravity forces over inertial forces. This is typical for the processes with stable convective liquid flows, without significant oscillations and surges. The We criterion is also less than 1 in both cases, which indicates the dominance of surface tension forces over inertial forces and the stability of the melt surfaces and the absence of ruptures of these surfaces. The Gr criterion for both the full-scale process and the model has very high values, which indicates a

Table 1. Physical parameters of the model and a full-scale process

Parameter	Physical model (sodium thiosulfate)	Full-scale process (steel)
Melt temperature (T_m), °C	68	1520
Casting mold wall temperature (T_w), °C	20	850
Flow velocity (V), m/s	0.01	0.015
Characteristic dimension (L), m	0.07	0.5
Thermal conductivity coefficient (λ), W/m·K	0.55	30
Density (ρ), kg/m^3	1670	7000
Kinematic viscosity (ν), m^2/s	$1.05\cdot10^{-6}$	$8.5\cdot10^{-7}$
Surface tension coefficient (σ), N/m	0.09	1.6
Thermal expansion coefficient (β), 1/K	$4.5\cdot10^{-4}$	$1.2\cdot10^{-5}$

Table 2. Values of similarity criteria for the physical model and the full-scale process

Similarity criterion	Physical model	Full-scale process
Fr	$1.5 \cdot 10^{-4}$	$4.6 \cdot 10^{-5}$
Re	$7.0 \cdot 10^{2}$	$8.8 \cdot 10^{3}$
We	0.13	0.49
Gr	$7.3 \cdot 10^{7}$	$1.3 \cdot 10^{10}$

significant influence of the natural convection on the movement of both melts. The value of the Re criterion in the full-scale process exceeds the critical value of $R_e \approx 2300$, which indicates the probability of turbulent flows formation in the steel melt.

In general, the analysis of the similarity criteria indicates the correspondence of the studied processes in the model and a full-scale object and the possibility of a qualitative (representative) assessment of the hydrodynamic processes occurring during the solidification of a steel melt in a casting mold using the developed physical model.

The sodium thiosulfate was melted in a muffle furnace and then fed into the model vessel using siphon filling at a temperature of 68–72 °C.

To model the ESH process, oil was poured onto the melt surface to simulate a slag pool. The oil was heated using a heating element immersed in it, and its temperature was maintained at 52–62 °C. The melt temperature was monitored using a thermocouple and a "Wintact WT3160" thermal imager.

Forced stirring of the melt was carried out by gas purging. For this purpose, a ceramic tube with a metal nozzle (tuyere) was used, which was immersed into the melt at different depths and in different places (along the axis and with a displacement from the axis). Purging was carried out periodically for 30–60 s. Argon was used as a gas, which was supplied at a flow rate that did not lead to an unacceptable excitation of the free surface of the pool. Hydrodynamic flows in the melt were studied by analyzing video records of the movement of suspended particles in it.

The experiments were carried out under the conventional ingot solidification scheme (without an external impact), with the use of ESH, as well as with the use of ESH and with various options of stirring the metal pool with a gas jet.

EXPERIMENTAL RESULTS AND DISCUSSION

Figure 2, *a* shows the structure of hydrodynamic flows of the model melt after its casting. It is characterized by downward liquid flows, which are localized in a rather narrow volume directly near the water-cooled walls of the vessel. The velocity of these downward flows is about 4.8 mm/s. The upward flows of the melt are dispersed throughout the central part of the pool and their velocity is on average 1.5 mm/s (Figure 3, *1*). Obviously, this flow structure results from the thermogravity convection caused by the cooling effect of the vessel walls.

The use of ESH did not change the structure and intensity of melt flows much (Figure 2, *b*). Downward liquid flows with a velocity of up to 4.2 mm/s occurred near the pool walls at a distance of not more than 20 mm, and low-intensity upward flows were dispersed in the central part of the pool (Figure 3, *2*). However, within 20 min after the melt was cast, when a layer of frozen sodium thiosulfate formed on the walls of the vessel, the flow

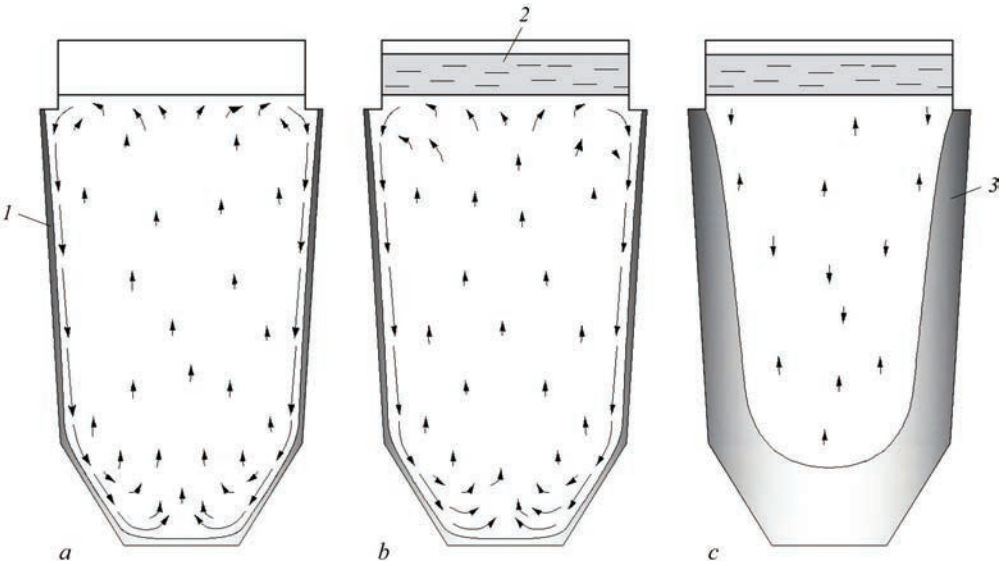

Figure 2. Structure of hydrodynamic melt flows: *a* — without external impact; *b* — with ESH; *c* — with ESH after the formation of a solidified ingot layer (*1* — vessel wall; *2* — liquid simulating the slag pool; *3* — solidified ingot layer)

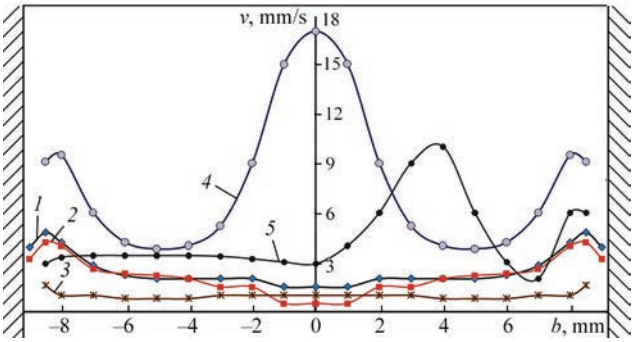

Figure 3. Distribution of flow velocity across the pool width (*b*) at the horizon $0.75 \times h_{pool}$ for different modeling schemes: *1* — without external impact; *2* — with ESH; *3* — with ESH within 20 min after casting; *4* — with stirring when the tuyere is immersed along the axis to 80 % of the pool depth; *5* — with stirring when the tuyere is immersed asymmetrically at 50 % of the pool depth

structure changed significantly: the melt flow almost completely stopped throughout the entire volume of the pool (Figure 2, *c*; Figure 3, *3*). In other words, under conditions when the cooling effect of the vessel walls due to the formation of a frozen layer of sodium thiosulfate on them is significantly reduced, and heat is fed by ESH in the upper layers of the pool, there are no factors for the occurrence of thermogravity convection. Such conditions of metal solidification without melt stirring cannot be considered favorable for overcoming liquation phenomena during the ingot solidification. In this case, it is advisable to use forced stirring of the metal pool.

Figure 4 shows the structures of hydrodynamic flows of the melt when using gas purging jet. The obtained data indicate that gas purging creates intense toroidal melt flows with upward flows spreading from the gas supply nozzle and downward flows near the vessel walls. This is created by the upward motion of gas bubbles that propagate from the nozzle and in turn bring the melt into motion. In this case, melt flows are

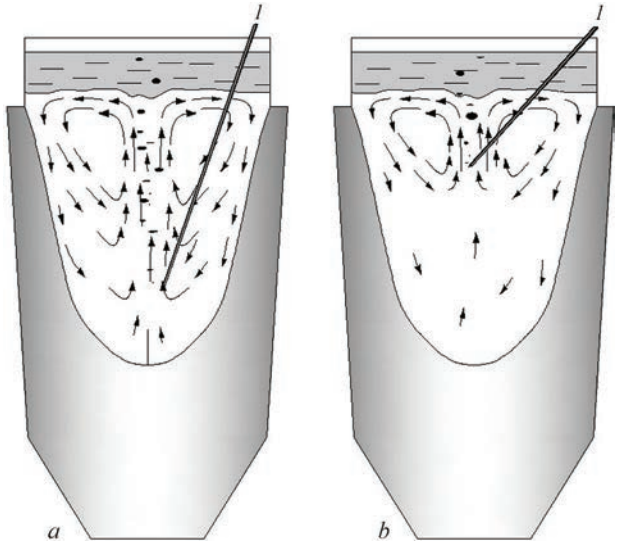

Figure 5. Structure of hydrodynamic flows during gas purging of the pool after 2 hours from the beginning of the experiment: *a* — immersion of the tuyere (*1*) to 70 % of the pool depth; *b* — at 28 %

formed mainly in the horizons above the gas supply nozzle. In other words, when gas flow rates do not lead to an unacceptable excitation of the free surface of the pool, the gas jet does not spread significantly below the nozzle. As a result, when the tuyere was immersed to a depth of 30 % of the total pool depth, forced melt stirring occurred only in a small volume concentrated in the upper layers in the centre of the vessel (Figure 4, *a*). At the same time, melt flows did not reach the crystallization front.

As the immersion depth of the tuyere increased, the volume of the melt involved in the toroidal motion increased (Figure 4, *b*), and only when the tuyere was immersed to a depth of at least 70–80 % of the total pool depth, the toroidal motion was formed in its entire volume (Figure 4, *c*). Under these conditions,

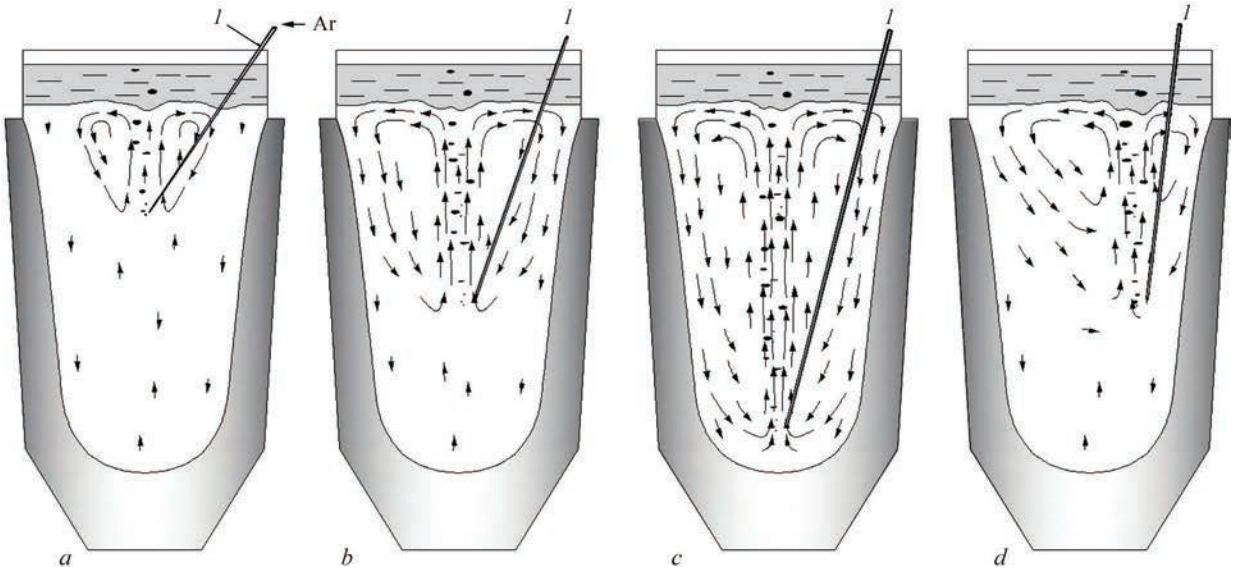

Figure 4. Structure of hydrodynamic flows during gas purging of the pool: *a* — tuyere immersion to 30 % of the pool depth; *b* — at 50; *c* — at 80; *d* — asymmetric tuyere immersion; *1* — tuyere

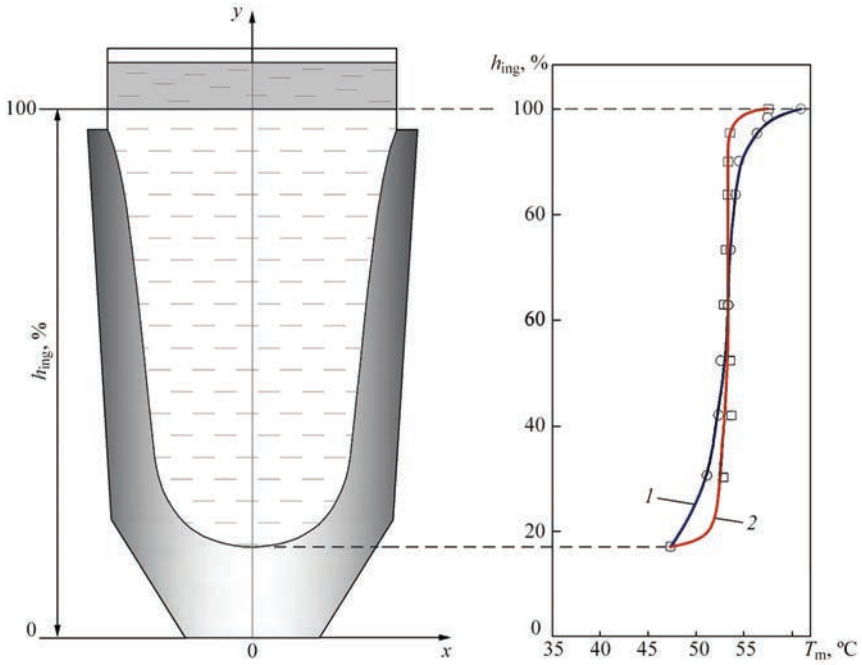

Figure 6. Temperature distribution over the height of the model liquid without (*1*) and with stirring (*2*)

forced melt flows washed the crystallization front along its entire length. The maximum velocity of upward flows along the pool axis was 17.0 mm/s, and 9.5 mm/s for downward flows near the walls of the vessel (Figure 3, *4*).

A flow structure which similar to that described above was observed when pool stirring was applied after 2 hours from the start of the experiment, when about 50 % of the ingot volume was formed (Figure 5, *a*, *b*).

The asymmetric arrangement of the tuyere in the vessel created an asymmetric toroidal melt motion (Figure 4, *d*). At the same time, melt flows washed the crystallization front on the one side of the vessel, but not on the opposite side. Such a flow structure cannot be considered effective to influence the ingot structure formation and liquation processes at the crystallization front. An exception may be made when at the purging process, it can be provided that the tuyere could move in a circle at a certain distance from the casting mold wall.

Figure 6 shows the temperature distribution of the model liquid across the cross-section of the vessel in the experiments without melt stirring and with (with the tuyere immersed to a depth of 70 % of the pool depth). As shown in the given data, melt stirring leads to a equalizing of the temperature over the height of the pool (Figure 6, *2*). This redistribution of temperature in the bottom part of the pool should reduce the length of the two-phase zone and, accordingly, the propagation of the liquation processes occurring at the ingot solidification.

In general, the obtained results confirm the prospects of using a gas jet for melt stirring, equalizing the temperature in the pool volume and influencing the liquation processes at the ingot solidification in a casting mold. For effective stirring of the entire volume of the metal pool and influencing the crystals growing at the crystallization front, it is advisable to place the tuyere along the pool axis and choose its immersion depth within 70–80 % of the pool depth. Under these conditions, downward flows of the melt reach the bottom of the pool and then spread upwards along the entire crystallization front. At the same time, the maximum admissible gas flow rates, which are determined by its pressure and nozzle diameter, are limited by the excitation of the free surface of the pool, melt spattering and deterioration of process stability.

The obtained results will be used in further studies to optimize the parameters of gas purging while casting model steel ingots in a casting mold.

CONCLUSIONS

1. A physical model was developed to study hydrodynamic processes in the metal pool during ingot casting in a mold under conditions of electroslag heating and stirring with a gas jet.

2. It is shown that using the conventional casting scheme, downward flows of the melt are formed near the walls of the casting mold, while upward flows are dispersed throughout the whole central part of the pool and have a lower velocity. As a solidified layer of the metal forms on the walls of the casting mold, the velocity of hydrodynamic flows throughout the

pool volume decreases significantly, until it stops completely.

3. It was found that the use of ESH does not lead to a noticeable change in the structure and velocity of hydrodynamic flows of the melt.

4. It is shown that gas purging creates intense toroidal melt flows with upward flows spreading from the gas supply nozzle and downward flows near the mold walls. In this case, the melt flows are formed mainly in the liquid volumes above the gas supply nozzle.

5. It was established that for effective stirring of the entire volume of the metal pool and impact on the crystals growing at the crystallization front, it is advisable to place the tuyere along the pool axis and choose its immersion depth within 70–80 % of the pool depth.

REFERENCES

1. Smirnov, A.N., Makurov, S.L., Safonov, V.M., Tsuprun, A.Yu. (2009) *Large ingot.* DNTU, Donetsk, Veber [in Russian].
2. Maidorn, C., Blind, D. (1985) Solidification and segregation in heavy forging ingots. *Nuclear Engineering and Design*, 84(**2**), 285–296. DOI: https://doi.org/10.1016/0029-5493(85)90199-2
3. Sang, B.G., Kang, X.H., Liu, D.R., Li, D.Z. (2010) Study on macrosegregation in heavy steel ingots. *Inter. J. of Cast Metals Research*, 23(**4**), 205–210. DOI: https://doi.org/10.1179/136404610X12665088537374
4. Pickering, E.J., Al-Bermani, S.S., Talamantes-Silva, J. (2015) Application of criterion for A-segregation in steel ingots. *Mater. Sci. and Technol.*, 31(**11**), 1313–1319. DOI: https://doi.org/10.1179/1743284714Y.0000000692
5. Honghao, Ge, Fengli, Ren, Jun, Li et al. (2018) Modeling of ingot size effects on macrosegregation in steel castings. *J. of Materials Proc. Technology*, **252**, 362–369. DOI: https://doi.org/10.1016/j.jmatprotec.2017.09.004.
6. Shapovalov, V.O., Biktagirov, F.K., Barabash, V.V. et al. (2024) New method for improving physical homogeneity of steel ingots. In: *Proc. of the VII Inter. Conf. on Welding and Related Technologies, 7–10 October 2024*, 21–24. DOI: https://doi.org/10.1201/9781003518518-4
7. Marx, K., Rodl, S., Schramhauser, S., Seemann, M. (2014) Optimization of the filling and solidification of large ingots. *La Metallurgia Italiana*, 106(**11–12**), 11–19.
8. Protokovilov, I.V., Porokhonko, V.B., Biktagirov, F.K. et al. (2019) Physical modeling of ingot crystallization in a mold under conditions of electroslag heating and feeding. *Suchasna Elektrometal.*, **3**, 3–9 [in Russian]. DOI: https://doi.org/10.15407/sem2019.03.01
9. Eldarkhanov, A.S., Efimov, V.A., Nuradinov, A.S. (2001) *Processes of formation of castings and their modeling.* Moscow, Mashinostroenie [in Russian].
10. Protokovilov, I.V., Porokhonko, V.B. (2017) Physical modeling of electrode metal drop transfer in ESR with superposition of pulsed magnetic fields. *Suchasna Elektrometal.*, **3**, 9–13 [in Russian]. DOI: https://doi.org/10.15407/sem2017.03.02

ORCID

I.V. Protokovilov: 0000-0002-5926-4049,
V.V. Barabash: 0000-0001-8138-3565

CONFLICT OF INTEREST

The Authors declare no conflict of interest

CORRESPONDING AUTHOR

I.V. Protokovilov
E.O. Paton Electric Welding Institute of the NASU
11 Kazymyr Malevych Str., 03150, Kyiv, Ukraine.
E-mail: lab38@paton.kiev.ua

SUGGESTED CITATION

I.V. Protokovilov, V.V. Barabash (2025) Studies of hydrodynamic processes during ingots crystallization in a casting mold under conditions of electroslag heating and stirring of the metal pool. *The Paton Welding J.*, **5**, 38–43.
DOI: https://doi.org/10.37434/tpwj2025.05.04

JOURNAL HOME PAGE

https://patonpublishinghouse.com/eng/journals/tpwj

Received: 19.02.2025
Received in revised form: 08.04.2025
Accepted: 22.05.2025

DOI: https://doi.org/10.37434/tpwj2025.05.05

METHODOLOGY FOR EVALUATION OF THE WELDING AND TECHNOLOGICAL PROPERTIES OF FLUX-CORED WIRES FOR ARC SURFACING

A.A. Babinets, I.O. Ryabtsev, I.P. Lentyugov

E.O. Paton Electric Welding Institute of the NASU
11 Kazymyr Malevych Str., 03150, Kyiv, Ukraine

ABSTRACT

An analysis of existing methods for evaluating the welding and technological properties of electrode materials used in arc surfacing (welding) has been conducted. The fundamental principles for assessing the stability of the arc process have been reviewed. Key approaches to investigating the properties of electrode materials and the list of controlled parameters most frequently utilized for this purpose have been identified. It has been demonstrated that quantitative evaluation criteria are more advantageous compared to qualitative ones. Based on the analysis, a comprehensive methodology for evaluating the welding and technological properties of flux-cored wires has been developed, comprising three main components. The first component includes a visual expert assessment of the arc surfacing process and the quality of the deposited metal formation, performed using a differential scoring system. The second component focuses on evaluating the melting characteristics of flux-cored electrode wires based on experimentally determined melting rates, deposition rates, and material loss coefficients. The third component involves assessing the stability of the arc process, which is conducted using experimentally determined coefficients of variation for current and voltage fluctuations in the arc. The advantages of the proposed comprehensive methodology have been demonstrated through the evaluation of the properties of real flux-cored wires for arc surfacing. It has been established that this methodology provides more informative results compared to approaches relying solely on qualitative indices. The study confirmed that the type and granulometric composition of the metallic components in the core of flux-cored wires influence the stability of the arc surfacing process. The use of chemically purer and more homogeneous metallic granular powders in the wire core, compared to ferroalloy powders, improves the stability and productivity of the surfacing process by 15–30 %.

KEYWORDS: arc surfacing, flux-cored wire, deposited metal, welding and technological properties, surfacing stability, coefficients of variation

INTRODUCTION

It is known that flux-cored wire is a highly productive material, capable of solving a wide range of tasks, in particular those related to manufacture or restoration by arc surfacing methods of parts used in various sectors of industry [1–3].

Flux-cored wire consists of a metal sheath (from soft steel, nickel, titanium strip, etc) and core, filled with powder components. The core composition includes alloying components (ferroalloys, pure metals, carbides, borides, etc), which ensure the required chemical composition and properties of the deposited metal [1–3]. In addition to alloying elements, deoxidizing, gas- and slag-forming components are often added to the core composition, which promote shielding and refining of the molten metal. Light ionizing additives, stabilizing the arc discharge, can also be added to the core, which improves the surfacing (welding) process efficiency [1–5].

The advantages of flux-cored wires are their versatility, wide possibilities for deposited metal alloying, as well as high productivity, which ensures a significant reduction in material costs [1, 5, 6]. Due to that the flux-cored wires are used successfully in the processes of mechanized and automatic surfacing (welding). By their operational characteristics, they are practically not inferior to solid wires, so that serial equipment can be used for surfacing [6].

Compared to flux-cored wire surfacing, however, application of solid electrode wires allows producing metal of a more homogeneous chemical composition and properties. This is due to higher stability of the deposition process in the second case.

The high stability of the surfacing process, and, thus, greater homogeneity of the deposited metal by its composition and properties are particularly important during deposition of corrosion-, gas-erosion- and wear-resistant layers on critical parts, operating in the chemical, oil and gas, metallurgical and other industries. In such cases, during selection of electrode materials, there arises the need for evaluation of their welding and technological properties, as well as studying the influence of numerous factors, among which the composition of the flux-cored wire filler (core) is of key importance.

THE OBJECTIVE OF THE WORK

is analysis of the available procedures for evaluation of welding and technological properties of electrode materials, used in surfacing (welding), as well as de-

velopment of the respective methodology for arc surfacing methods with application of flux-cored electrode wires.

ANALYSIS OF REFERENCE SOURCES

Stability of the surfacing (welding) process is one of the key parameters of welding and technological properties of electrode materials. At the same time, it is a complex and multifactorial concept, for which there is no unified standardized evaluation methodology [4, 7]. Stability depends on the parameters of the object of study. The researchers choose or develop the methodology for stability determination in each specific case, depending on the defined tasks.

Various technological measures are applied to increase the uniformity of melting of the flux-cored wire core and sheath, in order to improve the homogeneity of the obtained deposited metal. Among them are increase in the fraction of metallic powders in the core composition, selection of low-melting compositions for slag-forming components, reduction of sheath thickness, etc [3].

The welding and technological properties of electrode materials are often evaluated by visual examination of the produced samples and analysis of the quality of formation of the deposited bead or weld [8–11]. Visual examination is conducted using a magnifying glass with magnification of ×2–5, with recording of the controlled parameters. They include: correspondence of the geometrical dimensions of the deposited bead (or weld) to technical documentation; dimensional stability along the entire length of the controlled segment; absence of undercuts or visible defects, etc. Such a methodology, however, allows only indirect evaluation of the arc process stability.

In the opinion of the authors of [3, 4, 6], the arc process stability can be effectively evaluated using quantitative indices. The process is considered to be stable, if deviation of its parameters from the average values does not exceed the specified level. A measure of stability in this case is the parameter deviation from its average value. Dispersion, mean-root-square deviation or coefficient of variation can be used as such a measure [12].

So, in [6] the following criteria were selected, in order to determine and optimize the welding and technological characteristics of coated electrodes and welding wire: average and critical short-circuiting frequency, coefficients of variation of the respective frequency, as well as the average and maximal weight of the metal drop.

In [5, 13] devoted to welding with self-shielded flux-cored wires, the process stability was assessed by analyzing the coefficients of variation of the welding current and voltage, as well as the average time and frequency of short-circuits determined using a system equipped with a high-speed analog-to-digital converter. Slag crust separability, presence of defects and metal losses due to spattering were assessed additionally.

Welding and technological properties of the electrodes were evaluated in [14] using a comprehensive point scoring system, taking into account the following controlled parameters: ease of arc excitation, weld formation quality, degree of metal spattering, covering property and ease of slag separation and presence of defects. Arcing stability was assessed using an automated complex of diagnostics and monitoring of the welding process parameters, also converting the derived data into final points.

In [15, 16] during surfacing with flux-cored wires and strips a methodology of evaluation of the welding and technological properties was used, which is based on determination of the quality of the deposited metal formation, melting and deposition rates, coefficients of spattering losses and arc burning stability. The quality of formation was assessed by the ratio of the deposited bead width (b) to its height (h). In the opinion of the authors of the mentioned works, the greater value (b/h), the higher is the quality of formation. Stability was determined by the value of the coefficients of variation by voltage and current: they smaller they are, the more stable is the process of arc burning.

In [17] the welding and technological properties of flux-cored wire microalloyed with boron, were assessed by a complex methodology, which incorporated the following quality parameters: mode of arc excitation (light, medium, complicated); arc burning stability (stable, satisfactory, unstable); quality of the deposited bead formation (high-quality, satisfactory, poor); type and presence of defects in the deposited metal (absent, isolated, considerable quantity); quality of slag crust separation (easy, satisfactory, complicated); compliance of the chemical composition and hardness of the deposited metal with the technical requirements (compliance, non-compliance). Melting characteristics were also evaluated by quantitative characteristics: melting and deposition rates and coefficient of losses.

DEVELOPMENT OF THE METHODOLOGY FOR EVALUATION OF WELDING AND TECHNOLOGICAL PROPERTIES OF FLUX-CORED WIRES FOR ARC SURFACING

Summing up the data presented, one can state that evaluation of the welding and technological properties of electrode materials for surfacing should be

comprehensive, in order to increase the informativeness and validity of their selection. Such key parameters should be taken into account as: characteristics of electrode wire melting, presence of defects, quality of deposited metal formation, and quality of slag crust separation (if the methods of submerged-arc or self-shielded flux-cored wire surfacing are used).

In our opinion, it is rational to evaluate the quality of deposited metal formation using a differential scoring system. Application of mathematical expressions for such an assessment, based on the relationship of its parameters [15], has no practical benefit, as the deposition modes are usually selected, taking into account the requirements to ensuring the specified penetration depth, width and height of the deposited bead [1].

It is rational to perform evaluation of the arc process stability on the base of quantitative characteristics. This is particularly important with application of electrode materials with similar characteristics, when visual determination of the arc process stability is greatly complicated. The most accurate and informative assessment can be achieved by analysis of integral values, which determine the energy state of the arc process. Examples of such values are arc voltage and current, which are recorded multiple times during the process [4].

Based on the conducted analysis and results of our own experimental research [17, 18], we developed the following methodology of comprehensive assessment of the welding and technological properties of flux-cored wires for surfacing, which consists of three components.

The first component includes visual expert evaluation of the arc surfacing process and the produced deposited metal, using the differential scoring system (Table 1). The controlled parameters used by this component are as follows: mode of arc excitation, quality of the deposited metal formation, presence of visible defects, correspondence of the deposited metal chemical composition to the requirements and quality of the slag crust separation (provided the submerged-arc or self-shielded flux-cored wire surfacing method is used).

The second component contains evaluation of the melting characteristics (productivity) of flux-cored electrode wires, which is determined by the rates of melting and deposition and coefficient of losses. The melting rate (α_m) characterizes the specific (referred to one ampere of welding current) productivity of the wire melting process. The deposition rate (α_d) characterizes the specific productivity of the deposition process. Losses of electrode metal (allowing for burnout and spattering losses) are characterized by the coeffi-

Table 1. Monitored values of welding and technological properties of flux-cored wires for surfacing with point score by the differential method

Monitored parameter	Point score	Brief characterization of the parameter
Mode of arc excitation	0	Poor. Ignition not from the first touch of the electrode to the workpiece or absence of ignition
	1	Satisfactory. Ignition without electrode sticking
	2	Good. Ignition right after the first touch of the electrode to the workpiece
Quality of the deposited metal formation	0	Poor. Bead is non-uniform by width and height, surface is coarse-scaled
	1	Satisfactory. Isolated unevenness by the width or height, also at the edges, surface is finely-scaled
	2	Good. Bead is uniform, with a smooth transition to the base metal, surface is smooth
Presence of visible defects (pores, cracks, lack-of-fusion)	0	One or more cracks > 5 mm long and/or chains, clusters of pores
	1	No cracks. Isolated pores at > 100 mm distance
	2	No defects
Compliance of the chemical composition of the deposited metal with technical requirements	0	Does not comply. Deviations of the weight fraction of any element by more than ± 10 % from its specified value or deviation of the weight fraction for two or more elements by more than ± 5 from their specified values
	1	Partial compliance. Deviation of weight fraction for any element by more than ± 5 % of its specified value or deviation of the weight fraction for two or more elements by more than ± 2.5 % of their specified values
	2	Complies. Chemical composition of the metal is in the specified range by all the elements
Quality of slag crust separation	0	Poor. After completion of the surfacing process the crust does not separate
	1	Satisfactory. Separates at partial mechanical impact
	2	Good. Separates after deposition without additional mechanical impact

cient of losses (ψ). The above coefficients are calculated using the following expressions [17, 18]:

$$\alpha_m = \frac{G_m}{It}; \quad (1)$$

$$\alpha_m = \frac{G_d}{It}; \quad (2)$$

$$\psi = \frac{\alpha_m - \alpha_d}{\alpha_m} 100\%, \quad (3)$$

where G_m is the molten metal weight; g; G_d is the deposited metal weight, g; I the welding current, A; t is the deposition time, h.

The higher the melting and deposition rates and the smaller the losses coefficient, the higher is the productivity of flux-cored wire surfacing.

The third component contains an evaluation of the stability of the arc surfacing process, which it is proposed to perform based on the dispersion of instantaneous values of arc current and voltage with their multiple recording, using the calculated respective coefficients of variation. Application of the coefficient of variation as a controlled parameter allows elimination of the influence of the scale of different samples of the derived data.

To record the mode parameters during the deposition process, it is necessary to use devices with high-speed analog-digital converters and function of saving the derived data. In our work a digital recording multimeter ANENG AN9002, fitted with a high-speed analog-digital converter, was used for this purpose. The multimeter saves measurement results in its memory in real time and allows transmitting them to other devices, using the Bluetooth communication technology.

Analysis of the derived instantaneous values of arc current and voltage, using the calculated coefficients of variation, can be performed with application of standard tools, included into the programs for mathematical analysis, such as for instance Microsoft Excel, MathLab, etc. [19]. In this work, built-in functions of mathematical analysis of Microsoft Excel program were used.

To determine the coefficient of variation, it is necessary to first calculate the standard deviation (S). For this purpose we can use the built-in function STDEV (number 1; …), where number 1 is the first numeric argument, which corresponds to a sample from the population. Instead of the arguments separated by a semicolon, an array or an array reference can be used. STDEV function calculates the standard deviation by the following formula:

$$S = \sqrt{\frac{\sum (X - \dot{X})^2}{n-1}}, \quad (4)$$

where X is the sample mean; n is the sample size.

Then, it is necessary to determine the arithmetic mean (X) using AVERAGE (number1; …) function, where number 1 is the first number, reference to a cell or range, for which it is necessary to calculate the mean value. Here, it should be taken into account that AVERAGE function calculates the mean value, i.e. the center of the set of numbers in the statistical distribution. There are three most common ways to determine the mean value:

1. Arithmetic mean value is calculated by adding up a set of numbers and then distributing the resulting sum by their number.

2. Median is the number, which is the middle of a set of numbers, i.e. half of the numbers have values larger than the median, and half of the numbers have values smaller than the median.

3. Mode is the number that occurs most often in this set of numbers.

At symmetrical distribution of the set of numbers, these values of evaluation of the degree of centralization are equal. At asymmetrical distribution of a set of numbers they can differ, which should be taken into account in calculations.

The coefficient of variation is known to express the extent of variation of the studied parameter, and it is determined by the ratio of mean root square deviation (S) to the mean value of parameter (X), i.e. it is calculated by the following expression:

$$V = \frac{S}{\dot{X}}, \quad (5)$$

where S is the standard (mean-root-square) deviation; X is the arithmetic mean.

For the general case it is assumed that if the value of the coefficient of variation is smaller than 33 %, the set is believed to be homogeneous, and if it is larger than 33 %, the set is heterogeneous. In practice, during determination of the arc process stability by comparing the coefficients of variation by current and voltage, the process for which these coefficients are smaller, will be more stable. The coefficient of variation is usually expressed in percent.

Moreover, during statistical analysis of the data, often it is rational to plot the histogram of a certain parameter distribution, which allows visual evaluation of the magnitude and nature of the data scatter. In Excel program the distribution histogram is a bar chart, in which each bar is a range of values (pocket), and the bar height is proportional to the number of values in it (frequency of observations). In order to construct

Table 2. Comparative evaluation of welding and technological properties of experimental wires and stability of the process of arc surfacing with experimental wires

No.	Composition of flux-cored wire core, fraction size	Mode of arc excitation	Quality of deposited metal formation	Defects	Compliance of deposited metal chemical composition	Quality of slag crust separation	Total score	Coefficients, %				
								melting	deposition	losses	variation by current	variation by voltage
1	PG-R6M5 powder, 50–300 μm	2	2	2	2	1	9	17.1	16.8	1.75	14.12	4.73
2	PG-R5M5 powder, 200–250 μm	2	1	2	2	1	8	16.2	15.8	2.47	14.71	4.99
3	Mixture of ferroalloy powders, 50–300 μm	2	1	2	2	1	8	13.6	12.6	7.35	16.18	6.08

the distribution histogram in Excel, there should be not less than 50 values in the data set. The histogram proper is formed with application of "Analysis Package" add-on.

As an example, this work gives an assessment of welding and technological properties of experimental flux-cored wires, which was conducted by the developed methodology. Comparison of the properties of flux-cored wires with different granulometric composition of the core material was performed, with granular metallic powder PG-R6M5 of two different fractions being applied as the core material in experimental wires (Table 2). Used as the standard was flux-cored wire with a core of a mixture of ferroalloy and other components, with their content calculated so as to ensure producing deposited metal of one chemical composition. The samples were produced by the method of submerged-arc surfacing under a layer of AN-26P flux. The modes of surfacing and heat treatment of all the samples were the same, and the samples were surfaced in five layers. The idea of the research is described in more detail in [18].

Results of evaluation of welding and technological properties of experimental flux-cored wires are given in Table 2. The appearance of the surfaced samples is shown in Figure 1, and the histograms of distribution of instantaneous values of arc current and voltage are presented in Figure 2.

As one can see from the derived data, evaluation of the welding and technological properties of flux-cored wires, having similar characteristics, by just the qualitative parameters according to the procedure of [17], without taking into account the data on productivity and stability of the process, yields practically the same results (see the total number of points in Table 2).

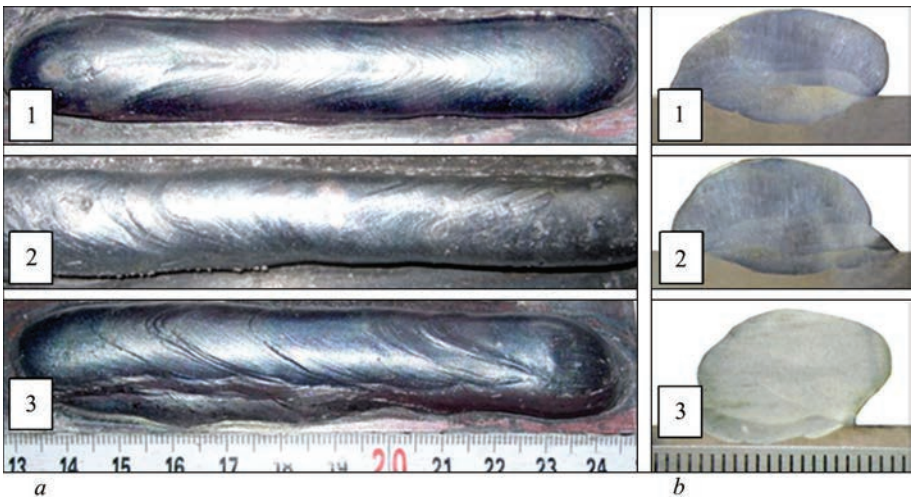

Figure 1. Appearance (*a*) and transverse macrosections (*b*) of samples surfaced in five-layers with wires Nos 1–3. Wire designations according to Table 2

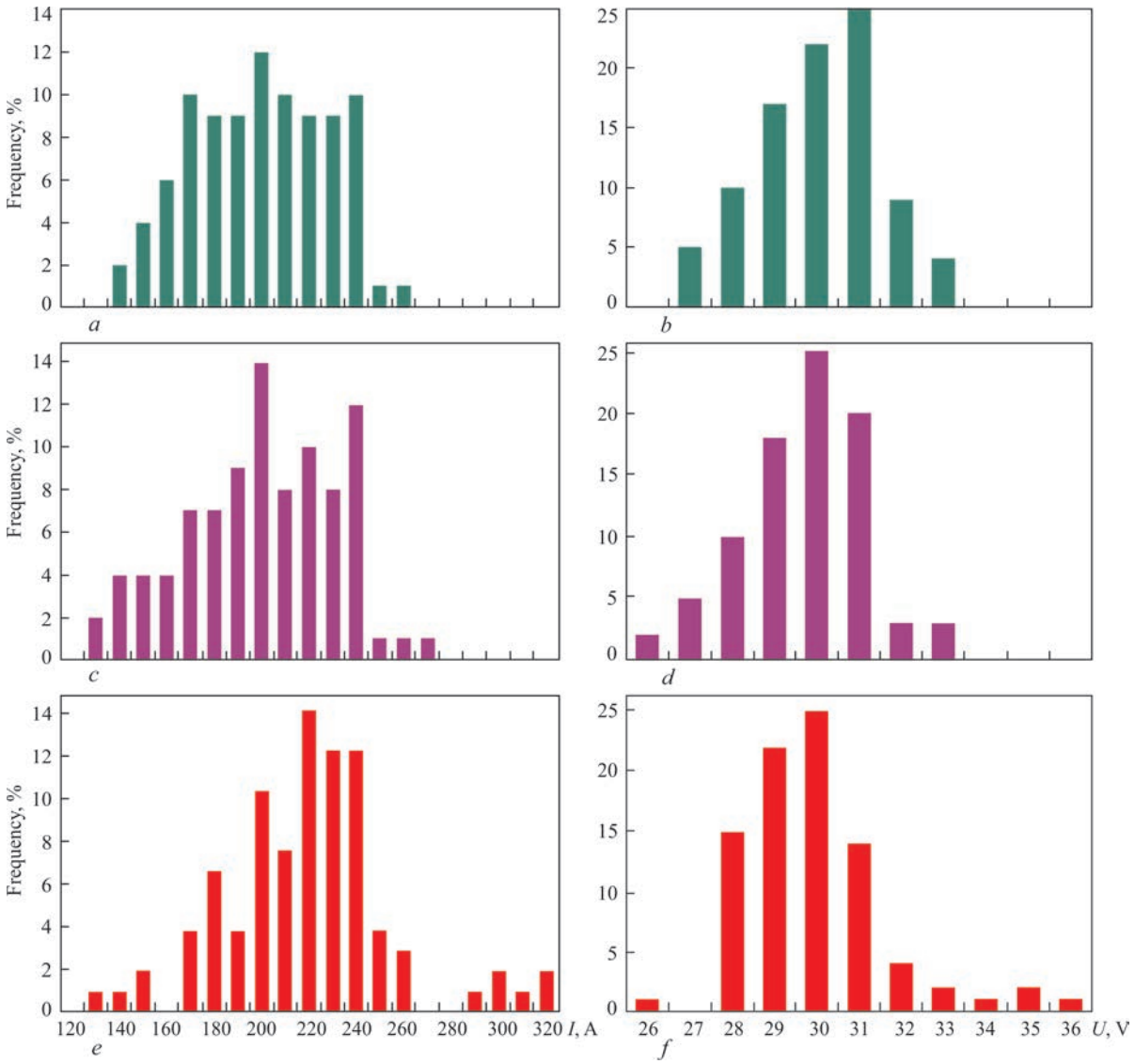

Figure 2. Histograms of distribution of current and voltage (*a, c, e*) and voltage (*b*, *d*, *f*) during surfacing with wires: No. 1 (*a*, *b*), No. 2 (*c*, *d*), No. 3 (*e*, *f*). Wire designations according to Table 2

Frequency, %

Performance of comprehensive analysis by the developed methodology, allowing for the melting and deposition rates, and the coefficient of losses, as well as the coefficients of variation by voltage and current and their distribution histograms, allowed determination of the increase in productivity and stability by 15–30 % during surfacing with experimental flux-cored wires (Nos 1, 2), compared to the wire-standard (No. 3).

CONCLUSIONS

1. A comprehensive methodology of comparative evaluation of the welding and technological properties of flux-cored wires for arc surfacing was developed, which is based on determination of the quality of deposited metal formation, parameters of process productivity and stability.

2. Application of the proposed methodology allows performing a comprehensive evaluation of the mentioned properties of flux-cored electrode wires, using quantitative characteristics, without application of complex and expensive software-hardware systems.

3. It was confirmed that the type and granulometric composition of metallic components of the core of flux-cored wires in electric arc surfacing influence the parameters and stability of the process, in particular, application of metallic granular powders of high chemical purity and homogeneity by physical properties, for instance of the type of R6M5, instead of the traditional ferroalloys, improves the welding and technological properties of flux-cored electrode wires.

REFERENCES

1. Ryabtsev, I., Fomichov, S., Kuznetsov, V. et al. (2023) *Surfacing and Additive Technologies in Welded Fabrication*. Switzerland, Springer Nature AG. DOI: https://doi.org/10.1007/978-3-031-34390-2
2. Pokhodnya, I.K., Shlepakov, V.N., Maksimov, S.Yu., Ryabtsev, I.A. (2010) Research and developments of the E.O. Paton

Electric Welding Institute in the field of electric arc welding and surfacing using flux-cored wire (Review). *The Paton Welding J.*, **12**, 26–33.
3. Pokhodnya, I.K., Suptel, A.M., Shlepakov, V.N. (1972) *Welding with flux-cored wire*. Kyiv, Naukova Dumka [in Russian].
4. Pokhodnya, I.K., Gorpenyuk, V.N., Milichenko, S.S. et al. (1990) *Metallurgy of arc welding: Processes in the arc and melting of electrodes*. Kyiv, Naukova Dumka [in Russian].
5. Golovko, V., Kotelchuk, O., Naumeiko, S., Golyakevich, A.A. (2022) Development of self-shielded flux-cored wires for arc welding of low-alloy steels. *Defect and Diffusion Forum*, **416**, 103–114. DOI: https://doi.org/10.4028/p-58v9g5
6. Shlepakov, V.N. (2014) Physical-metallurgical and welding-technological properties of gas-shielded flux-cored wires for welding of structural steels. *The Paton Welding J.*, **6–7**, 53–56. DOI: https://doi.org/10.15407/tpwj2014.06.10
7. Kostin, O.M., Yaros, O.O., Yaros, Y.O., Savenko, O.V. (2021) UPE-500 complex for determining welding and technological characteristics of coated electrodes. *The Paton Welding J.*, **8**, 33–37. DOI: https://doi.org/10.37434/tpwj2021.08.07
8. Pawlik, J., Bembenek, M., Goral, T. et al. (2023) On the influence of heat input on Ni–WC GMAW hardfaced coating properties. *Materials*, 16(**11**), 3960. DOI: https://doi.org/10.3390/ma16113960
9. Beczkowski, R., Gucwa, M. (2017) Cladding hardfacing layers used to protect the surface against abrasive wear. In: *Proc. 26th Inter. Conf. on Metallurgy and Materials*, *Brno, Czech Republic, May 24–26*, 1188–1193.
10. Kakhovs'kyi, M.Y. (2016) Influence of aqueous media on the gas saturation of weld metal in the course of underwater welding of 12KH18N10T steel. *Materials Sci.*, **51**, 843–846. DOI: https://doi.org/10.1007/s11003-016-9911-7
11. Zhang, M., Wang, Y., Zhang, W.-H. et al. (2018) Development of gas shielded flux cored wire for 1Cr12Ni2W1MoV stainless steel and properties of welded joint. *Transact. of Materials and Heat Treatment*, 39(**11**), 129–136. DOI: https://doi.org/10.13289/j.issn.1009-6264.2018-0215
12. Lankin, Yu.N. (2011) Indicators of stability of the GMAW process. *The Paton Welding J.*, **1**, 6–13.
13. Shlepakov, V.N., Kotelchuk, A.S., Gavrilyuk, Yu.A. (2017) Modern flux-cored wires for welding of low-alloy steels of increased and high strength. *The Paton Welding J.*, **11**, 8–12. DOI: https://doi.org/10.15407/tpwj2017.11.01
14. Majdanchuk, T.B., Skorina, N.V. (2014) Improvement of adaptability to fabrication and welding properties of electrodes for tin bronze welding and surfacing. *The Paton Welding J.*, **6–7**, 172–176. DOI: https://doi.org/10.15407/tpwj2014.06.37
15. Zhudra, A.P., Krivchikov, S.Yu., Dzykovich, V.I. (2014) Application of complex-alloyed powders produced by thermocentrifugal sputtering in flux-cored wires. *The Paton Welding J.*, **12**, 36–40. DOI: https://doi.org/10.15407/tpwj2014.12.08
16. Voronchuk, A.P., Zhudra, A.P., Petrov, A.V., Kochura, V.O. (2019) Influence of modes of flux-cored strip surfacing on their welding-technological properties. *The Paton Welding J.*, **1**, 33–37. DOI: https://doi.org/10.15407/tpwj2019.01.07
17. Ryabtsev, I.O., Babinets, A.A., Lentyugov, I.P. (2023) Welding-technological properties of flux-cored wire with boron-containing binder in the charge. *The Paton Welding J.*, **9**, 17–20. DOI: https://doi.org/10.37434/tpwj2023.09.03
18. Ryabtsev, I.O., Babinets, A.A., Lentyugov, I.P. et al. (2024) Welding and technological properties of flux-cored wire with the charge in the form of granulated powder. *The Paton Welding J.*, **7**, 17–21. DOI: https://doi.org/10.37434/tpwj2024.07.03
19. Mackenzie, J.G., Allen, M. (1998) Mathematical power tools: Maple, Mathematica, Matlab and Excel. *Chemical Eng. Education*, 32(**2**), 156–160.

ORCID
A.A. Babinets: 0000-0003-4432-8879,
I.O. Ryabtsev: 0000-0001-7180-7782,
I.P. Lentyugov: 0000-0001-8474-6819

CONFLICT OF INTEREST
The Authors declare no conflict of interest

CORRESPONDING AUTHOR
A.A. Babinets
E.O. Paton Electric Welding Institute of the NASU
11 Kazymyr Malevych Str., 03150, Kyiv, Ukraine.
E-mail: a_babinets@ukr.net

SUGGESTED CITATION
A.A. Babinets, I.O. Ryabtsev, I.P. Lentyugov (2025) Methodology for evaluation of the welding and technological properties of flux-cored wires for arc surfacing. *The Paton Welding J.*, **5**, 44–50.
DOI: https://doi.org/10.37434/tpwj2025.05.05

JOURNAL HOME PAGE
https://patonpublishinghouse.com/eng/journals/tpwj

Received: 24.01.2025
Received in revised form: 26.02.2025
Accepted: 21.05.2025

DOI: https://doi.org/10.37434/tpwj2025.05.06

ELECTROMAGNETIC-ACOUSTIC TRANSDUCER WITH A COMBINED MAGNETIZATION

H.M. Suchkov, S.Yu. Pliesnetsov, M.Ye. Kalnitskyi, Yu.Yu. Koshkarov, I.M. Oleksenko

National Technical University "Kharkiv Polytechnic Institute"
2 Kyrpichova Str., 61002, Kharkiv, Ukraine

ABSTRACT

The use of methods and means for excitation ultrasonic pulses of transverse waves using electromagnetic-acoustic transducers is becoming increasingly widespread in industry. However, transducers based on permanent powerful magnets have disadvantages, which consist in their strong attraction to ferromagnetic products and in the adhesion of ferromagnetic particles, which leads to distortion of the results of non-destructive testing and a decrease in sensitivity. Over time, such magnets gradually lose their magnetic properties. The known transducers with a pulsed magnetization can only operate with low probing frequencies due to heating. It is proposed to use permanent magnets with a relatively low magnetic field induction and additional pulsed magnetization simultaneously. Such a technical solution increases the sensitivity of the inspection and significantly reduces the attraction of the transducer to a ferromagnetic product, and also makes it possible to significantly increase the frequency of probing the test object.

KEYWORDS: ferromagnetic product, non-destructive testing, ultrasonic pulses, electromagnetic-acoustic transducer, magnetic field, pulsed magnetization

INTRODUCTION

Ultrasonic wave pulses are often used for non-destructive testing of metal products, most often ferromagnetic ones [1]. In conventional testing using a contact fluid, it is necessary to remove rust, paint, dirt, etc. from the surface of objects [1–3], which leads to significant material losses. The problem can be solved by using the electromagnetic-acoustic (EMA) method of excitation and reception of ultrasonic pulses [2, 4–6], which does not require special cleaning of the surface of metal products such as pipes, sheets, billets, etc.

It is known that the sensitivity of the EMA method of excitation and reception of ultrasonic pulses is quadratically dependent on the magnitude of magnetic field induction [4–5]. That is why many experts develop EMA transducers (EMAT) with high-power magnetic field sources [7]. However, a contradiction arises. On the one hand, the sensitivity of the EMAT increases, and on the other hand, the force of attraction of the EMAT to the test object (TO) made of ferromagnetic material grows significantly. In addition, exfoliated ferromagnetic particles, such as scale, adhere to the EMAT, which leads to the formation of powerful interference [8]. To eliminate the mentioned disadvantages, many researchers propose the use of pulsed magnetic field sources [9–16], which have the ability to obtain a powerful magnetic field at pulsed magnet supply currents of 2–3 kA. However, the coils of the pulsed source heat up quickly [9], which makes it impossible to perform flaw detection and thickness measurement of the TO with the required frequency of probing a metal product.

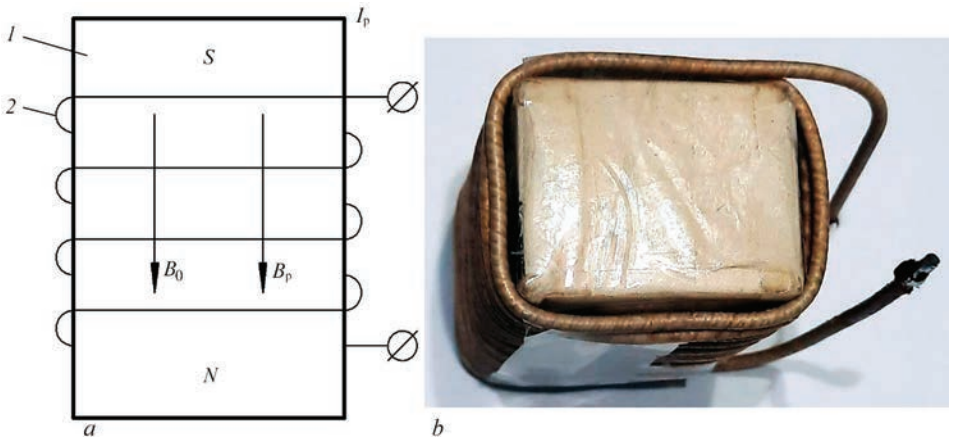

Figure 1. Simplified image of a magnetic field source with an induction vector oriented normal to the surface of a ferromagnetic metal product: design of the MFC (*a*) and its image (*b*); *1* — permanent magnet; *2* — pulsed magnetization coil; B_0 — magnetic field induction magnitude generated in the pulsed magnetization coil; B_p — pulsed magnetic field induction magnitude

This paper presents the results of improving EMAT by using a permanent magnet of low power and a pulsed magnetization at powering the coils of a magnetic field source with a current of less than 2 kA. Such an approach can significantly reduce the above disadvantages of the known EMAT.

AIM OF RESEARCH

is the comparative analysis of EMAT sensitivity with a combined magnetization.

EMAT WITH A COMBINED MAGNETIZATION AND ITS RESEARCH PROCEDURE

Let us consider, as an example, a combined EMAT for excitation and reception of ultrasonic shear wave pulses in a ferromagnetic metal product normal to its surface. The base of the proposed EMAT is a magnetic field source (MFS), which can be represented in the way as shown in Figure 1. In the simplest version, it is a permanent magnet and a pulsed magnetization coil.

Obviously, the MFC elements should meet a number of requirements: the permanent magnet material should be resistant to heat and have low electrical conductivity; the dimensions of the permanent magnet should provide a preferential orientation of the magnetic field induction vector normal to the TO surface (the cross-section of the magnet pole should be in the range of 30×30–50×50 mm^2, height 50–60 mm [9]) and a specified working area of the magnet action, which overlaps the working area of the high-frequency inductance coil [4]; the pulse magnetization coil should have a minimum inductance, which is necessary to form a short magnetization pulse.

A simplified mock-up of a combined EMAT based on a magnetic field source with a combined magnetization can be made as follows (Figure 2). The arrows in the volume of a ferromagnetic conductive metal product show the directions of propagation of ultrasonic pulses.

To perform the research, a mock-up (simplified unit) was made, the diagram of which is shown in Figure 3. The magnetic field source consists of a permanent magnet *1* based on NeFeB metal-ceramic, on which a magnetization coil 2 is wound (see Figure 1). The coil is powered from the unit *3* by magnetization current pulses. The high-frequency inductance coil *4* is powered by high-frequency current pulses from the unit *5*. The ultrasonic pulses *7* excited in the product

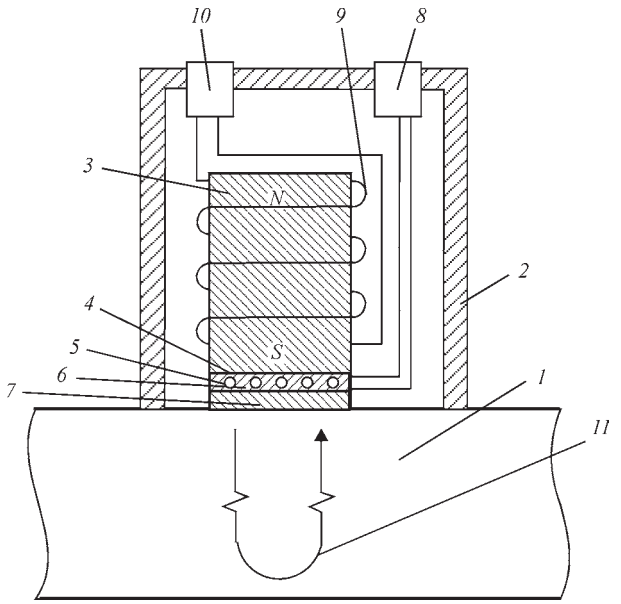

Figure 2. Simplified design of EMAT with a permanent and pulsed magnetization: *1* — ferromagnetic conductive metal product; *2* — casing; *3* — permanent magnet; *4* — pole of a permanent magnet *3*; *5* — plane high-frequency inductance coil; *6* — dielectric base; *7* — protector; *8* — electrical connector for powering high-frequency inductance coil *5*; *9* — pulsed magnetization coil; *10* — electrical connector for powering pulsed magnetization coil *9*; *11* — ultrasonic wave pulses in the TO

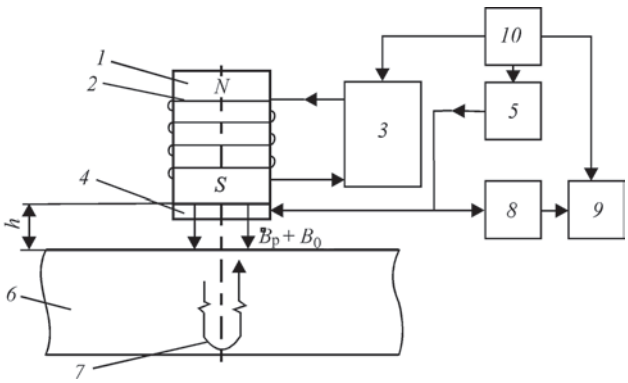

Figure 3. Test bench for studying capabilities of EMAT with a combined magnetization

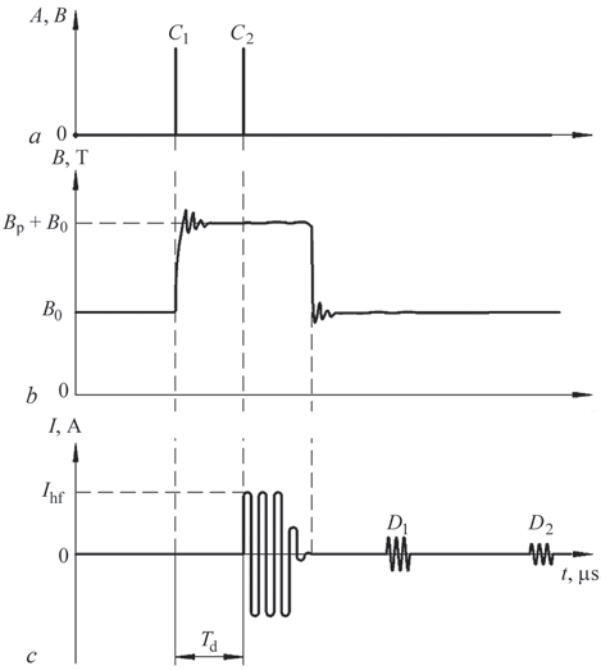

Figure 4. Functional diagram of operation of the test bench with a combined magnetization of the TO by one cycle of ultrasonic pulse probing

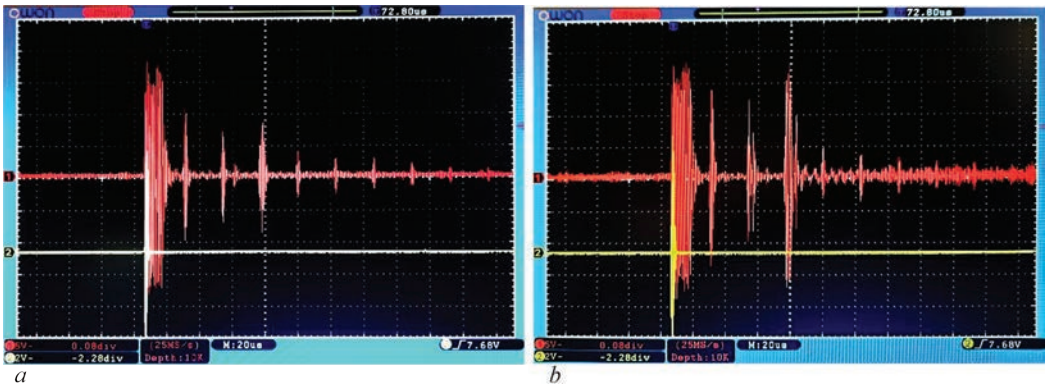

Figure 5. Realizations with sequences of bottom pulses reflected in the TO received in the absence of a pulsed magnetization (*a*) and with the combined operation of a permanent and pulsed magnetization (*b*)

6 are reflected from the metal volume and received by the high-frequency coil *4*. The ultrasonic pulses *7* received from the product *6* are amplified by the unit *8*, from which they are transmitted to the unit *9*, where they are processed and visualized. The control and synchronization of the bench elements is performed by the unit *10*. $B_p + B_0$ is the direction of the induction vector of the resulting magnetic field.

During research, the dimensions of the permanent magnet were 30×40×60 mm. The magnet material was made on the base of NeFeB. The pulse magnet coil had 21 turns of the wire with a diameter of 2.4 mm. The distance from the pole of the magnetic field source to the TO surface made of 39 mm thick st45 steel was 10.6 mm. The peak current in the magnetization coil reached 270 A. The delay of the high-frequency packet pulse relative to the start of the magnetization pulse exceeded 50 μs. The duration of the high-frequency packet pulse was equal to three periods of the 2.3 MHz filling frequency.

Figure 4 shows a functional diagram of operation of the combined magnetization test bench.

The test bench operates as follows. The EMAT is placed above the surface of the TO *6*, so that the distance from the pole of the permanent magnet *1* to the metal product *6* amounts to *h* (usually several millimetres). A permanent magnetic field B_0 is formed in the surface layer of the TO. The control and synchronization unit *10* transmits a synchronizing pulse C_1 to the unit *3* (Figure 4, *a*). The unit *3* excites a current pulse in the magnetization coil *2* with a time duration of several tens of microseconds, which excites the induction B_p in the surface layer of the TO. The magnetic fields generated by the magnetization coil *2* and magnet *1* coincide in direction and consist of $B_p + B_0$ (Figure 4, *b*). Next, the control and synchronization unit *10* transmits a synchronizing pulse C_2 (Figure 4, *a*) to the unit *5* with a delay T_d, which excites a packet pulse of high-frequency current in the high-frequency inductance coil *4*. As a result, a high-frequency eddy current I_{hf} is excited in the surface layer of the TO *6* in the zone of action of $B_p + B_0$ (Figure 4, c). The interaction of the magnetic field $B_p + B_0$ and the eddy current I_{hf} in the surface layer of the TO *6* due to the electromagnetic-acoustic conversion leads to the excitation of ultrasonic packet pulses in a metal product (Figure 3, position *7*). The ultrasonic pulses reflected from the TO *6*, e.g. bottom signals D_1 and D_2, are received by the high-frequency inductance coil *4* by means of an inverse electromagneto-acoustic conversion. The electric pulses received and converted by the coil *4*, which carry information about the quality of the metal product *6*, are amplified by a low-noise unit *8* (Figure 3), from which they are transmitted to the unit *9*, where they are processed and visualized.

As a result, due to the additional magnetic field B_p, the power of the excited ultrasonic pulse increases significantly and, accordingly, the sensitivity of ultrasonic testing grows, since the ratio of the amplitude of the useful signal to the amplitude of the noise increases. This conclusion is confirmed by the results of experimental studies (Figure 5) performed with the use of the bench (Figure 3).

From the analysis of the data obtained during the experimental studies, it was found that an increase in the amplitude of the bottom pulses due to the use of a pulsed magnetization reached 40 %. This means that the sensitivity of testing ferromagnetic metal products grows. In addition, the force of attraction of the magnet to the TO decreased, which improved the process of scanning the surface of the ferromagnetic TO by the operator using a portable EMAT.

CONCLUSIONS

It was found that in order to increase the sensitivity of testing, it is advisable to apply a magnetic field source with a simultaneous use of a permanent and a pulsed magnetic field.

To ensure an increase in the amplitude of the useful signal in relation to noise, it is necessary to delay the action of a high-frequency pulse in relation to the beginning of a magnetization pulse by at least 50 μs.

The use of additional pulsed magnetization makes it possible to increase the amplitude of the bottom pulses in relation to interference by up to 40 % at gaps between the TO and MFC surfaces of more than 10 mm.

Applying this technical solution, the force of attraction of the EMAT against the ferromagnetic TO is reduced, which improved the process of scanning the surface of the ferromagnetic TO by the operator using a portable EMAT.

REFERENCES

1. Karpash, M.O., Rybitskyi, I.V., Koturbash, T.T. et al. (2012) *Acoustic control of structures and equipment in oil and gas industry*: Monography. Ivano-Frankivsk, Vyd-vo IFNTUHG [in Ukrainian].
2. https://www.autondt.com
3. Pozniakova, M.Ye. (2021) *Ultrasonic method and tool for detecting internal defects in railway axles:* Syn. of Thesis for Cand. of Tech. Sci. Degree. Kharkiv [in Ukrainian].
4. Desiatnichenko, O.V. (2015) *Electromagnetic-acoustic thickness gauge for checking metal products with dielectric coatings*: Syn. of Thesis for Cand. of Tech. Sci. Degree. Kharkiv [in Ukrainian].
5. Pliesnetsov, S.Yu. (2021) *Development of methods and tools for electromagnetic-acoustic testing of rod, tubular and sheet metal products:* Syn. of Thesis for Dr. of Tech. Sci. Degree. Kharkiv [in Ukrainian].
6. *Innerspec Website*: https://www.innerspec.com/portable/emat-sensors
7. Suvorova, M.D. (2019) Development of magnetization sources for EMO converters on the basis of powerful permanent magnets. *Visnyk NTU KhPI. Seriia: Elektroenerhetyka ta Peretvoriuvalna Tekhnika*, **1**, 63–73 [in Ukrainian].
8. Suchkov, H.M. (2005) *Development of the theory and practice of creating devices for electromagnetic-acoustic control of metal products:* Syn. of Thesis for Dr. of Tech. Sci. Degree. KhPI, Kharkiv [in Ukrainian].
9. Donchenko, A.V., Myhushchenko, R.P. Suchkov, H.M., Kropachek O.Yu. (2024) *Surface-mounted combined electromagnetic-acoustic transducer with pulsed magnetization for inspection of ferromagnetic metal products*. Utility model Pat. 156088, U202304534, Publ. 08.05.2024 [in Ukrainian].
10. Heng Zhang, Shu-juan Wang, Guo-fu Zhai, Ri-liang Su (2014) Design of bulk wave EMAT using a pulsed electromagnet. In: *IEEE Far East Forum on Nondestructive Evaluation/Testing (FENDT), Chengdu, China, 20–23 June 2014*. DOI: https://doi.org/10.1109/FENDT.2014.6928272
11. Hernandez-Valle, F., Dixon, S. (2011) Pulsed electromagnet EMAT for ultrasonic measurements at elevated temperatures. *Insight — Non-Destructive Testing and Condition Monitoring*, 53(**2**), 96–99. DOI: https://doi.org/10.1784/insi.2011.53.2.96
12. Ogata, S., Uchimoto, T., Takagi, T., Dobmann, G. (2018) Development and performance evaluation of a high-temperature electromagnetic acoustic transducer for monitoring metal processing. *Int. J. Appl. Electrom*., 58(**3**), 309–318. DOI: https://doi.org/10.3233/JAE-180016
13. Hernandez-valle, F., Dixon, S. (2010) Initial tests for designing a high temperature EMAT with pulsed electromagnet. *NDT & E Inter*., 4(**2**), 171–175. DOI: https://doi.org/10.1016/j.ndteint.2009.10.009
14. Guofu Zhai, Bao Liang, Xi Li, Yuhang Ge, Shujuan Wang (2022) High-temperature EMAT with double coil configuration generates shear and longitudinal wave modes in paramagnetic steel. *NDT & E Inter*., **125**, 1–12. DOI: https://doi.org/10.1016/j.ndteint.2021.102572
15. Salam Bussi, Suchkov, G., Mygushchenko, R. et al. (2019) Electromagnetic-acoustic transducers for ultrasonic measurements, testing and diagnostics of ferromagnetic metal products. *Ukrainskyi Metrolohichnyi Zh.*, **4**, 41–49. DOI: https://doi.org/10.24027/ 2306-7039.4.2019.195956
16. Suzhen Liu, Ke Chai, Chuang Zhang, Liang Jin, Qingxin Yang (2020) Electromagnetic acoustic detection of steel plate defects based on high-energy pulse excitation. *Appl. Sci*., 10(**16**), 5534. DOI: https://doi.org/10.3390/app10165534

ORCID

H.M. Suchkov: 0000-0002-1805-0466,
S.Yu. Pliesnetsov: 0000-0001-8428-5426,
Yu.Yu. Koshkarov: 0000-0003-1430-0154,
I.M. Oleksenko: 0009-0007-9302-1300

CONFLICT OF INTEREST

The Authors declare no conflict of interest

CORRESPONDING AUTHOR

H.M. Suchkov
National Technical University
"Kharkiv Polytechnic Institute"
2 Kyrpichova Str., 61002, Kharkiv, Ukraine.
E-mail: hpi.suchkov@gmail.com

SUGGESTED CITATION

H.M. Suchkov, S.Yu. Pliesnetsov, M.Ye. Kalnitskyi, Yu.Yu. Koshkarov, I.M. Oleksenko (2025) Electromagnetic-acoustic transducer with a combined magnetization. *The Paton Welding J*., **5**, 51–54.
DOI: https://doi.org/10.37434/tpwj2025.05.06

JOURNAL HOME PAGE

https://patonpublishinghouse.com/eng/journals/tpwj

Received: 29.01.2025
Received in revised form: 20.03.2025
Accepted: 11.06.2025